Evaluation of Organ-on-Chip Microfluidic Flows Using Optical Coherence Tomography

Eric Safai

Masters of Science Thesis

Biomedical Engineering, 3mE

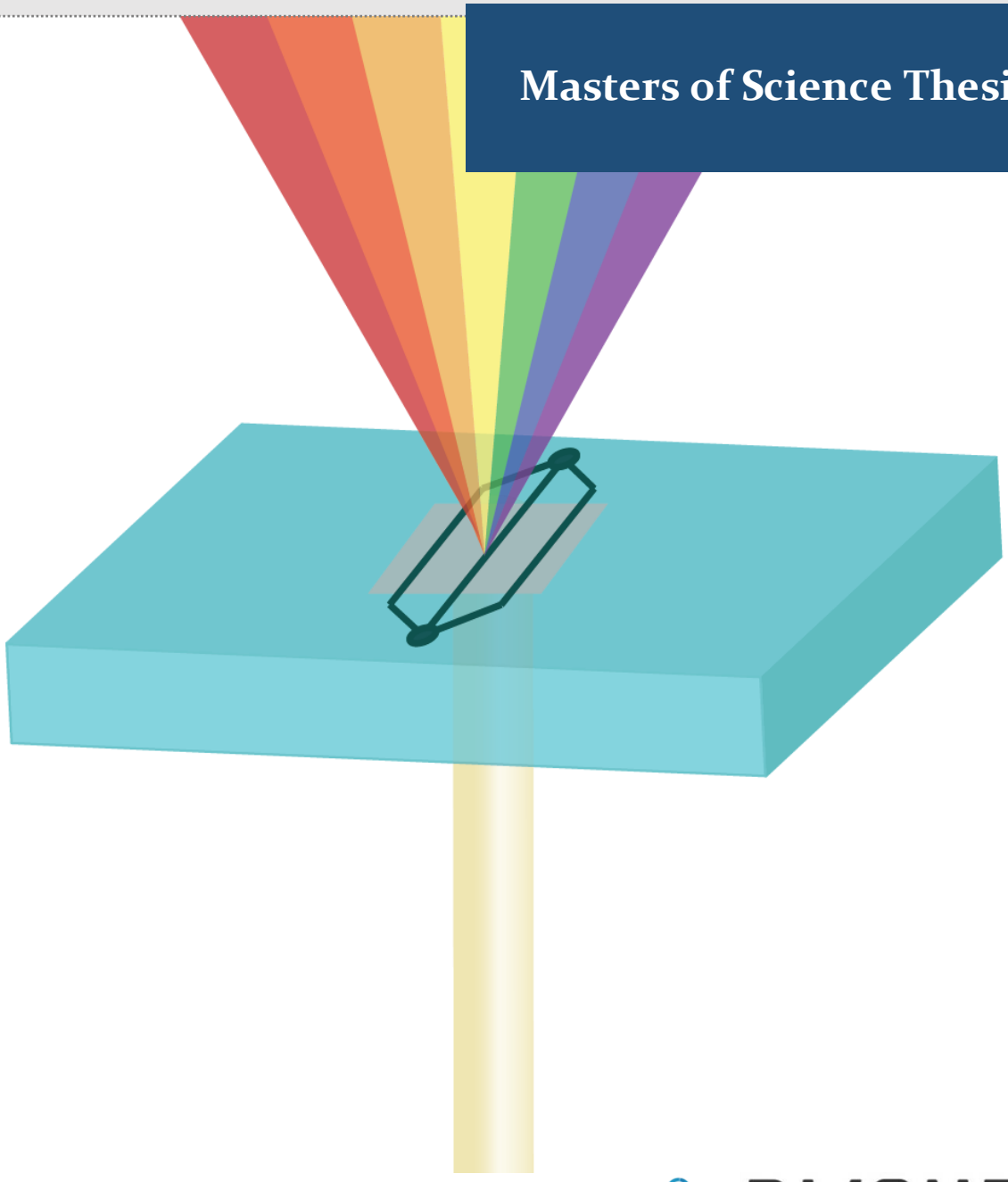

TU Delft
Delft University of Technology

BI/OND
The Versatile Organ-on-Chip platform

Evaluation of Organ-on-Chip Microfluidic Flows Using Optical Coherence Tomography

Master of Science Thesis

For the degree of Master of Science in Biomedical Engineering at
Delft University of Technology

Eric R. Safai

June 19, 2020

Faculty of Mechanical, Maritime and Materials Engineering (3mE) · Delft
University of Technology


TU Delft
Delft University of Technology


BI/OND
The Versatile Organ-on-Chip platform


ImPhys

Delft University of Technology
Department of Biomedical Engineering

The undersigned hereby certify that they have read and recommend to the Faculty of
Mechanical, Maritime and Materials Engineering (3mE) the acceptance the thesis Entitled

Evaluation of Organ-on-Chip Microfluidic Flows Using Optical Coherence Tomography

By

Eric R. Safai

In partial fulfillment of the requirements for the degree of
Master of Science Biomedical Engineering

Dated: June 19, 2020

Supervisors:

Prof. Dr. Ronald Dekker

Dr. ir. Nikolas Gaio

Readers:

Prof. Dr. Paddy French

Ir. Jos de Wit

Acknowledgements

I would first like to express a deep gratitude to Niko. His poignant insight and productive comments were only outweighed by his patience and understanding, particularly given personal and global circumstances. It has been a pleasure to work with him and a huge learning experience. I would further like to thank Prof. Ronald Dekker and the BI/OND team for their support and ability to make the research and work process enjoyable with an encouraging atmosphere. I recognize that I am quite fortunate to have had them as mentors and colleagues during my studies. As a result, I have not only learned an incredible amount about performing proper research, but moreover I have gone through life experiences whose lessons that from now on I hope to carry with me.

I am also thankful for the involvement of Jos De Wit with taking OCT measurements, his assistance with looking at the data, and fruitful discussions in this project. I wish him the best of luck with the continuation of his PhD. I know he will persevere in these unique circumstances. I want to specifically extend my appreciation to Cfan for her friendship over the past decade, for her dry, witty humor, and for always be there when I was in need of unrestrained and unbiased advice. Her comments on the thesis work were also helpful; her biggest contribution was in assisting to bring my poorly sketched cover image to life.

Next, I would like to thank the many loved ones and friends, both in Delft and around the world, from my time in Europe to from the earliest days of my childhood, those with whom I converse regularly and those with whom I can always call out of the blue and pick up from where we last left off. Sahil, Matthew, Mikey, Nandi, Josh, Paul, Michelle, Sedris, my Jebers, Burak & Frederiek, Harry – I am fortunate enough that the list could be expanded much more. Thank you all for you unwavering support from great and near distances.

I would like to also acknowledge support from the Foundation Justus & Louise van Effen and the Groesbeek Assenbroek Funds. Along with this, I would like to extend my gratefulness to Peggy Eskikiliç-Jong and Stephanie Meulemans. Both of them were there for me in difficult times and continued to support me long after their resolutions were fulfilled. Continue the great work in supporting deserving and hardworking students.

Finally, I would like to give my deep appreciation and love to my family. I am blessed to have had my sister join me on this adventure to study in Europe, and I expect to experience many more adventures with her throughout life. I could not have made it without you. And to my parents, who have dealt with the distance of both their children admirably. Thank you for helping in my pursuits and supporting me every day.

Delft, University of Technology — Eric Safai
June 19, 2020

Table of Contents

List of Figures

Chapter 1

Chapter 2

Chapter 3

Chapter 4

Appendix A

Appendix B

Appendix C

Appendix D

List of Tables

Appendix D

Abstract

Isolation of specific biological phenomena *in vitro* is critical to understanding living systems, due to cells' innate capacity to integrate and respond to a wide range of signals simultaneously. Concomitantly, advances in micromanufacturing techniques overlap with progress in tissue engineering to produce microenvironments that better mimic *in vivo* systems. The convergence of these fields has given rise to microfluidic 3D culture platforms which have resulted in a large shift in the understanding of how many biological processes unfold due the platform's ability to highly control microarchitectures, biochemical gradients, co-culture conditions, and mechanical stimuli. So-called Organ on Chip's (OOCs) have been instrumental in shifting the paradigm in which cell culturing is carried out and in which ways scientists think about testing potential drug therapeutics.

The microfluidic OOC platform, inCHIPit™, by BIOND Solutions, B.V. is a versatile tool designed for co-culture with a variety of macroscopic tissue types, such as organoids, explants, spheroids, and microtissues. It is a silicone (a.k.a. PDMS) and silicon-based platform that has the capacity for pneumatically controlled flexions and monitoring bioelectrical potentials. The inCHIPit™ model has already be implemented to model various organs, including midbrain organoids and induced pluripotent stem cells (iPSCs). The purpose of this study, however, is to further characterize the laboratory tool itself rather than the potential biological applications. Here, optical coherence tomography (OCT) is used to interrogate the OOC device's construction and culture capability by making use of properties of interfering waves and backscattering light. Furthermore, the microfluidic fluid flows and diffusion events in an OOC were characterized with OCT for the first time. And, as proof of concept, organoid-like bodies (OLBs) and their impact on flows in culture were examined.

inCHIPit™ consists of two microcompartments – a straight microfluidic channel and a culture well separated by a microporous PDMS membrane – which are supported by a series of interlocking plates and a culture lid, all composed of different materials. In terms of imaging quality, the plate material choice and lid optical traits played a key role by limiting background noise, yet, for instance, the culture lid qualities would prove inhibiting to OCT measurements during actual cell culture experiments. Moreover, the fluid velocity profiles within in inCHIPit™ microfluidics were observed and were demonstrated to exhibit characteristic velocity profiles. It was also shown that mass transport phenomenon across the porous membrane in the cell culture well occur and follow typical diffusive mechanisms. Further, initial observations as to the effects of OLBs on fluid flow characteristics in the inCHIPit™ platform were reported. The compilation of OCT and OLB measurements and observations make a strong argument for the potential of inCHIPit™ system as a staple of biomedical applications.

Chapter 1

Introduction

Lab on chip (LOC) devices have witnessed an aggressive increase in prevalence and application across a large number of academic fields. Advances in microfabrication techniques starting in the early 1990's helped realize the benefits of smaller build dimensions – shorter heat and mass transport times, reduced reaction volumes, high capacity for parallel experiments – which led to the explosion of microelectromechanical systems (MEMS) and micro total chemical analysis systems (μTAS) in recent decades [1]. Applications include point-of-care diagnostics, forensics sciences, biomolecular analyses, chemical separation, and microparticle synthesis [2]–[4]. A notable result of such efforts is the endeavor to sequence the human genome; over the course of the last three decades, the cost per human genome has plummeted from $100 million USD to ca. $1000 USD while the time required to sequence a single human genome has also been dramatically reduced [5]. A large driver of this cost reduction is the foundation of next-generation sequencing technologies in microfluidic methods with highly paralleled reactions [6], [7]. There are, as well, commercial examples of LOC applications, like Agilent's 2100 bioanalyzer which amalgamates microfluidics and ultraviolet (UV) spectrometry for better quantitation of nucleic acids [8].

Continued advances in microfabrication techniques have similarly led to biomedical MEMS (bioMEMS), which attempt to better recapitulate biological environments [9]. And, as with the goals of MEMS and μTAS, the ultimate achievement of bioMEMS is to overcome the larger issue of reducing the variability, costs, and time to implementation associated with drug development and clinical testing [10]; an overview of the current process is shown in Figure 1.1. Microfluidic channels can be precision-engineered to have complex structures and connections, while prototyping systems have been expedited through soft-lithographic techniques employing an optically transparent polymer polydimethylsiloxane (PDMS) [11], [12]. Along with developments in micropumping [13] and membrane synthesis methods [14], some LOC platforms may be implemented in simulating complex biological systems. Development of these systems and ones that are similar has earned these culture systems classification as Organ on Chip's (OOCs) for their growing abilities to emulate human organ functions and responses to stimuli.

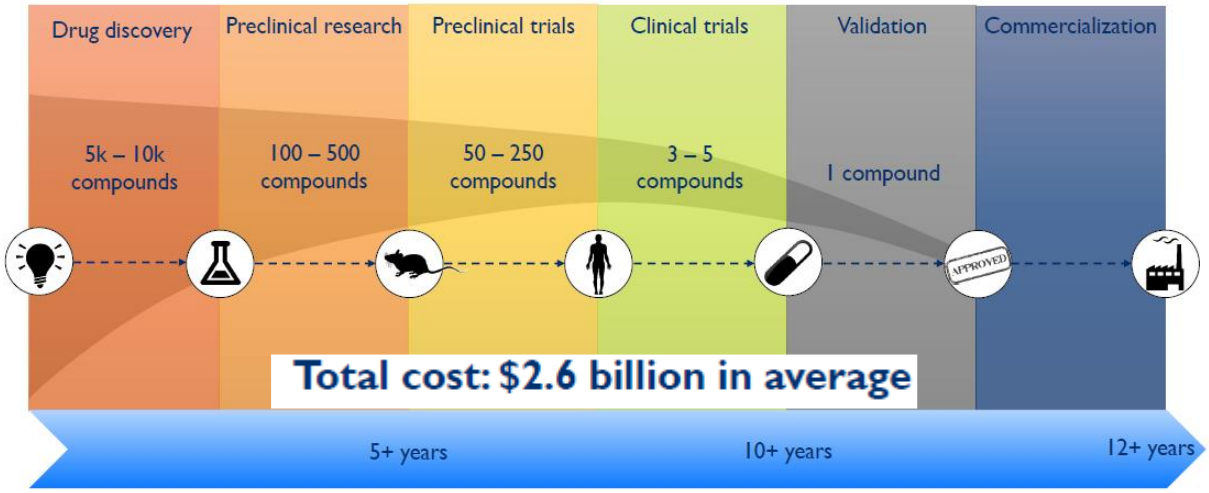

Figure 1.1 Example development process for discovery of new therapeutics [5].

However, despite rapid progression of these *in vitro* models, there are still limitations in comparison to *in vivo* situations that must be overcome. Cells integrate and process a myriad of external and internal stimuli simultaneously, which makes isolating the impact of specific effects a significant challenge, whether the effect is biochemical, genetic, or mechanical. Another complication arises when attempting to co-culture multiple cell types due to highly complex interactions between the two or more sets of cell types. Consequently, current and emerging OOC devices attempt to enable quantification of more system traits while remaining faithful to biological recapitulation. In this introductory chapter, an overview of the recent growth and development of advanced three-dimensional (3D) cell culture methods will be discussed as well as a brief explanation of the microfabrication methods for production of the specific culture system implemented in this master's thesis work. Subsequently, the structure and aims of the thesis are highlight at the conclusion of this chapter.

1.1 Organ on Chips – 3D Microfluidic Cell Culture

Prior to the advent of OOC development and research, a variety of *in vitro* methods have been developed over the last decades to generate human tissue models outside of the body. Initial methods implemented simpler two-dimensional (2D) models, such as cell culture in flat conformations on Petri dishes, porous membranes, and later, trans-species assays through the use of laboratory animals [15]. These modelling methods, however, lacked efficient means to measure physiological stimuli in similarly complex environments as those found in the human body. Furthermore, cells in such cultures lacked the correct spatial orientations. Experiments performed by Bischel *et al.* (2014) demonstrated variable responses of endothelial cell secretions dependent on the spatial culture conditions, with cells in a lumen configuration showing larger and more homeostatic concentrations of exocytosed factors [16]. The authors further showed *in vitro* higher invasive behavior of kidney cancer epithelial cells when cultured with HUVECs in a luminal shape, suggesting local microenvironment structure has a contributing role to tumor progression [16]. The arrangement of cells in OOC cultures may be controlled by fluid flow effects, patterning in extracellular matrix (ECM) or synthetic hydrogels, and microfluidic chip chamber design [17].

Organ on chip platforms are advanced microfluidic cell culture systems developed with the intention of better mimicking *in vivo* conditions of the human body *in vitro* [18]. These platforms may also be referred to as 3D microfluidic culture platforms. This technology developed due to the integration of multiple engineering and biological disciplines, including microfabrication methods and tissue engineering, along with the increasing demand for more accurate *in vitro* testing in drug research and development [19]. Superior recapitulations of *in vivo* responses are achieved due to a wide range of improvements over previous traditional cell culture methods, including 3D microenvironments for cell growth, induction of mechanical forces from fluid flows or applied compression and tension,

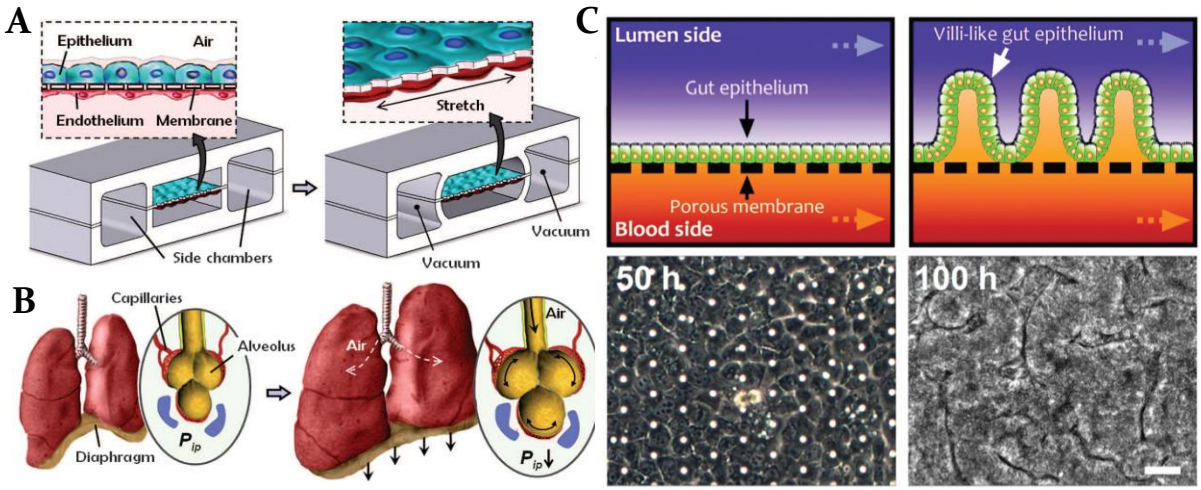

Figure 1.2 Examples of specific organ systems reconstituted in a foundational OOC platform engineered at the Wyss Institute. **A**. Microfabricated lung OOC, though compartmentalized PDMS microchannels, recreates the alveolar-capillary interface, along with mechanical motion, as diagramed in **B**. **C**. In a similar model, formation of villi-like structures was demonstrated after extended culture under cyclic stress. Scale bar is 25 μm. Figure adapted from Ref. [22], [23].

production of stable, quantifiable biochemical gradients, and complex co-culturing methods [20]. Through this nexus of factors, the creation of minimal, artificial operating units that imitate tissue- and organ-level responses has been achieved.

Organ on chip systems have also been crucial in elucidating the previously overlooked role of mechanical forces in cell, tissue, and organ development, as described by Donald Ingber, founder of the Wyss Institute and arguably the entire OOC field [21]. For example, the first "lung-on-chip" was created in 2010 at the Wyss Institute, which utilizes a porous, flexible membrane to separate co-cultured endothelial cells and lung cells while simultaneously applying pneumatically driven cyclical strains along the membrane interface (Figure 1.2) [22]. Air flow is also applied to maintain an air-liquid interface at the membrane boundary, similar to the interface established in alveolus of the lungs where gas exchange during normal respiration. This same system was adapted to mimic the conditions in the gut where mechanical stimulations were demonstrated to induce cell differentiation and encourage the appearance of villus-like structures at the transition between the intestinal lumen and mucosal barrier [23].

Besides advantages of control over the spatial arrangement and physical perturbations of cells, OOC devices, due to the nature of near-Stokes flow (i.e. low Reynolds number flow) as a result of their O(10-100) micrometer length scales, allow for the generation of finely controlled physical and biochemical gradients [24]. For instance, angiogenesis, the dynamic remodeling of vascular beds *in vivo*, has been "orchestrated," as phrased by the authors, under soluble angiogenic factors, VEGF and ANG-1 [25]. The OOC platform itself is designed in such a way for easy examination of any number of induced biochemical gradients. Similar work was performed by the commercial organ on chip company Mimetas B.V., where scientists quantified angiogenic events in a high-throughput manner with biochemical gradients maintained for up to six days [26]. Concomitantly, the circa nanoliter volumes utilized in microfluidic systems significantly improves reagent reaction efficiency; the ease of access permits researchers to control the temporal induction of chemical gradients; and, dilution effects are easily studied due to the predictable nature of fluid mechanics and mixing effects [27], [28].

Similar to the regulation of chemical gradients, shear and pressure forces are straight-forward to control and engineer as a result of laminar flows in microfluidic channels [29]. Additionally, due to the facile selection and introduction of microenvironmental scaffolding (i.e. ECM) into microfluidic chips, cellular mechanoregulation and mechanotransduction phenomena have been more rigorously characterized [30]. Specifically, for instance, work from Noo Li Jeon's lab demonstrated angiogenic sprouting events were strongest when interstitial fluid flow – the convective transport of bodily fluids through extracellular tissue – went against the direction of elongation [31]. Mechanical cues can also be induced by manipulating the microfluidic system itself rather than through geometry or pressure-driven flows. Work performed at the Technical University of Delft (TU Delft), the so-called Cytostretch,

showed how pneumatically, cyclically applied pressures to cells cultured along a flexible, porous membrane can simulate physiological conditions in tissue that experience external forces, such as heart or gut [32]. Similarly, actuation fluid was oscillated underneath a cell culture chamber that was positioned strategically at an air-liquid interface to emulate conditions at the alveolar-capillary transition in alveolar sacs in human lungs [33].

While several features of biological development and behavior are highlighted herein, more cues are integrated and dynamically processed as a part of cellular homeostasis and spatiotemporal dynamics. Parameters such as co-culture conditions, organ-organ interactions, and metabolic factors are deterministic in how cells will behave. These characteristics are summarized and visualized in Figure 1.3 [34]. Moreover, OOC models applied to interrogate disease conditions and to aid in drug development are not covered; these are given provided in additional literature overviews [35]–[38].

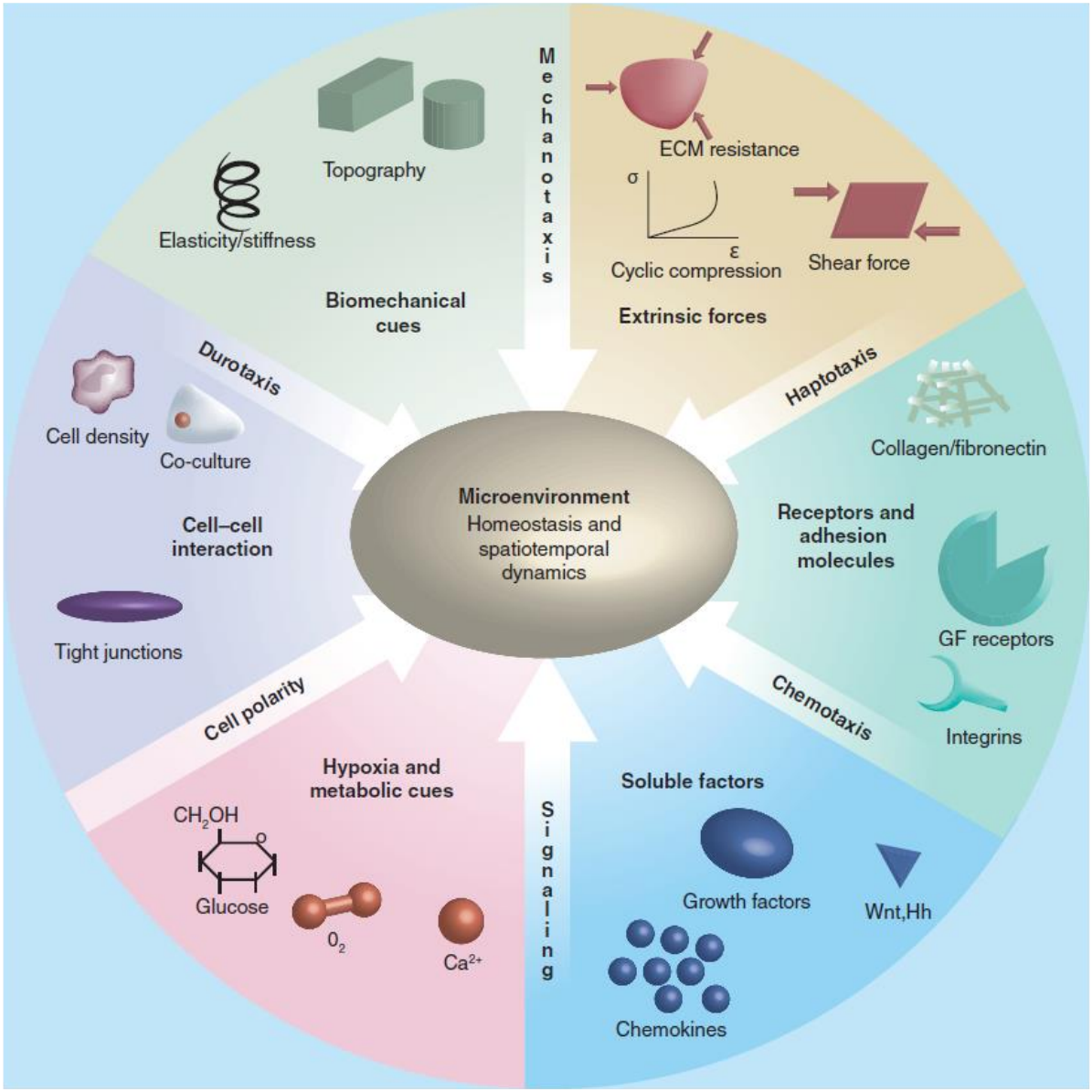

Figure 1.3 Critical parameters to consider when modelling organ systems in 3D *in vitro* microenvironments. In the body, cells react singularly to all dynamic cues at once; OOC platforms provide the opportunity to isolate specific impacts of factors. ECM: extracellular matrix; GF: growth factor; Hh: hedgehog. Adapted from Ref. [34].

1.2 BI/OND OOC Device

As mentioned earlier in this chapter, the OOC field has rapidly expanded in its number of publications [39], in its incubation of dozens of companies globally [40], and in the intricacy of microfluidic and organ system designs [41]. This is a result of OOCs' potential to address and drastically improve many challenges being faced by the pharmaceutical industries and healthcare systems, such as the high costs of research and development (R&D) and the advancement of personalized medicine [42].

BIOND Solutions B.V., is a start-up company founded by researchers at TU Delft the Electrical Engineering, Mathematics, and Computer Science (EEMCS) faculty with the goal of developing a versatile OOC platform intended to serve as a flexible culture system for scientists and medical researchers. The BI/OND platform, inCHIPit™, is designed as a multifunctional, integrated tool for microfluidic 3D (co-)culture of organ-specific cell(s) and larger macroscopic tissue samples, such as organoids, explants, spheroids, and microtissues [43]. Further, due to the fact that this device is fabricated using traditional clean room methods, the BI/OND platform allows for the *in situ* monitoring of electrochemical parameters such as electrical biopotentials with integrated carbon nanotube microelectrode arrays [44]. And, as a final key quality of inCHIPit™, the PDMS microporous membrane permits for mechanical stimulations of the culture environment [45]. The design goals and fabrication process are further expounded upon in the following subsections.

1.2.1 Design Goals

Traditionally, most of the hundreds of OOC devices are produced using soft lithographic methods in tandem with the optically transparent, flexible elastomer PDMS due to the process' affordability and rapid prototyping [46]. The BI/OND microfluidic chip was designed with some specific goals in mind; namely, production of such chips with microfabrication compatible methods, tissue culture versatility to accommodate human (co-)culture models and macroscopic tissues, integration of real-time sensors, and induction of mechanical forces relevant to specific organ types.

1.2.2 Fabrication & Assembly

In this section, the fabrication and assembly process for the BI/OND platform is explained in brief (Figure 1.4), as this process is not the main focus of this work. More in-depth descriptions and assessments of the PDMS on Silicon (POS) guidelines can be found in the work *Organ-on-Silicon* by Gaio *et al.* [43].

The first step in fabrication of the BI/OND device is deposition of silicon oxide (SiO_2) onto both sides of a 500 µm silicon (Si) wafer. Using plasma enhanced chemical vapor deposition (PECVD), a 1 µm deep SiO_2 layer is deposited on the frontside and a 5 µm layer on the backside. The thickness of backside SiO_2 layer is such because it is serving as a hardmask for patterning steps later in the fabrication process. A PDMS layer is coated on the frontside of the Si wafer via spin coating, which allows for the direct tuning of PDMS membrane thickness, ranging from 2 to 20 µm [14]. An aluminum (Al) hardmask is patterned to the spin coated PDMS to create an etching design for the generation of the porous membrane and inlet/outlet openings for the microfluidic portion of the BI/OND device. In order to preserve a volume for the microfluidic channel, a sacrificial layer is deposited above the membrane pores and the intended path(s) for the microchannel. Additional PDMS is then dispensed to surround the sacrificial material to create the walls and bottom of the microchannel; the thickness of the PDMS is approximately 200 µm. The last major step is to form the culture well that is atop the porous membrane and microchannel. The backside is etched using deep reactive ion etching (DRIE) and buffered hydrofluoric acid (BHF) etching, which specifically removes the Si substrate and SiO_2 layers adjacent to the PDMS, respectively. These final steps establish the culture well and the microfluidic inlet and outlet. The final product is shown in Figure 1.5.

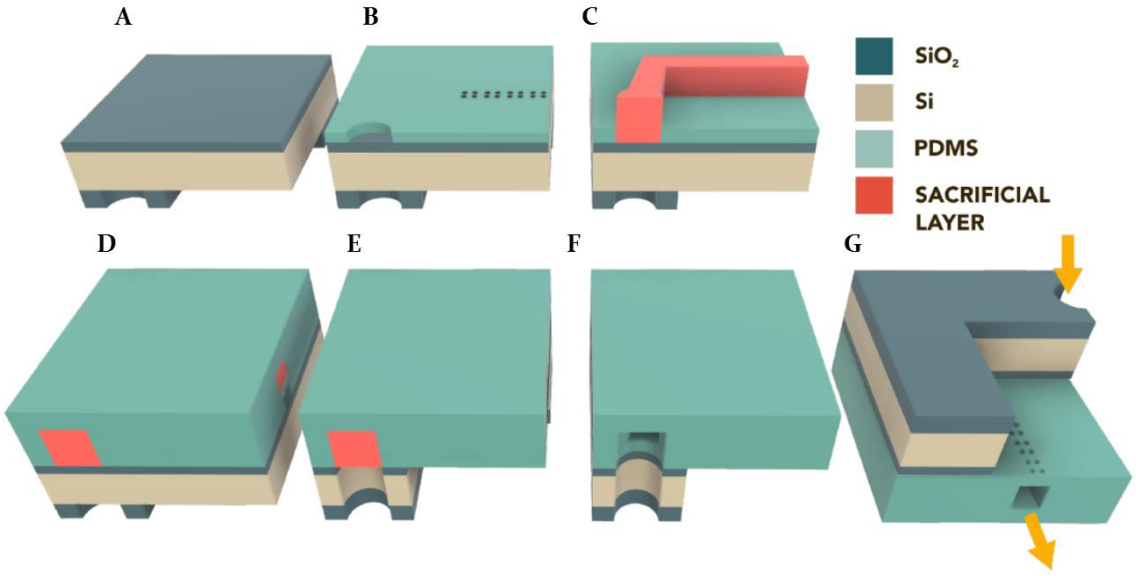

Figure 1.4 Schematic of BI/OND fabrication and assembly process. **A**. Using PECVD, SiO2 is deposited to the front and back of the silicon wafer, 2 and 6 µm, respectively. The backside is patterned **B**. PDMS is spin coated on the front side and patterned. **C**. A sacrificial layer (100 µm) is constructed to form the microchannel. **D**. A second layer of PDMS is spin coated enveloping the sacrificial layer. **E**. Silicon and SiO2 are etched away to form the culture well and microfluidic inlet/outlet. **F**. After etching, the channel is fully formed. **G**. The device is inverted to the correct orientation. Yellow arrows indicate intended fluid flow vectors. Adapted from Ref. [43].

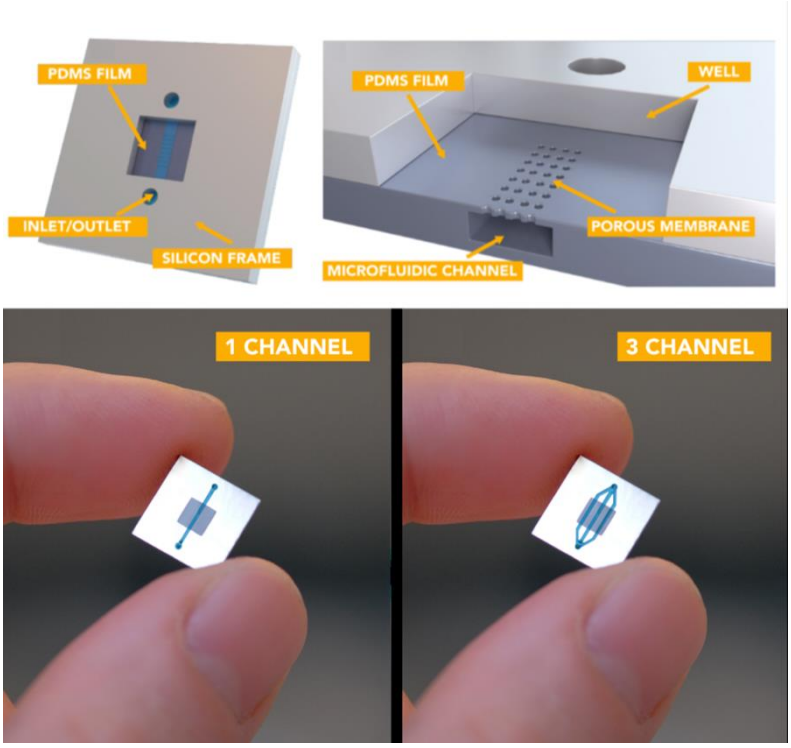

Figure 1.5 Representative computer renderings and examples of final BI/OND OOC platforms. **Top**. Schematic of final microfabrication product with section focusing on the culture well, microfluidic channel, and porous membrane. Image not scaled. **Bottom**. Images of two BI/OND platform variations, a 1 channel and 3 channel microfluidic layout. Adapted from Ref. [43].

1.3 Thesis Contribution

Despite the progress and innovation witnessed in this expanding field of 3D microfluidic culturing, not only are true *in vivo* conditions still not fully emulated *in vitro*, but methods for observing and quantifying are yet to achieve a fully agnostic state. Many *in vitro* models require either simulative approximations or mathematical models to predict and confirm experimental results, or the measurement methods they use introduce uncertainties unique only to engineered systems. To provide a few examples, various attempts have been made either to integrate biosensors passively into culture systems, to generate simulations of dynamic cell systems, or to directly measure *in vivo* systems using minimally invasive techniques, such as confocal microscopy or micro-particle image velocimetry (µPIV) [47]–[50]. Such methods require complex development of intricate, integrated platforms, simplifying assumptions to complete simulation work, or introduction of non-native elements, such as fluorescent dyes or microparticles, which potentially introduce unknown effects. Ultimately, the demand for truly bystander observation is still present. While confocal microscopy is a notable tool, its imaging capabilities are limited by sample preparation, long imaging durations that are unable to be performed in real time, and shallow imaging depths [51].

The intention of this thesis work is to introduce the OOC field to an imaging technique that better addresses some of these limitations; it is also the goal to perform initial quantifications of conditions in the BI/OND platform. Optical coherence tomography (OCT) is an imaging technique already available to the biomedical field that overcomes the previously mentioned barriers. This interferometric imaging method makes use of visible, coherent light as a measurement probe in a similar fashion that ultrasound utilizes high frequency sound waves to reconstruct structural information based on measurement of interfering, backscattered waves. Moreover, through the implementation of Doppler shift principles to electromagnetic waves, it is also feasible to characterize fluid flow profiles between adjacent microcompartments and microfluidic channels without the need for foreign dyes, microparticles, or additional sample preparation.

Preliminary observations have confirmed in a limited fashion that flow through the microchannel underneath the upper culture well follows simulation predictions. However, the resolutions of these measurements are low, and few of the underlying parameters thereof have yet been fully explored. Thus, the main effort of this thesis research will focus on determining the optimal measurement parameters for both the OCT system and the microfluidic conditions for fluid flow characterizations. Once this goal is achieved, follow up experiments are performed to identify suitable conditions to match the demands from the intended use of the BIOND microfluidic chips. These restraints and aims and have been delineated into three main objectives:

- Establish and optimize imaging and measurement protocols to fully characterize fluid flow profiles, specifically in the BIOND microfluidic chip
- Characterize the fluid flows and confirm adherence to simulated physical models
- Assess changes to flow profiles during introduction of organoid tissues

1.3.1 Thesis Outline

The subsequent thesis material is structured according to the following synopsis. Chapter 2 introduces the fundamental concepts behind interferometric methods through the use of interference of waves. This chapter is concluded with a discussion of the measurement technique OCT and D-OCT and some of the theory behind the measurements. In Chapter 3, the methodology, microfluidics, and experimental setup are overviewed. Chapter 4 addresses the results achieved during this thesis, investigating fabrication material impacts on OCT, fluid profile measurements, and the impact of organoid-like bodies on BI/OND culture flows. Lastly, Chapter 5 concludes the results of this thesis work and contains recommendations for future research.

Chapter 2

Interferometry and OCT

In this chapter, first the theory of interferometry and basic measurements of optical coherence tomography (OCT) will be discussed. Low coherence (i.e. white visible light) interferometry techniques, along with rapid signal processing methods, have greatly advanced the field since OCT's first applications in the 1990's [52]. Some of these advances are algorithmic, such as the transition from time domain (TD) measurements to simultaneously reading magnitude and phase parameters from the spectral domain (SD), or also referred to as Fourier domain (FD) [53]. In particular, OCT coupled with Doppler effects, Doppler OCT (D-OCT), is an advanced implementation of OCT utilized to measure fluid velocities; for example, Doppler-based techniques have been quite useful for understanding biological systems such as *in vivo* hemodynamics and tissue microcirculation without any perceivable impact on the observed systems, and all measurements are performed in real-time [54]. Appropriately, the precise theory of D-OCT is discussed at the end of this chapter. In this work, D-OCT is used to directly observe fluid velocities and flow profiles in the BI/OND platform – a unique approach to membrane diffusion characterization not often used in such microsystem platforms and, to the author's knowledge, never in OOCs.

2.1 Interferometry

While the theory and observation of interferometric phenomena have been present in scientific pursuit and everyday life: Newton first observed and attempted to describe interference fringes in a thin air film between two glass plates – "Newton's Rings," [55], and colorful soap films or oil slicks are commonplace today. Interference spectroscopy, specifically, began gaining usage and broadening its applications at the end of the 19th century, in large part due to the development of Fourier transform spectroscopy, which eventually permitted for mapping of complex spectra instead of only measuring signals over time. A quarter of a century later, Einstein's theories on light helped fuel the development of advanced light sources (e.g. lasers), which removed limitation of low spatial and temporal coherence in light emissions used for imaging. The combination of these technological advancements resulted in higher accuracy and an expansion of various interferometry techniques. In the modern era, rapid progress in

electronic hardware (e.g. photodetectors, digital computers, fiber optics) have given even more capturing power to interferometric methods [56], [57]. A more in depth over and discussion of the current states of interferometry, and specifically optical interferometry, may be found in work by P. Hariharan.

Interferometry is the utilization of the overlap and summation of waves – typically electromagnetic waves, although acoustic waves, which are also used in a range of techniques [58], and water waves exhibit the same qualities – to discern specific sets of information regarding a scanned sample [59]. Waves follow the principle of linear superposition, which is the concept that when two separate waves interact in space, the resultant wave form is the summation of the two interacting waves if each respective wave were to progress through the same medium individually [60]. In two extreme cases fully constructive interference and fully destructive interference patterns, the waves' phases are offset by even multiples of π radians (180°) and odd multiples of π radians. Even more recently, superposition phenomena have gained notoriety in the field if quantum mechanics to describe superconducting states in quantum computing applications [61], [62].

Typically, in the application of interference principles in interferometry, waves propagate from a single source, therefore possessing the same phase, amplitude, and frequency characteristics. Upon encountering a surface of an object or traversing between mediums, specific parameters are altered as a result of such interactions. The example of light bending through a glass of water creating the illusion that a straw is in two separate, disjoint locations is commonplace, which exemplifies the transition between air and water and the resulting shifts in wavelength of reflected light. Under more controlled situations, these changes in qualities can be used to extract information of the medium or object. In order to measure and quantify these alterations, many interferometric methods have been developed over the last century [57]. The most common methods involve comparing a reference beam to a sample beam and investigating shifts in complex frequencies or phase shifts to elucidate differences in optical path lengths.

2.2 Optical Interferometric Techniques

Many interferometric systems implement optical arrangements that cause two beams, originating from the same source, but have travelled through different paths, to interfere at a final point or surface of measurement. One path is designated a reference beam while the other is the sampling, or test, beam. In a similar way that light will have phase shifts when traversing different mediums and consequently travel different lengths, interferometers will measure the difference in optical path length to calculate a phase shift between the reference beam and sample beam. The magnitude of phase shift can be connected to a physical distance (i.e. points of reflection on a rough surface of a sample) and the refractive index of a sample. Due to the fact that a standing interference pattern must be created for accurate measurements, both the reference beam and sample beam need to be of the same frequency. This is achieved by using a single light source and dividing a collimated beam to create two identical beams, either through wavefront division, which physically separates a single beam with a screen with adjacent pinholes, or through amplitude division, which uses beam splitting methods, such as a beam

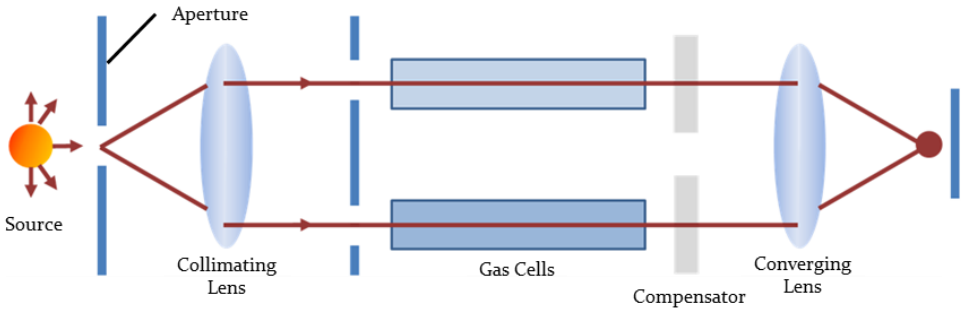

Figure 2.1 Simplified representation of Rayleigh interferometer. Adapted from Ref. [63].

splitter, diffraction grating, or a polarizing prism [56]. Here, a few different interferometers are discussed; the Michelson interferometer will be covered in most detail as it is the style of machine used for this thesis work.

In a Rayleigh interferometer, a canonical example of wavefront division, beams from a single source are divided using two apertures to diffract beams through two parallel glass, gas cells [63]. These cells can be filled with a reference gas, sample, gas, or placed under vacuum. The beams are directed through the cells and onto a detection plane using focusing lenses. By adjusting the angle of inclination of one of the two lenses, the optical paths can be equalized; through this, interference patterns can be observed and measured. Rayleigh interferometers are ideal for determining the refractive index of gases.

Most other interferometers make use of amplitude division. For instance, a Mach-Zender interferometer implements pairs of two beam splitters and two mirrors to divide and direct the beams, respectively. The degree and location of overlap between the reference and sample are controlled by varying the lateral position of the beams as well as the angle between the beams when exiting the interferometer (Figure 2.2A). Another popular interferometric setup is the Sagnac interferometer. Here, two beams two beams follow the same path, but in opposite directions. The number of mirrors is also adjustable, as see in Figure 2.2B.

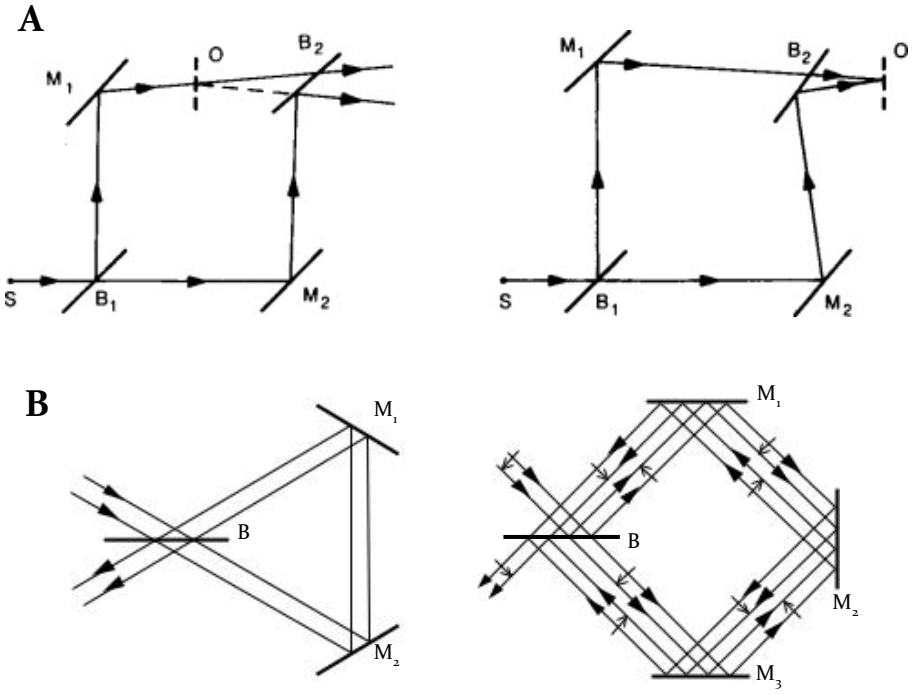

Figure 2.2 Examples of amplitude dividing interferometers. **A.** Localization of friends in the Mach-Zehnder interferometer. **B.** Two forms of the Sagnac interferometer. M: mirror; O: observation screen; B: beam splitter. Adapted from Ref. [56].

In the following sections, the theory of optical coherence tomography and its implementation using the Michelson interferometer is expounded.

2.3 Optical Coherence Tomography

Optical Coherence Tomography is an interferometry method that has developed into a major staple of biomedical imaging and medical diagnostic applications [64]. Through the use of low coherence, high intensity visible light, OCT permits for high-resolution cross-sectional and three-dimensional imaging *in situ* and in real-time, with feature resolutions of up 1 – 15 μm [65]. Furthermore, for highly scattering tissues, depths of approximately 2 mm have been imaged while along the order of 2 cm depths in transparent tissues, such as retinal tissue or embryonic sacs [66], [67]. This is achieved through the analysis of the magnitude and time delays of backscattered light, a concept that will be expounded upon further in this chapter. OCT's ability to characterize intact, non-excised tissues in real-time using

"optical biopsies," has resulted in its wide spread use in the medical field, such as in highly delicate organs, in histopathological diagnoses, and in guiding interventional procedures (e.g. microsurgeries), as well as in non-medical applications, including non-destructive testing and evaluation of materials (NDT/NDE) [68], [69]. A more extensive list can be found in Appendix A.

Within the context of medical imaging, OCT fills the gap between ultrasound and high-frequency laser methods such as confocal microscopy. Ultrasound scans in clinical settings exhibit lateral resolutions of the order 0.1 to 1 mm with imaging depths of up to several centimeters. Scanning resolution can be approved upon by using significantly higher frequencies (ca. 100 MHz), but this results in a large trade-off in imaging depth, which drops to only millimeters [65]. The same can be said of fluorescent microscopic techniques, which have resolutions of 1 µm or finer, but, due to the high rate of scattering in biological tissues, only have imaging depths of approximately a few hundred microns [70]. Further complications arise in confocal microscopy due to the necessity of long exposure times; the technique's high resolution, in part, derives from the exclusion of out of focus light *via* a spatial pinhole. Signal strength is diminished as a result, thus requiring long exposures to collect enough signal from the focal plane [51]. OCT, in comparison, and as mentioned above, has a penetration depth on the order of several millimeters and lateral resolutions around order 1 to 10 microns. These qualities are summarized in Figure 2.3. In the adjacent plot, more imaging techniques are shown with evaluations of their respective invasiveness and imaging speeds [70]. As it can be seen again, OCT fulfills requirements for a fast, high-resolution imaging method at moderate penetration depths, features that ultrasound and confocal microscopy each are lacking, respectively.

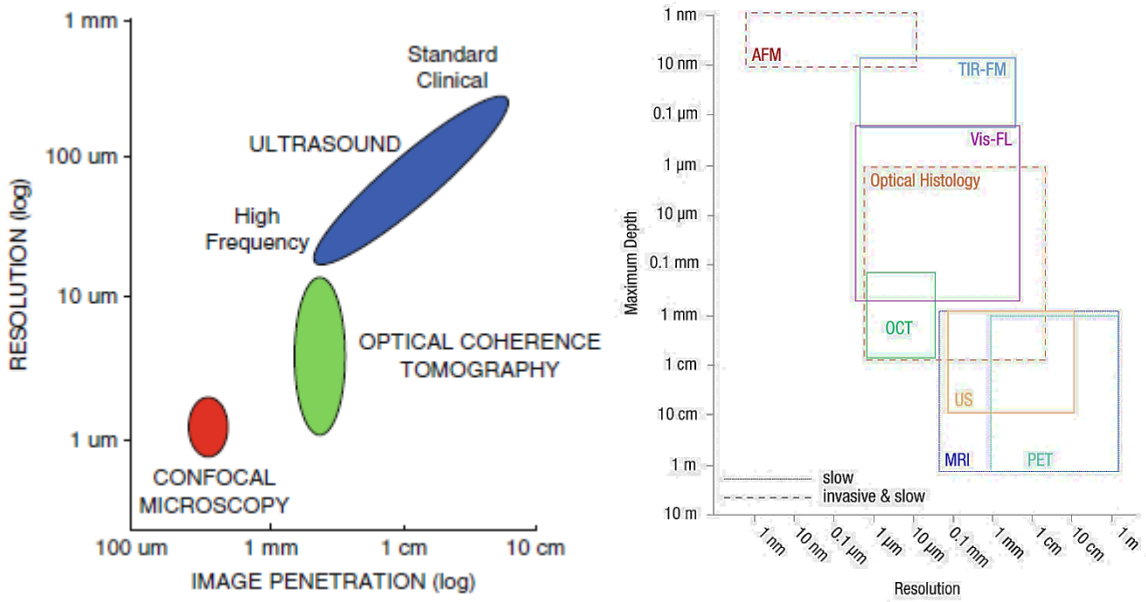

Figure 2.3 Comparison between different (medical) imaging techniques' imaging resolution, imaging penetration (i.e. maximum depth), (patient) invasiveness, and speed of imaging. **Left**. Plot of resolution against image penetration depth. Higher resolutions are obtained at a sacrifice to imaging depth. **Right**. Plot of maximum attainable imaging depth against image resolution with further distinctions between "slow" rates of image acquirement (boxes of solid lines) and "invasive & slow" imaging (boxes of dashed lines). AFM: atomic force microscopy; TIR-FM: total internal reflection fluorescence microscopy; Vis-FL: visible and fluorescent microscopy; OCT: optical coherence microscopy; US: ultrasound; MRI; magnetic resonance imaging; PET: positron emission tomography. Adapted from Refs. [65], [70].

2.3.1 A-Scans

An A-scan, or a single line scan at a point of interest along the surface of the object, a "one-dimensional" (1D) scan, is the simplest unit of data that can be acquired from an OCT machine. Through analysis of the phase shift data of the generated inference patterns, 1D scans provide information subsurface content at the point of interest. Wider spectra distributions containing more waves at both higher and lower frequencies, consequently, will have a distribution of penetration depths; as a result,

polychromatic light can be utilized to gather useful depth information. Analogously, low frequency waves or "slow" variations in reflected light frequencies, indicate shallow reflective events while narrow spectra distributions (i.e. "fast" variations) correspond to object features at deeper light penetrations. A typical signal distribution in a tissue scan is show in Figure 2.4. Notice that the backscattering is larger at the surface of the tissue while the intensity decreases as the penetration depth increases. This is due to less of the sample beam returning along its original path of origin. When recombined with the reference beam, which travels along a path of know length and reflects off of a plane mirror, providing low-noise heterodyne detection in FD-OCT [71]. Due to the fact that the position of the reference arm is known and can be set in the system, differences in phase between the original signal and the sample may be extracted to determine axial positions of reflection in the scanned sample. The computational process of getting to a final A-scan from raw intensity spectra is generalized in Appendix B-1.

2.3.2 B-Scans

By transversely scanning the incident optical beam and performing sequential measurements of a series of points – simply said, multiple A-scans, or M-scans – two-dimensional (2D) representations of optical backscattering may be generated, also known as a B-scan (Figure 2.4). The cross-sectional datasets are visually represented using gradated gray scales or false color images [65]. Similarly, sequential B-scans may be stitched together to create three-dimensional (3D) volumetric scans, a comparable process to that of confocal microscopy. Such reconstructions are referred to as C-scans. All methods of basic OCT scans are summarized in Figure 2.4.

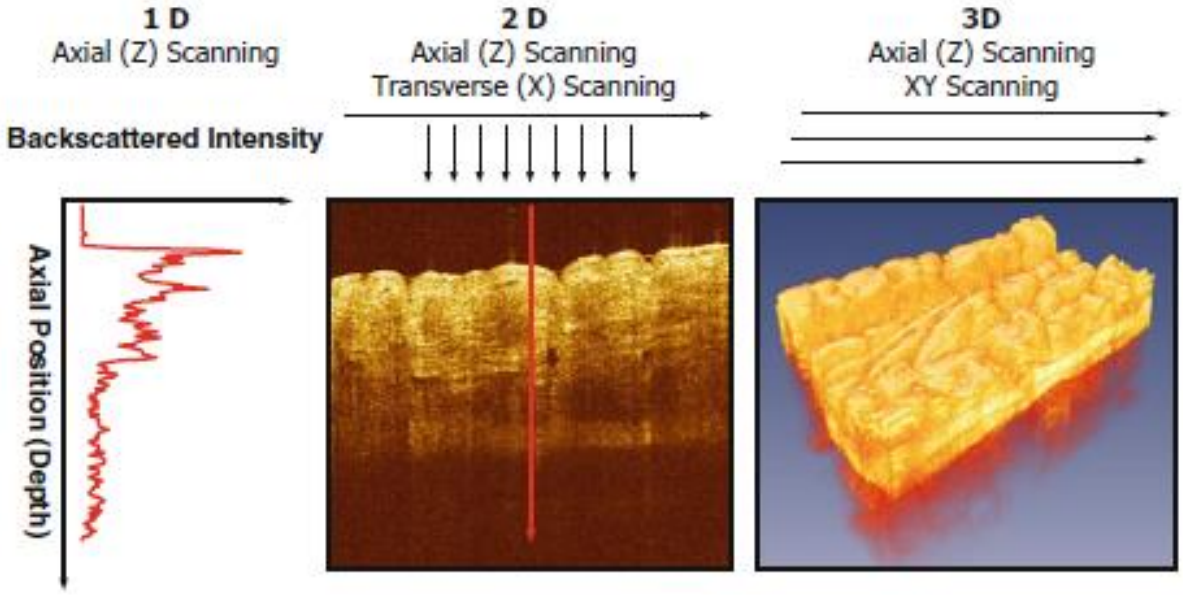

Figure 2.4 Examples of different scanning modes and data acquisition using an OCT system. The 2D and 3D images are formed from scans of the top dermal layers of skin. Adapted from Ref. [65].

As B-scans will be a major portion of the following work, a more detailed process is shown in Figure 2.5. Briefly, when a line scan is selected, that length is divided into the number of corresponding pixels measured by the photodetector. This dictates the number of A-scans connected to the B-scan and B-scan image. An appropriate number of A-scans are filtered and calculated to form an array of values mapping to the length and depth of the B-scan. These data are converted to decibels and scaled to the maximum signal value of the B-scan. Finally, the scaled image is colorized and plotted as the final B-scan in Figure 2.5.

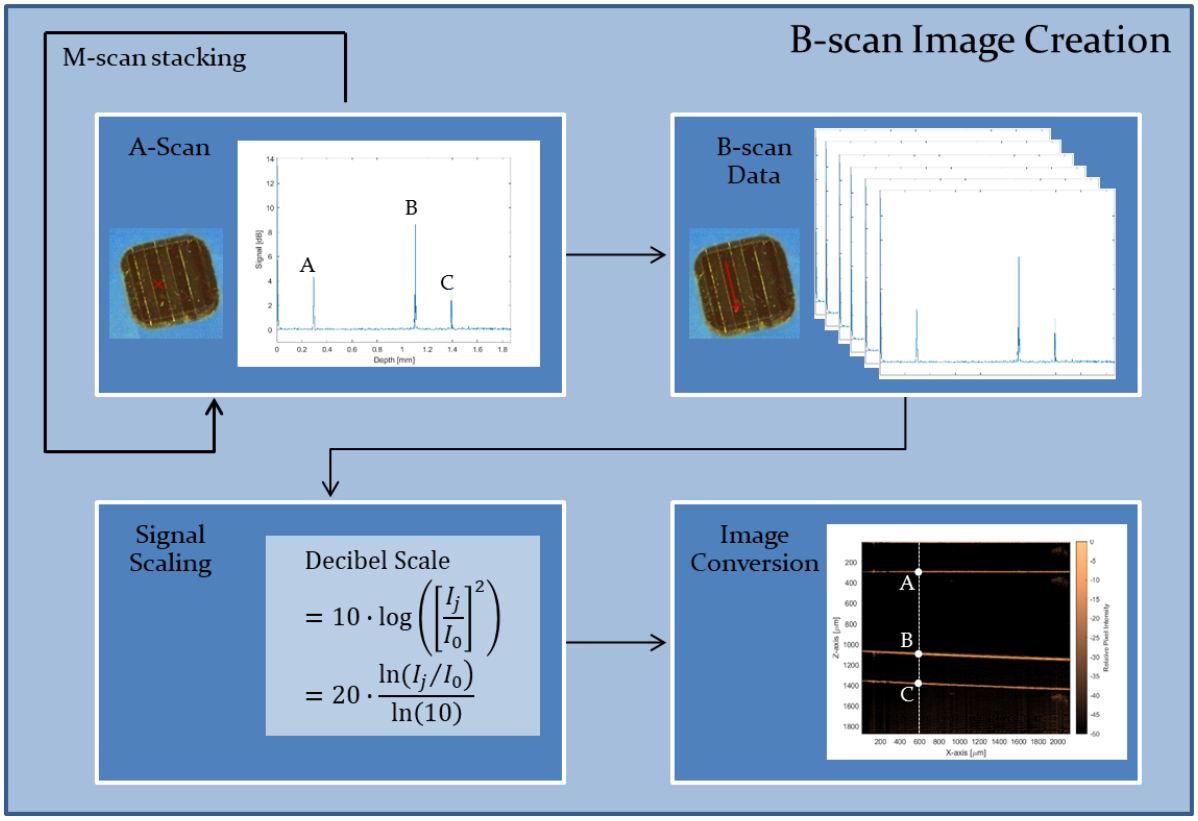

Figure 2.5 Schematic picturizing the creation of a B-scan image, beginning with A-scan data. A-scans are iteratively calculated along the scan path of interest (M-scan stacking), which when packaged together, constitute a B-scan. This signal data is converted to the decibel scale, which is relates the power of a signal (I_j^2) to a linear trend (1 Bel (B)= $\frac{1}{2}$ln (10) nepers (Np)). The data matrix, as B-scans are two dimensional, is scaled and plotted as a colorized image. Shown is the connection between the initial A-scan and the final B-scan through points A, B, and C.

2.4 Michelson Interferometers

2.4.1 Interferometer Setup

The three basic requirements for an OCT system are an interferometer – which can also be referred to as a beam splitter – a broad band, visible light source, and a photodetector. While these components may be arranged in varying configurations with increasing complexity and additional elements, this work focuses on what is called a Michelson Interferometer, which was used by Dr. Albert Abraham Michelson in his efforts to measure the speed of light, for which he was eventually awarded the Nobel Prize in Physics [72]. The minimal Michelson interferometer setup employing spectral-domain detection is show in Figure 2.6. OCT measures interference fringes (i.e. the constructive and destructive interference of waveforms) incident on a photodetector after two beams of light return from the reference arm and the sample arm (Figure 2.6). Emanating from the low coherence light source (typically of a Gaussian distribution of waveforms centered about a central wavelength λ_0), high intensity, visible light is fiber-optically directed through a 2 × 2 fiber coupler, which divides the optical power of the beam in a 1:1 ratio to both the reference arm and the sample arm. In TD-OCT, the reference arm is mobile and can be scanned along the light path, thereby controlling the optical depth at which peak interference occurs in time; in SD-OCT, however, the reference mirror is fixed, and spectral peaks are obtained through Fast Fourier Transforms (FFT) during computational processing. Both styles of systems contain the lateral scanning mirrors to control the field of view (FOV) in the sample arm. Backscattered or reflected light re-enters the respective fiber-optic paths to return to the 2 × 2 fiber coupler, where the two beams are mixed before traveling to the photodetector. As a result of the different optical paths, a heterodyne frequency is observed which provides both scattering strength

and position information. The photodetector, which in this case follows a squared-sum, summing the squares of each electric field incident upon it, converts the electromagnetic signal into an electrical current, which can then be further processed into A-scans, B-scans, etc. This process is diagramed in Figure 2.6. The mathematics of converting signals obtained from the photodetector is discussed later in this work.

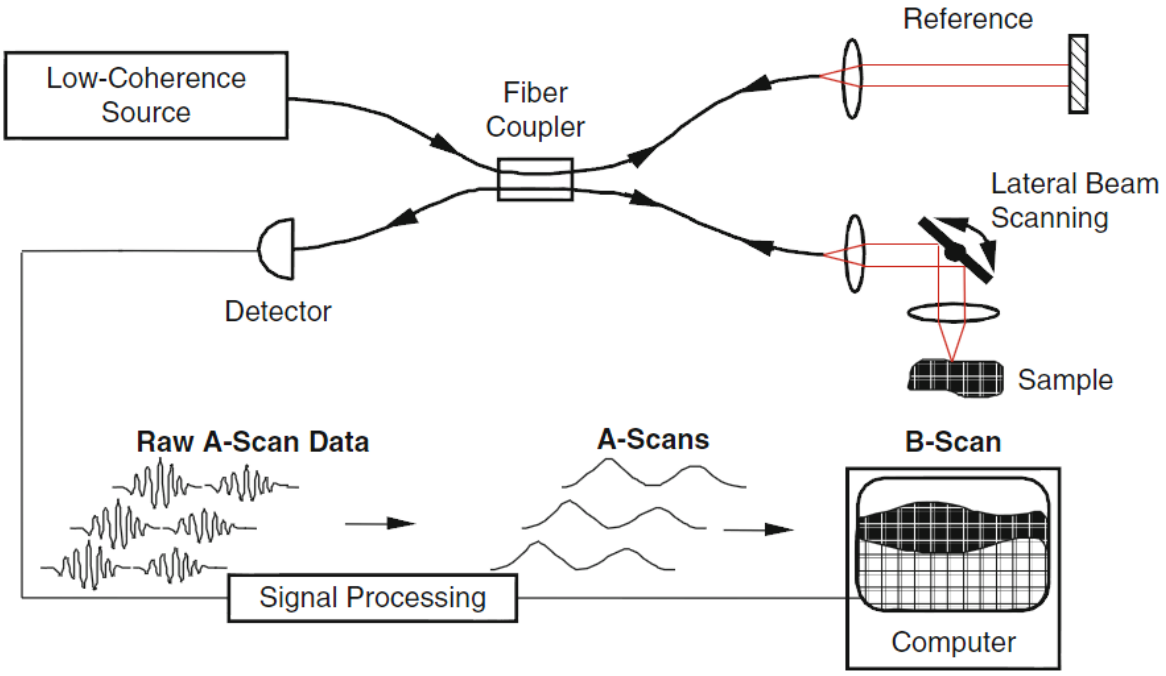

Figure 2.6 An example of a low coherence, fiber-optic interferometer using a Michelson arrangement. Light exits the source as a collimated beam and is directed by a beam splitter (i.e. fiber coupler) to both the reference mirror and the sample. The backscattered light from both paths are interfered and measured by a photodetector. The reference mirror is fixed in this spectral domain case. Bold lines indicate fiber-optic paths, red lines represent free-space optical paths, and thin lines represent electronic signal paths. Adapted from Ref. [72].

2.4.2 Theory of Michelson Interferometer

Due to the fact that light waves travel with frequencies on the order of terahertz (10^{14} periods per second), photodetectors in these systems must measure electrical fields rather than the impingent wave intensity. Such waves can be represented as cosine functions that aid in the visualization of such waves, as shown in Eq. 1, which also shows the relation between the intensity and the two interfering waves at the photodetector [56],

$$I_0(k,\omega) \sim |E_i|^2 = [E_r(t) + E_s(t)]^2$$
$$= |E_r|^2 + |E_s|^2 + 2 \cdot E_r \cdot E_s \cos(\omega t - kz) \qquad (1)$$

where I_0 is the intensity of the incident light on the photodetector which is proportional to the square of the total electric field; t is time; z is the direction of propagation; ω is the angular frequency ($\omega = 2\pi\nu$, where ν is beam frequency); E_i, E_r, E_s, are the electric fields of the light source, the reference beam; and the sample beam, respectively; k the wavenumber ($\frac{2\pi}{\lambda}$, where λ is beam wavelength); and ΔL is the path length. Equation 1 may be rewritten in a complex form as show in Eq. 2, which makes mathematical manipulations easier due to their linear properties, which are also shown in Figure 2.7 [73].

$$E_i = s(k,\omega)e^{i(kz-\omega t)} \qquad E_r = \frac{E_i}{\sqrt{2}}\left[r_r e^{i2kz_r}\right] \qquad E_s = \frac{E_i}{\sqrt{2}}\left[r_s(z_s) \times e^{i2kz_s}\right]$$
$$I_0(k,\omega) \sim |E_r + E_s|^2 = \left[s(k,\omega)e^{i(kz_r-\omega t)} + s(k,\omega)e^{i(kz_s-\omega t)}\right]^2 \qquad (2)$$

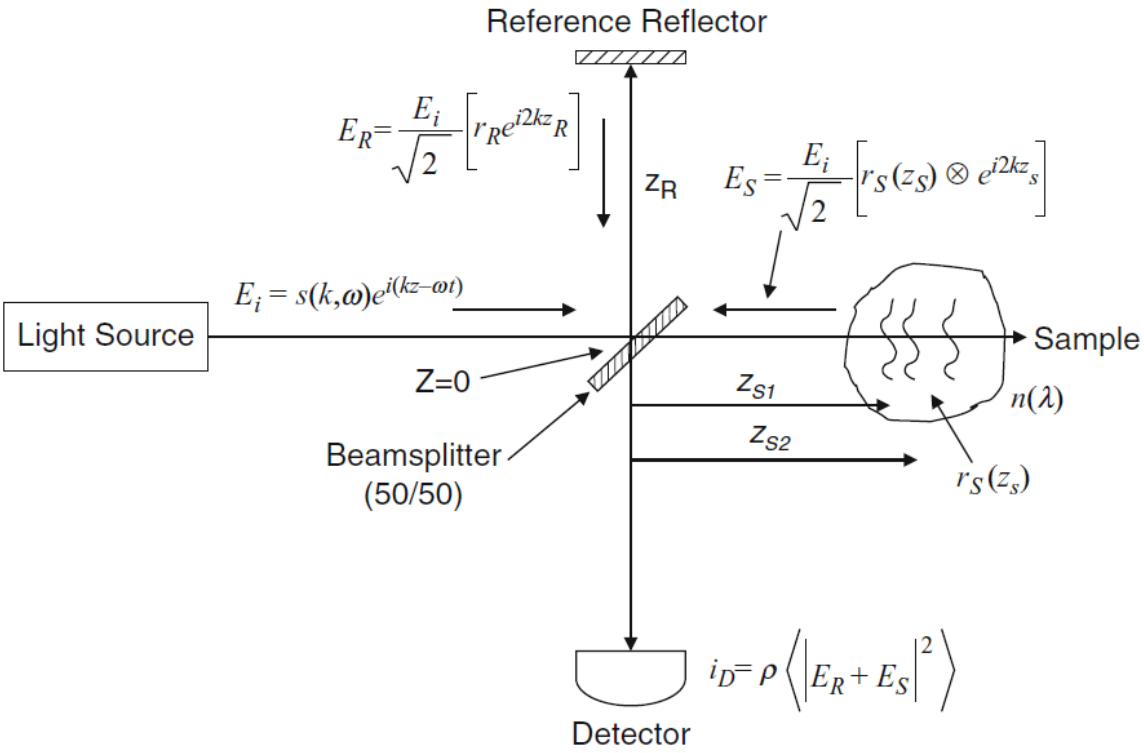

Figure 2.7 Visualization of mathematical relations between the electrical fields of the light source E_i, the reference reflector E_R, and the sample E_s, and photodetector intensity (i_D) for a Michelson interferometer setup. Z_N represents distance from the beam splitter (Z_0), in the direction of the reference reflector (Z_R), and in the direction of the sample (Z_{s_n}). Adapted from Ref. [73].

The electric field complex amplitude is represented by $s(k,\omega) = ae^{i\left(\frac{2\pi n(\lambda)z}{\lambda}\right)}$, where $n(\lambda)$ is the wavelength-dependent refractive index and a is the signal amplitude; the product $n(\lambda)z$ represents the optical path length p with z in this case representing a physical length. Wavelength λ and frequency ν are coupled according to $\frac{c}{n(\lambda)} = \lambda\nu$, where c is the speed of light under vacuum. Reference reflector and sample depth-dependent electrical reflectivity's, r_r and $r_s(z_s)$, respectively, are related to power reflectivity by $R_r = |r_r|^2$ and $R_s(z_s) = |r_s(z_s)|^2$, respectively. The cross-product operator is indicated by "×".

Through mathematical manipulations of these equations, the importance of the surrounding mediums' optical properties (e.g. reflectivity's, refractive indices) can be connected to physical distances in regards to the sample. As put in the MIT Professor Dr. James G. Fujimoto's book – the proverbial father of OCT in biomedical applications: "The reconstruction of the function $\sqrt{R_s(z_s)}$ from noninvasive interferometric measurements is the goal of low-coherence interferometry in OCT" [73]. By calculating the value of this function, optical path lengths of all major reflection events in the sample may be calculated, shown in the expanded function.

$$\sqrt{R_s(z_s)} = |r_s(z_s)| = \left|\sum_{n=1}^{N} r_{s_n}\delta(z_s - z_{s_n})\right| \qquad (3)$$

For clarity, $r_s(z_s)$ may be both continuous and discrete; the discrete form serves partially as a didactic tool, as shown in Eq. 3, suggesting that each interface between adjacent mediums will behave as single, separate reflectors, where n is the n'th pixel of N pixels. This is seen as δ represents the Dirac delta function, providing power at "point" reflectors at specific optical paths with respect to the reference reflector. In practice, N is the number of points per A-scan, and an intensity-depth plot may be generated, as in Figure 2.4 and Figure 2.5. The presence of Eq. 3 may be seen after expanding and simplifying Eq. 2 to achieve the follow relation

$$
\begin{aligned}
&I_o(k) \sim S(k) \cdot \left(R_r + R_{s_1} + R_{s_2} + \ldots\right) && \textit{"DC Terms"} \\
&+ S(k) \sum_{n=1}^{N} \sqrt{R_r R_{s_n}} \left(e^{i2k(z_r - z_{s_n})} + e^{-i2k(z_r - z_{s_n})}\right) && \textit{"Cross-correlation Terms"} \\
&+ S(k) \sum_{m \neq n=1}^{N} \sqrt{R_{s_n} R_{s_m}} \left(e^{i2k(z_{s_n} - z_{s_m})} + e^{-i2k(z_{s_n} - z_{s_m})}\right) && \textit{"Auto-correlation Terms"} \quad (4)
\end{aligned}
$$

where $S(k) = \langle |s(k,\omega)|^2 \rangle$, the power spectra of the light source. Typically in modelling light source spectra, Gaussian-shaped curves are used due to their near recapitulation of actual light source power distributions; for further detail on such characterizations, refer to the text of Fujimoto [74]. Three distinct components of the photocurrent generated by the squared-law photodetector, which can be delineated by direct current "DC", "Cross-correlation", and "Auto-correlation" terms, as referenced in Eq. 4. The total photocurrent $I_0(k)$ is preceded by factors related to the photodetector responsivity ρ, such that $i_D(k) = \frac{\rho}{4} I_0$, with $i_D(k)$ representing the actual photocurrent. All terms are time invariant as well. First, the DC terms are associated with a constant length offset, which is mainly driven by the power reflectivity R_r as $R_r \gg R_{s_n}$. Here is where the role of the reference beam can become detrimental, as too strong a signal will result in large signal offset during scanning. However, as seen in the cross-correlation team, R_r also provides power to the sample signals and to the main function of OCT measurements $\sqrt{R_s(z_s)}$. Thus, setting a balance between R_r and R_s is critical to clean measurements. Lastly, similarly, the auto-correlation terms are present as a result of interference patterns from reflections between sample layers, and must be appropriately "tuned out" by selecting an appropriate reference power reflectivity ρ, either through material selection or adjustments of the light source outputs. A full derivation may be found in Appendix B-2.

The derivation of these relations allows for the intelligent design and assessment of OCT experiments. The FFT of Eq. 4 may essentially be equated to an A-scan, thus giving experimenters a model from which to interpret their results.

2.4.3 Doppler Theory in OCT

Optical coherence tomography, since its initial applications in ophthalmology, has grown in scope and application, driving the creation of many variations on the original principal of an optical biopsy. By introducing the principles of Doppler shift – the perception by an observer of a change in frequency by a moving object, typically sound waves come to mind – OCT measurements can also be to elucidate velocity information in particular systems [75], [76]. In an analogous manner, in which the Doppler shift is proportional to the difference in speeds between the signal source and the observer, shifts in the phase of a sample beam in relation to the reference beam in the Michelson interferometer can be equated to scanned particles in motion. Below, an abridged derivation is shown in order to grant the reader some understanding of how such calculation are achieved; A full derivation is shown in Appendix A-3. The final velocity equation is show in Eq. 5.

$$\boldsymbol{V}\cos(\theta_s) = \frac{\boldsymbol{\lambda}_0}{4\pi}\frac{\Delta\phi}{\Delta t} \tag{5}$$

Here, θ_s represents the Doppler angle, which is the horizontal angle between the velocity vector and the impinging light wave; λ_0 is the vacuum centered wavelength of the light source; $\Delta\phi$ is the change in phase between sequential A-scans; Δt is the time between sequential A-scans ($\frac{1}{\Delta t}$ can be considered the same as the scanning rate of the OCT machine); $\boldsymbol{V}$ is the velocity magnitude of the measured particle. Inherent to the above equation (Eq. 5), there must be an angle between the moving constituents and light source, otherwise no velocity is detectable.

By considering the scanning light source and the returning backscatter as anti-parallel waveforms, one can derive a relationship between the frequency at the photodetector and the two former values, as show in Eq. 6

$$f_d = \frac{1}{2\pi}(\mathbf{k}_s - \mathbf{k}_t)\cdot\boldsymbol{V} \tag{6}$$

in which, $\boldsymbol{\kappa}_s$ and $\boldsymbol{\kappa}_t$ are wavelength vectors, in the form $|\boldsymbol{\kappa}| = \frac{2\pi}{\lambda}$, of the incoming and scattered light, respectively; f_d represents the electrical field frequency at the photodetector. These values are shown in Figure 2.8.

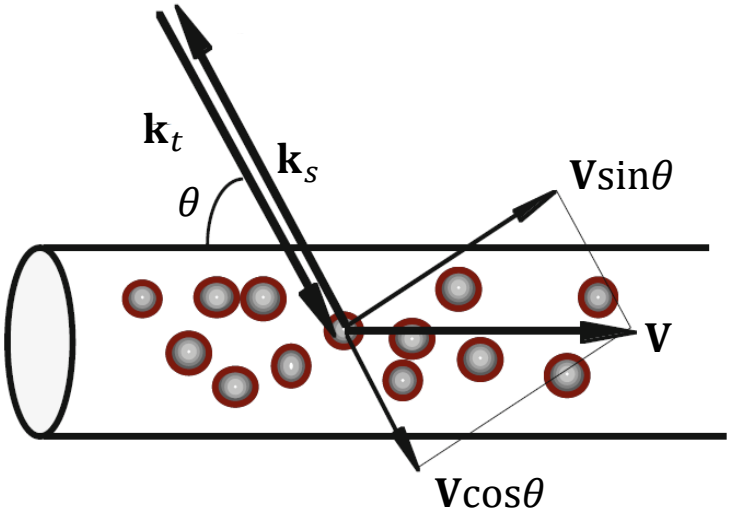

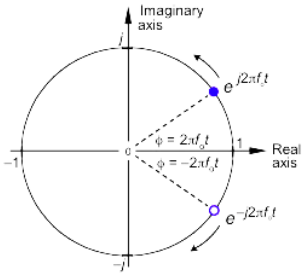

Figure 2.8 Left: Simplified diagram of particles flowing through a circular tube under observation by OCT. Only light returning along the original path of impingent light is observed by the OCT machine. **Right**: graphical representation of complex signals, where j is $\sqrt{-1}$. Adapted from Ref. [76], [77].

By expanding and carrying out the vector product in Eq. 6, detector frequency may be directly related to particle velocity. However, as mentioned previously, the high frequency of light makes it impossible to accurately measure such parameters. Thus, in order to overcome this equipment limitation, it may also be said that the frequency f_d at the detector takes the form $f_d = \frac{1}{2\pi}\frac{\Delta\phi}{\Delta t}$, which is a result of the relation between the wave phase shift and frequency in the complex plane, $\phi = 2\pi f t$ (Figure 2.8) [77]. By relating the two definitions, a final equation (Eq. 7) is obtained that connects complex phase shifts in the beat wave to particle velocity

$$\frac{2V\cos(\theta_s)}{\boldsymbol{\lambda}_0} = \frac{1}{2\pi}\frac{\Delta\phi}{\Delta t} \tag{7}$$

Which can be rearranged to arrive at Eq 5. Time and wavelength parameters are determined by equipment specifications – typical scanning rates are $O(10^3 - 10^4)$ Hz and (central) wavelengths are set

by the type of light source – while changes in phase $\Delta\phi$ must be calculated from OCT measurements. This can be accomplished one of two ways. First, differences in average phase shift in sequential A-scans at the *n*'th pixel may be determined by analyzing the interference fringes at the detector, as follows:

$$f_d = \frac{\Delta\phi}{2\pi\Delta t} = \frac{1}{2\pi\Delta t} \sum_{m=(n-1)M}^{nM} \sum_{j=1}^{N} \left[\tan^{-1}\left(\frac{Im\left[\widetilde{\Gamma}_{j+1}(t_m)\right]}{Re\left[\widetilde{\Gamma}_{j+1}(t_m)\right]} \right) - \tan^{-1}\left(\frac{Im\left[\widetilde{\Gamma}_{j}(t_m)\right]}{Re\left[\widetilde{\Gamma}_{j}(t_m)\right]} \right) \right] \quad (8)$$

Here, *M* is the window size, limited to even numbers, in the axial direction for each one of *N* A-scan's; *j* is the *j*'th A-scan; and, *Im* and *Re* are the imaginary and real components of the complex signal $\widetilde{\Gamma}_j$. A second, cross-correlation method may also be implemented, shown in Eq. 9. This is the method implemented during this thesis work, whose details will be explained in Chapter 3.

$$f_d = \frac{\Delta\phi}{2\pi T} = \frac{1}{2\pi T} \tan^{-1}\left(\frac{Im\left[\sum_{m=(n-1)M}^{nM} \sum_{j=1}^{N} \widetilde{\Gamma}_j(t_m) \cdot \widetilde{\Gamma}^*_{j+1}(t_m)\right]}{Re\left[\sum_{m=(n-1)M}^{nM} \sum_{j=1}^{N} \widetilde{\Gamma}_j(t_m) \cdot \widetilde{\Gamma}^*_{j+1}(t_m)\right]} \right) \quad (9)$$

Chapter 3

Experimental Setup & Data Analysis

The experimental setup in this work is mainly composed of two systems interacting though the BI/OND microfluidic device. First, the BI/OND platform is highlighted in more detail. The aspiring laboratory tool involves several pieces and comes in a variety of formats. Second, the first system, the OCT aspect, involves generating high intensity, broadband visible light and, also, measuring the returning waves caused by scattering in the microfluidic device. And lastly, the second system, the liquid handling, controls flow conditions with the aim of creating flow patterns that most simulate conditions during cell or tissue culture. Both of these systems and their associated experimental protocols are summarized in this chapter. Concluding the chapter, the data processing is overviewed, covering some of the methods specific to this project and the BI/OND OOC.

3.1 BI/OND Organ on Chip Platform

3.1.1 BI/OND inCHIPit™

Two variations of the BI/OND OOC platform are used in this work, the inCHIPit-3C™ ("Tri-channel") and the inCHIPit-1C™ ("Mono-channel"), which are PDMS and silicon based microfluidic devices with three parallel microchannels and one microchannel, respectively. An exemplary rendering of the inCHIPit-1C™ is shown in Figure 3.1A,B. The inCHIPit™ structure is designed with the intent of growing multiple cell or tissue types while being physically separated by a porous membrane to permit various manners of cellular interactions, for example, diffusion of exocytosed cytokines (Figure 3.1C). Larger, macroscopic type samples, including organoids, *ex vivo* biopsies, spheroids, and microtissues, are able to be introduced to the main, upper culture well for culturing and experimentation (Figure 3.1D). These microfluidic devices are manufactured on 1 *cm* x 1 *cm* silicon inserts through clean-room validated microfabrication methods; refer to the introductory chapter for a review of the protocol and to work by Gaio *et al.* in *Organ-on-Silicon* for a fully detailed overview [43]. The height of the microfluidic

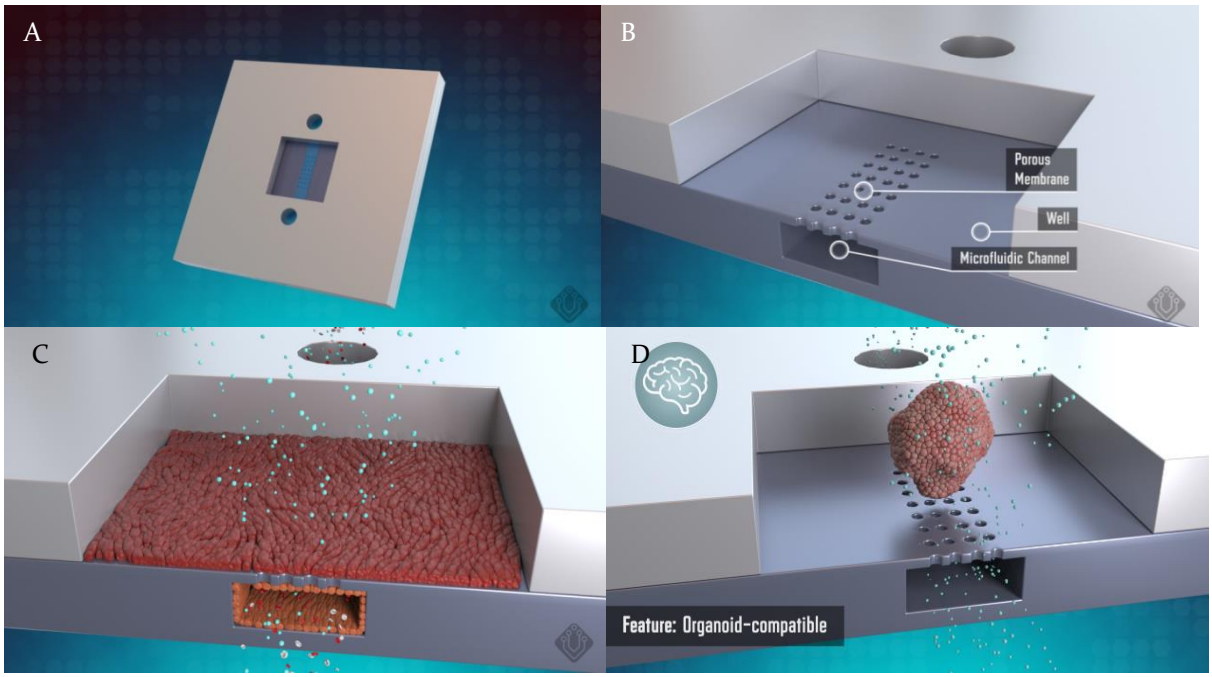

Figure 3.1 A. Computer rendered model of the inCHIPit-1C™ with microfluidic channel inlet and outlet in view. **B**. Zoomed in perspective of the cell culture well, identifying the microfluidic channel, the porous membrane, and the culture well. **A**. Idealized vision of a brain organoid experiencing diffusive effects as a result of fluid flow in the microfluidic channel across the underside of the porous membrane. **B**. Idealized vision of a co-culture system. Cells in the microchannel are endothelial cells that form to the form of the microchannel walls while in the culture well are epithelial cells. Cell metabolites and pass through the microfluidic channel and across the membrane. Graphics provided by BIOND, B.V.

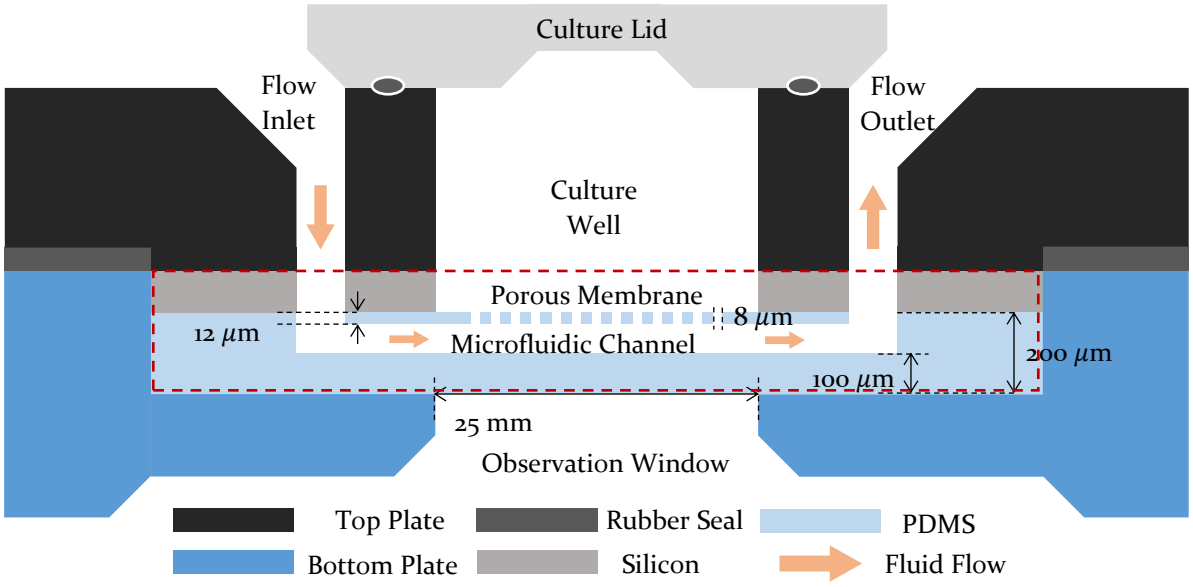

Figure 3.2 Cross sectional view of the assembled BI/OND inCHIPit™ device. The microfluidics rest in the base of the bottom plate, aligned with the inlet and outlet to allow microfluidic flows. The microfluidics are denoted by the red dashed outline. The culture well also aligns with the empty volume in the top plate to allow easy access to the porous membrane during cell culture. The culture lid along with the rubber ring seals and isolates the culture well during cell culture. The observation window enables microscopic observation. Diagram not to scale.

channels in both inCHIPit™ types are 100 ± 10 μm, while the width of the channels in the inCHIPit-3C™ are 300 ± 10 μm and the width of the channel in the inCHIPit-1C™ is 400 ± 10 μm. The length of the channel(s) freestanding from silicon support in both designs is ca. 25 mm. The diameter of the porous in the membrane are approximately 8 μm with a pore to pore distance of approximately 20 μm. Membrane thickness is about 12 μm [14]. The supporting PDMS walls between the microfluidic channels of the inCHIPit-3C™ estimated to be 0.7 ±0.1 mm wide, while the thickness of the support PDMS is 200 μm in both inCHIPits™ and the thickness of the PDMS below the channel is approximately 100 μm. The microfluidics rests in the center of the bottom plate and is secured *via* the top plate, which has an empty volume for culturing (Figure 3.2).

3.1.2 BI/OND Hardware Assembly

The BI/OND OOC assembly and its components are portrayed in Figure 3.3. There are four major pieces to the BI/OND device: the top plate, the microfluidic device (i.e. inCHIPit™), bottom plate, and the securing ring. Two forms of the top plate were tested, a dark (i.e. opaque) and a light (i.e. translucent) top plate (Figure 3.3A). The top of the top plate also forms the culture well where macroscopic tissues would be cultured, such as organoid models; this culture well is easily accessible for observation and tissue retrieval while also possessing the ability to be sterilely sealed. On the underside of the top plate, where the microfluidic device is placed, completing the microfluidic circuit, there is a rubber foil designed to evenly create an air and liquid tight seal to prevent spillage during culturing (Figure 3.3B). The top plate and inCHIPit™ are braced by the bottom plate which also has an observation window for microscopy observations and measurements (Figure 3.3C). An image of the BI/OND microfluidic device

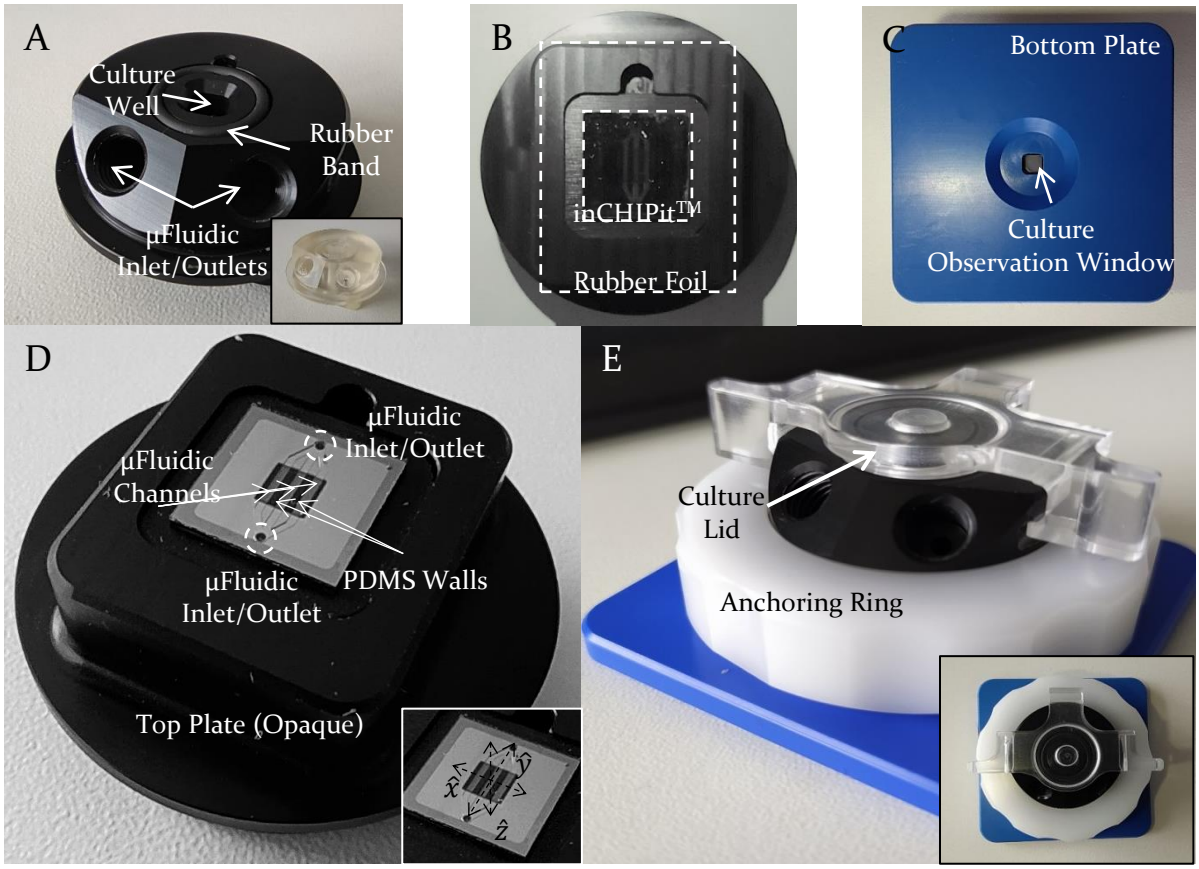

Figure 3.3 A. Front face of the opaque top plate, showing flow ports, the culture well, and sealing rubber band. **Inset**: translucent top plate. **B**. Underside of the top plate showing placement of the inCHIPit™ and rubber foil. **C**. Underside of the bottom plate showing observation window. **D**. inCHIPit™ loaded into the top plate with identifying labels of key features of the system. **Inset**: axis system when imaging the inCHIPit™. **E**. Fully assembled BI/OND OOC device. The top plate is secured to the bottom plate *via* an anchoring ring and the culture well is isolated with an optically clear lid. **Inset**: Top view of assembled BI/OND OOC device.

in the correct orientation in the top plate is shown in Figure 3.3D. To ensure a tight fit and a completely isolated culture environment, the top plate, microfluidic chip, and bottom plate are secured by screwing the top plate and bottom plate together and the culture well is closed off with a culture lid, respectively (Figure 3.3E). This assembly is also easily scaled up for parallel experiments and microscopic imaging using the comPLATE™ (Appendix C-1), although this current work only utilized single assemblies.

During OCT measurements, the BI/OND hardware was oriented in one of two ways: "right-side up" where the culture well and top of the porous membrane were directly exposed to the incident light waves, or "upside down" where the entire BI/OND device was inverted so that the bottom of the microfluidic device was directly imaged through the observation window. This was achieved by placing the BI/OND platform in a Thorlabs Mirror Holder (Part. No. KS2), which when the microfluidics are correctly oriented, permit for single axis manipulations in the xy-plane (Figure 3.3D, inset). This permitted for precise setting of the angle of inclination, which is essential for achieving accurate Doppler measurements. Levelness was checked during imaging using functions included in the Thorlabs software, but later more rigorous calculations are made during the image processing steps as adjustments are made for the differing refractive indices.

3.2 Optical Coherence Tomography Setup

All imaging experiments were carried out in the Department of Imaging Physics within the Faculty of Applied Science, TU Delft, in the Kalkman Laboratory. The setup process is summarized in full in Figure 3.4. The two separate liquid handling and OCT systems are highlighted in blue and red, respectively. The liquid handling system is composed of a pressure source, liquid reservoir, and a flow sensor. The OCT system is composed of a light source, the scanning system, a charge coupled detector, and a computer system. The microfluidic system is identified by purple highlighting. Each block process is connected by an arrow indicating a physical connecting element. Thick arrows are specific to the liquid handling system representing pressure and fluid flows while thin arrows are connected with the OCT system representing light waves and electrical signalling. Each major unit is summarized in the following sections.

3.2.1 OCT Base Unit

The OCT system used in this thesis work is the Ganymede Series GAN220 from Thorlabs. This base unit is a system that images at a center wavelength of 900 nm, through the use of two matched pair superluminescent diodes (SLD). As an imaging unit, these light spectrum values are equivalent to 3.0 μm axial resolution and 1.9 mm imaging depth. The scanning rate was set to 36 kHz. Furthermore, the integrated linear charge coupled detectors (CCD) provide for array-based spectral detection, with each A-scan consisting of 1024 pixels c. The full specifications are tabulated in Appendix C-2.

3.2.2 OCT Scanning System

While the Base Unit provides the light source and detection capabilities, the OCTP-900 Scanning System (Thorlabs) provides the interferometer (i.e. beam splitter), an adjustable reference arm, a sample arm, and an integrated camera for real time imaging and video capture. The reference arm is adjustable through two metrics: the path length and reference intensity. This design feature is included in effort to compensate while imaging in different mediums or with samples of diverse reflectivity values.

3.2.3 BI/OND Device Orientation

In order to control the angle of the BI/OND device in a fine manner, a Thorlabs Mirror Holder (Part No. KS2) was used due to this ability to adjust angles to a high degree. Using the live view feature of the Thorlabs software, it is possible to orient the microfluidics along the two adjustment axes, designated the x-axis and y-axis in this work (Figure 3.3D). The benefit of this system is that it is also compatible

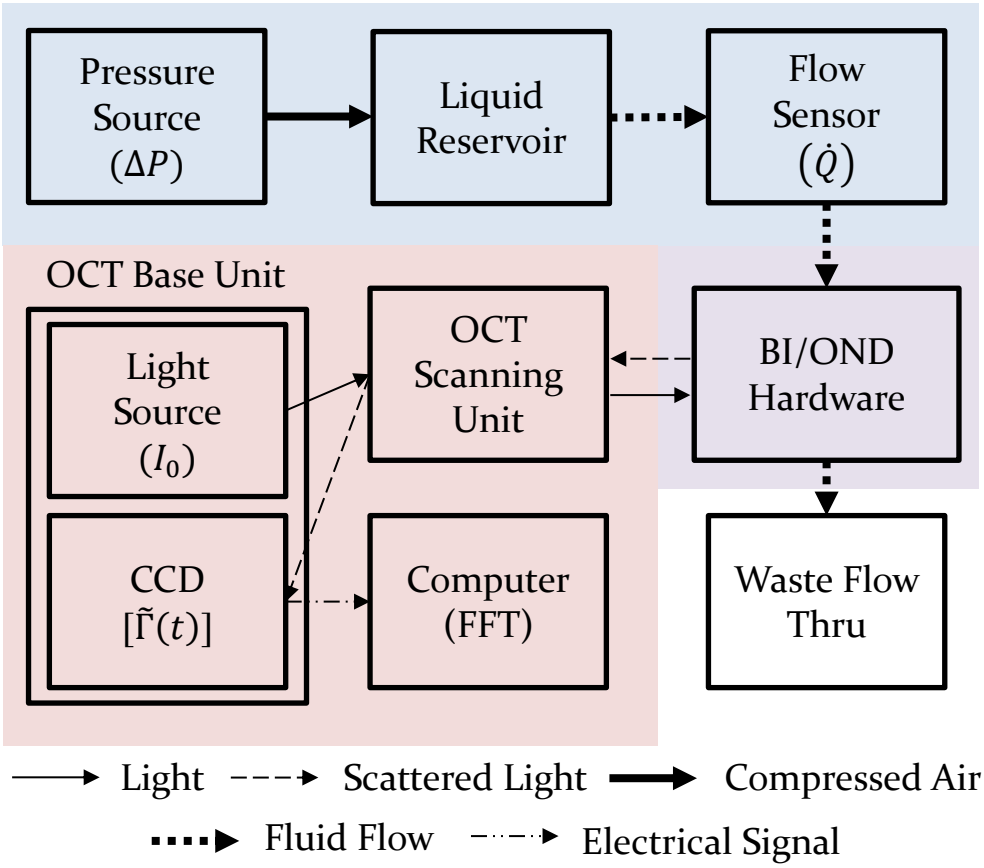

Figure 3.4 Block diagram exemplifying the experimental process. Red block represents the OCT system, the blue block represents liquid handling, and the purple block is the point of overlap, the BI/OND hardware. CCD: Charge Coupled Detector; FFT: Fast Fourier Transform; SLD: Superluminescent Diode; $\tilde{\Gamma}(t)$: Time-dependent Complex Signal Data; ΔP: Pressure Drop; $\dot{Q}$: Volumetric Flow Rate.

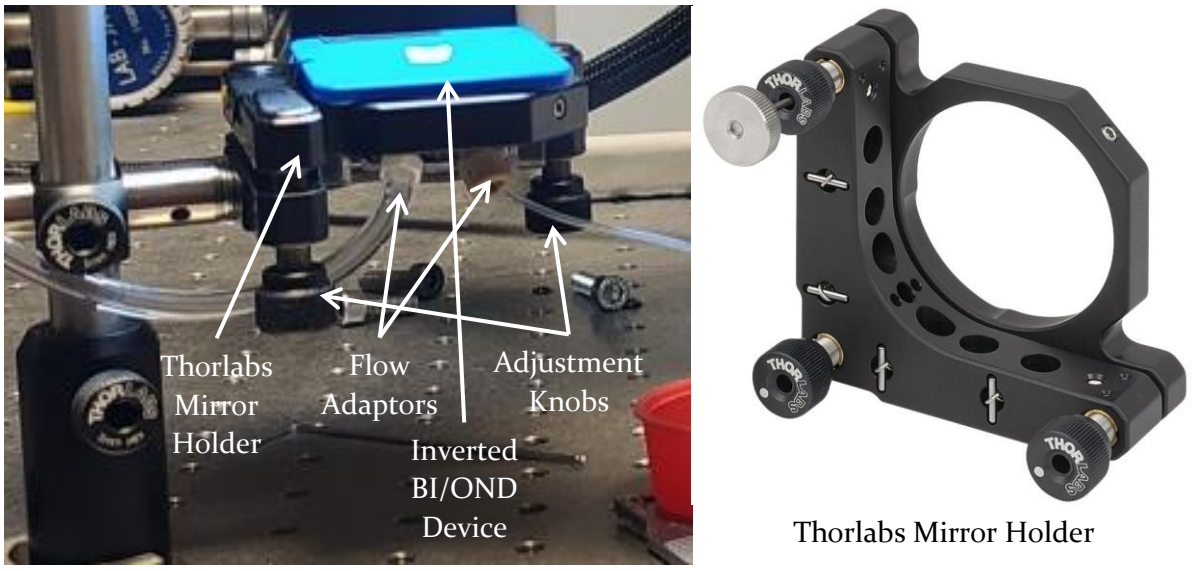

Figure 3.5 Images of the BI/OND device in an inverted position during flow experiments. **Right**: fluid flows entered and exited through the flow adaptors. The angles of inclination of the x-axis and y-axis were adjusted separately by use of the adjustment knows of the Thorlabs Mirror Holder. **Left**: expanded image of the Thorlabs Mirror Holder.

with the required microfluidic fittings of the BI/OND device. An image of the inverted BI/OND device and the Thorlabs Mirror Holder is shown in Figure 3.5.

3.2.4 Thorlabs Software

Thorlabs OCT software streamline the process of capturing and saving images during experimentation. A more expanded protocol may be found in Appendix C-3**.** Briefly, the intensity and raw spectral data needs to be calibrated before each round of experiments. This is achieved by performing the following steps: first, intensity is adjusted by tuning the aperture through which light is passed to and from the Scanning System. Too bright of a visual field results in high background noise while too low of a visual field makes identification of significant features difficult. Intensity readings were set to approximately 70% maximum signal strength, with an acceptable range of 60% to 80%. The raw spectral data is adjusted through manipulation of the reference arm, which involves manually adjusting the optical path length.

3.3 Microfluidic Liquid Handling

3.3.1 Microfluidic Pressure Pump

The pressure source used for this project is the Fluigent Microfluidic Flow Control System (MFCS™)-EX. A-i-O® 2018 software was used. This compact, integrated microfluidic pressure controller permits for both push and pull pressure drops, which allow for the introduction of constant fluid flows through the BI/OND microfluidic device. Although capable of up to 8 differential flows simultaneously, this study required only the use of one pressure drop. The maximum applied pressure is approximately 50 mbar. A short protocol is shown in Appendix C-4.

This pressure is applied to a liquid reservoir that contains either deionized water (DI H_2O) or an oil-in-water nanoemulsion Intralipid® 20%, with a reported droplet size of approximately 500 μm. The dispersed phase (i.e. oil droplets) is 20% (v/v) of the solution and is composed of soybean oil stabilized by 1.2% (v/v) egg yolk phospholipids and a 2.25% (v/v) glycerin-water continuous phase (i.e. non-droplet volume). These nanoemulsion droplets were introduced to microfluidic flows to assist in making Doppler measurements as flowing water itself is insufficient to provide such data.

3.3.2 Microfluidic Flow Sensor

Volumetric flow rates are measured using a Fluigent Flow Rate Platform (FRP), which makes use of transport phenomena qualities – variations in liquid temperature – to measure flow rates with a reported accuracy between 7 nL/min to 5 mL/min. The maximum measured flow rate used in this work is ca. 218 μm/min and the minimum 90 μm/min; there was no difference observed between volumetric flow rate readouts of water and Intralipid®. At low flow rates, baseline readings exhibited some non-zero flow rates as a result of hydrostatic pressure differences inherent to the experimental setup. For example, microfluidic tubing that passed above the FRP or the fact that the BI/OND microfluidic platform was not constantly even with the water level resulted in low positive or negative flow rates. This noise in the flow readings were minimized as best as possible by attempting to keep all fluid containing components at approximately the same relative height.

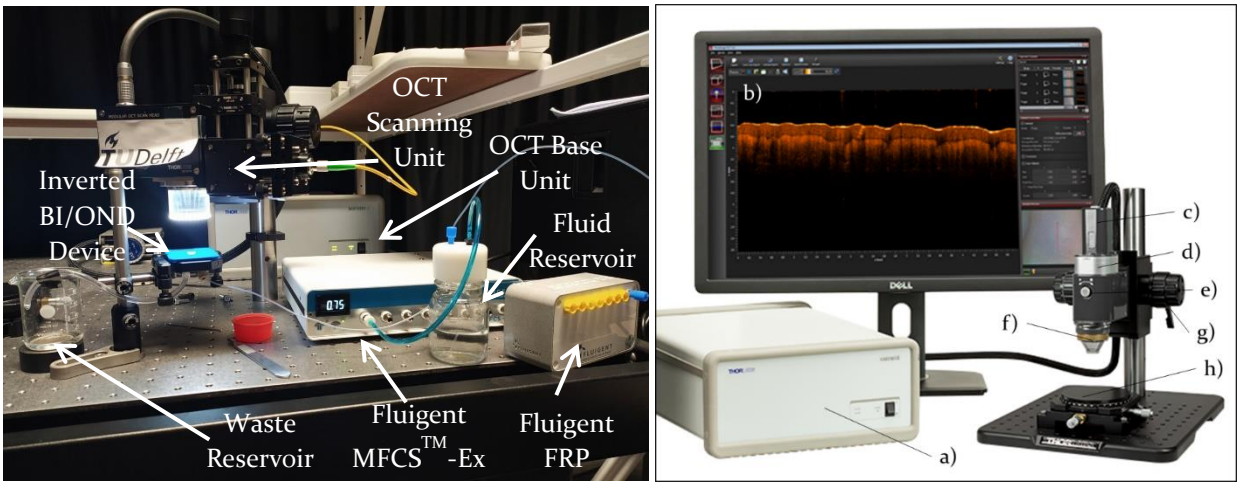

Figure 3.6 Left: Photo of experimental layout, with key pieces of equipment identified. **Right**: Ganymede OCT system: a) Base Unit; b) Thorlabs software; c) reference arm; d) aperture adjustment knob; e) OCT scanning system; f) objective lens; g) focus adjustment; h) translation stage. Left figure adapted from Ref. [70].

3.4 Experimental Setup

The minimal requirements for this thesis work include only the BI/OND hardware and the OCT equipment for making physical characterizations of the microfluidics. By adding the liquid handling aspects in tandem with a scatter medium (e.g. Intralipid®), the capacity for D-OCT is included. A full view of the experimental setup is shown in Figure 3.6. Also shown in Figure 3.6 is a clarifying image of some of the smaller, additional components of the OCT system. While the Base Unit and Scanning System are mentioned above, specific adjustments are made during experiments using integrated parts of the system, for example, the aperture and focusing knobs allow the user to move the sample into the scanning range of the OCT system. All data acquired during OCT measurements were processed using MATLAB® 2018b. The in-house code is shown in Appendix C-5.

Chapter 4

OCT Measurements

The goal of this chapter is to overview and discuss the key results from this thesis work. The results can be delineated into four major points: material effects on OCT imaging compatibility, Doppler measurements of OOC microfluidics, characterization of diffusion phenomenon, and measuring impacts of organoid-like bodies (OLBs) on culture well fluid flows. Due to the structure of the BI/OND device, and as with many OOC platform constructions, there are some associated difficulties to overcome when implementing an imaging technique such as OCT. Here, various approaches were investigated and tested to improve imaging capacity in regards to OOC devices. Afterwards, fluid velocities were measured in the microchannel of the inCHIPit™, officially bringing OCT into the OOC field. The multi-layer structure of the BI/OND device permitted for the observation of secondary flows in the culture well, which will be critical for future *in vitro* experiments involving cells and tissues. Initial observations of more complex flows in the presence of large tissue structures represent the conclusion of this thesis work.

4.1 Material Effects

Optical measurements techniques are often selected due to their alluring traits, such as ease of implementation and relatively non-invasive; furthermore, the speed of signal acquisition permits for real-time imaging, such as in OCT [78]. However, despite these positive traits, such measurements methods are susceptible to background noise as a result of detection methods, signal processing means, and sample material. In the OOC context in particular, as 3D culture device become more complex and contain layered materials, with varying optical properties, such as refractive indices, reflectivity's, and transmissivity's [79], adapting optical measurement methods require more adjustments. In the following subsections, different effects of the inCHIPit™ materials are interrogated; internal reflections, top plate material, and culture lid impacts are discussed.

4.1.1 Device Dependent Internal Reflections

Secondary, faux reflection events were observed during initial OCT measurements of the BI/OND inCHIPit-3C™ device. These erroneous signals become more apparent if the sample was not placed correctly at the focal point of the objective lens of the Scanning Unit. It was also noted that these signals became more dramatic if the microfluidics were empty (i.e. a lack of fluid presence with only air present in microchannels). Examples of these extra reflections are shown in Figure 4.1. These measurements were performed with the inCHIPit-3C™ device inverted (refer to Figure 3.4) such that the bottom of the microfluidic channel was closest to the impingent beam and the culture well furthest.

In Figure 4.1A, a transverse cross-sectional image is shown. Adjacent to the live view image, examples of total internal reflections are shown. At interfaces between different mediums, light waves may either be reflected or transmitted, depending on the angle of incidence and the refractive indices of the materials. The larger the differences in refractive index values, the greater the resulting phase shift in the reflecting wave. For reference, the refractive indices of air, water, and PDMS are 1.0003, 1.33, and 1.43, respectively [80]–[83]. A clear example of this is the step between the porous membrane at the adjacent PDMS layer (Figure 4.1B). The data is processed using a single refractive index value (n_{Air}); adjustments are made in MATLAB® post processing when checking dimensions (data not shown). Such events are potentially compounded because of the inCHIPit™ construction, in which initially reflected waves from deeper interfaces reflected again away from the original impingent light source. In comparing Figure 4.1B and 4.1C, it is clear that not only primary reflections are present, but also secondary and higher order phase shifts are observed. There are measured signals at locations unexpected given the geometry of the inCHIPit™ platform (Figure 4.1C).

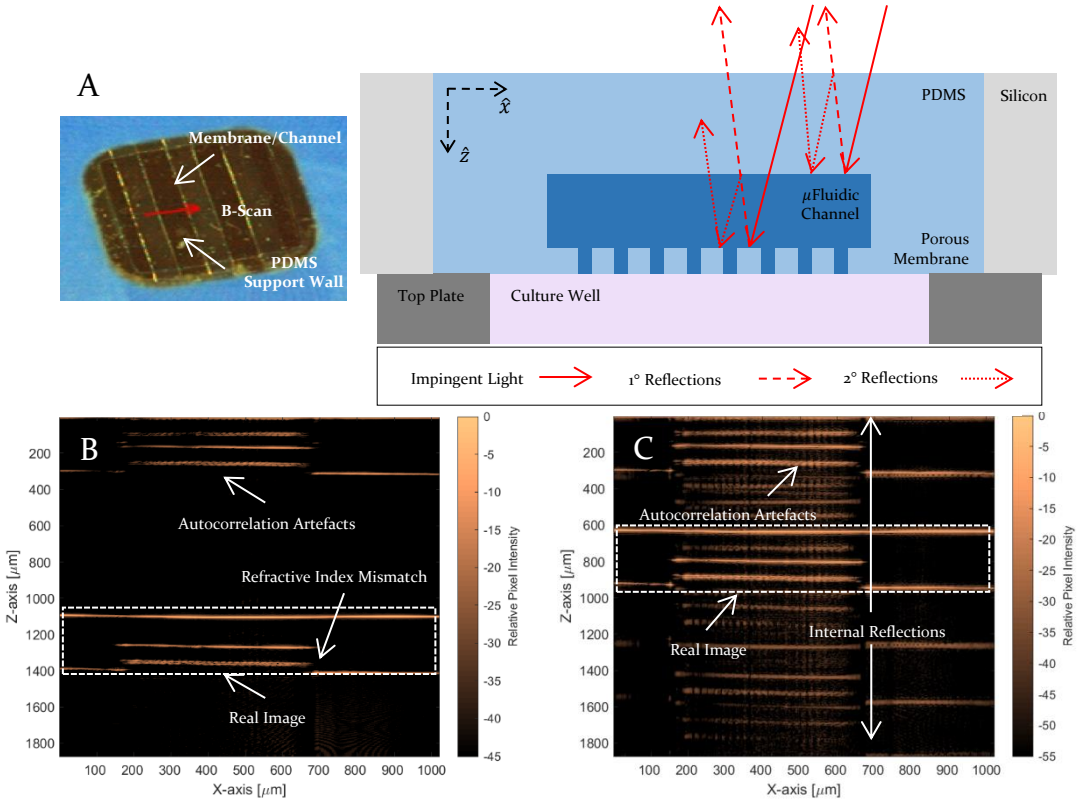

Figure 4.1 Multiple internal scattering events and autocorrelation artefacts within inCHIPit™ microfluidics. **A**. Video image of selected section of inCHIPit-3C™ for B-scan (red arrow) (right), and schematic of scattering paths for impingent light, resulting in first order, second order, and higher order non-primary reflections (left). Refractive index mismatch also shown with arrow **B**. B-scan reconstruction without superfluous noise and strong signal. **C**. B-scan reconstruction with multiple extra reflection events and strong autocorrelation artefact signal. Dashed boxes indicate the location of the real image. Distances are unscaled optical path lengths [μm].

These issues are possibly unique to OCT imaging because of its greater depth of imaging. If compared to higher resolution imaging techniques also largely used in cell culturing, like fluorescent

confocal microscopy, these higher order reflection and transmission signal are outside the focal plane and as well do not appear in the observation plane as strongly due to the higher frequency waves implemented. Confocal microscopy also has the added benefit of pinholes, which physically filter out extra scattered light to isolate the returning sample beam for higher SNR [84].

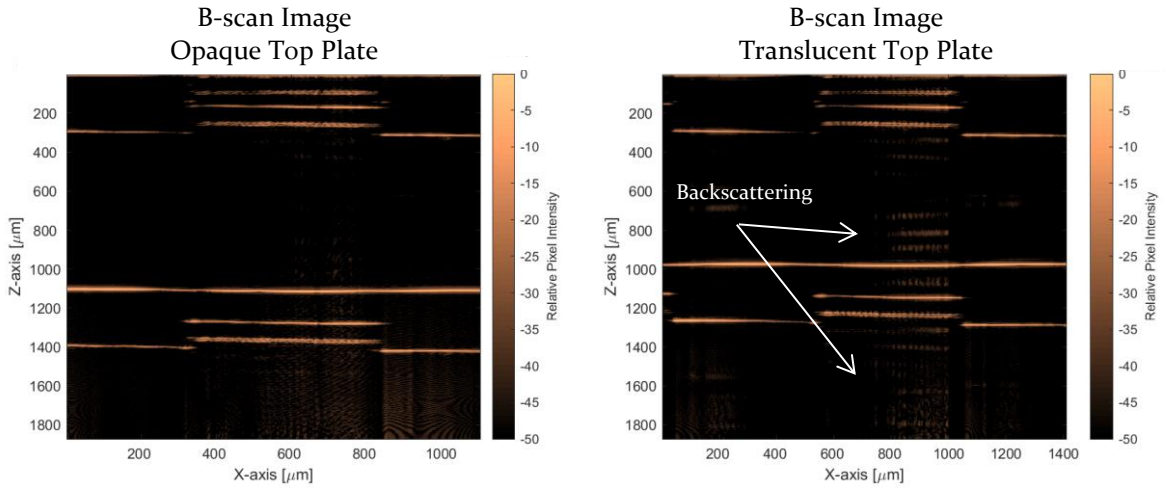

Figure 4.2 Transverse cross-sectional B-scans comparing the amount of background scattering when using the opaque top plate or the translucent top plate. inCHIPit-3C™ device was inverted in relation to the impingent sampling wave. Distances are unscaled optical path lengths [μm].

4.1.2 Top Plate Material Effects

While it is possible to construct OOC platforms out of other polymer-type materials, such as ECM hydrogels [85] or glass-based microfluidics [86], most are still usually entirely PDMS-based. This is originally a result of PDMS' affordability and capacity as a rapid prototyping material with good optical transparency [87]. However, as OOC devices become more complicated in an attempt to recapitulate their respective organ behaviors, microfluidic designs are becoming more complex, and more materials are being utilized. Here, there are a silicon support and plastic top plates. In Figure 4.2, two top plates of different qualities are compared: a dark "opaque" top plate and a light "translucent" top plate (Figure 3.3A). As before, imaging was performed with an inverted inCHIPit™ device to negate extra path lengths and transmission layers; both transverse and longitudinal B-scans were captured.

It is evident that the opaque top plate gave clearer images, seen from the presence of additional, irrelevant signals in the B-scan with the translucent top plate. This observation is further supported in the longitudinal B-scans making the same comparison (Figure 4.3).

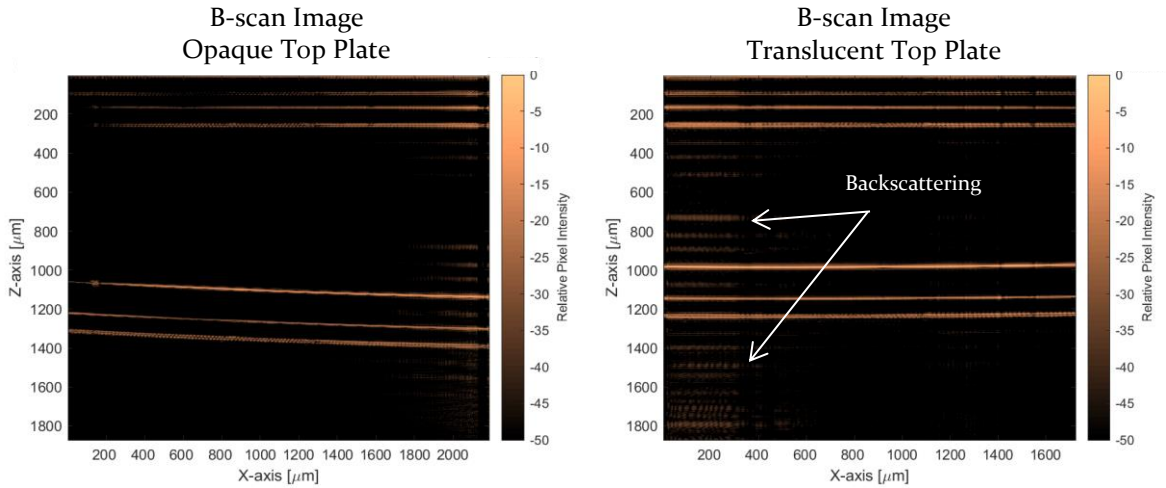

Figure 4.3 Longitudinal B-scans comparing the amount of background scattering when using the opaque top plate or the translucent top plate. inCHIPit-3C™ device was inverted in relation to the impingent sampling wave. Distances are unscaled optical path lengths [μm].

It is not quite clear for the improved image quality, as one would expect a translucent material to permit deeper penetration by light waves, resulting in weaker backscattering, while using the opaque top plate would result in the inverse observation. This would suggest something in regards to the absorptivity of the two top plates. Furthermore, it is curious the top plates play a role in backscattering as geometrically, they do not directly interact with the impinging light waves. The culture well is an empty space reserved for cell culture, and while the microfluidic chip is placed flush with the base of the top plate, the observed microfluidic components are not in direct contact with the top plate. As seen in Figure 4.1A and Figure 3.2, the top plate walls are flanking the regions of interest (e.g. the microchannel, porous membrane, and culture well). These observations may be indicative of some additional mechanisms acting within the BI/OND device. Work performed by Moon and co. at the University of California suggests that such horizontal static noise patterns could be the result of reflections at the end of the sample arm (i.e. the inCHIPit™ device) [88]. Typically, such artefacts are removed during detection at the CCD, but in the case of a highly reflective system such as an OOC platform, this might not be fully achievable.

In a further attempt to improve the quality of the image, and in preparation for D-OCT measurements, adjusting the angle of inclination of the OOC device was explored. By selectively manipulating the adjustment screws of the Thorlabs Mirror Mount securing the inCHIPit™ device, the device would be angled in both the x-axis and y-axis independently (Appendix D-1). In post processing of the B-scan data, angles of inclination could be extracted. In Figure 4.4, the effect is demonstrated. By shifting the angle, the autocorrelation artefact is almost completely eliminated. This is, however, at the sacrifice of the intensity of the sample signal. An optimal range of angles was determined to be between 2° and 3.5°.

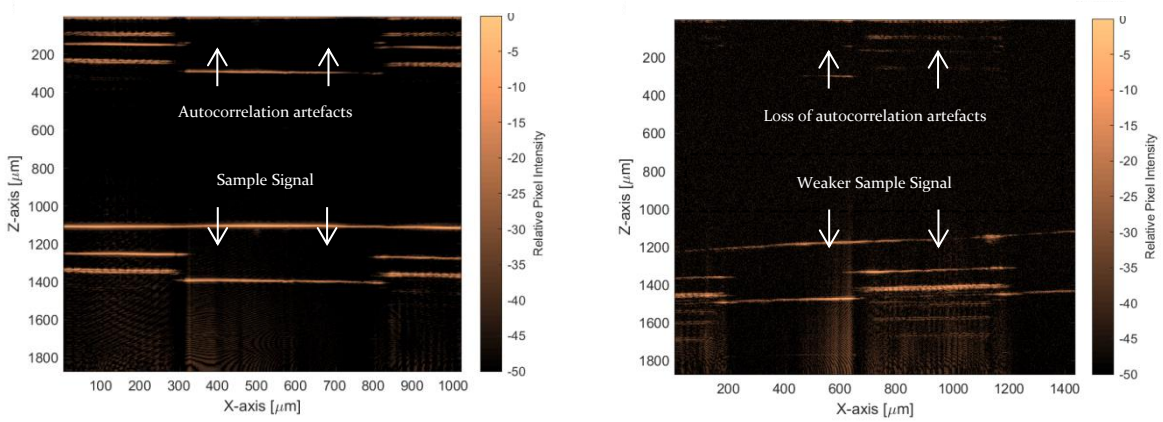

Figure 4.4 Demonstration of the impact of angle of inclination during B-scan imaging of perpendicular cross-section of inCHIPit-3c™ device. **Left**: angle of inclination is 0°. **Right**: angle of inclination is approximately 3.2°. inCHIPit-3C™ device was inverted in relation to the impingent sampling wave. Distances are unscaled optical path lengths [μm].

4.1.3 Effect of Culture Lid

When performing any form of cell or tissue culture, it is absolutely requisite that the culture environment be as sterile as possible. Typically, cell cultures are performed within a class of biological cabinets or fume hoods as a primary precaution; however, other easy to take measures are in place, such as culturing the cells in sterile, covered containers. Here, the BI/OND platform makes use of a semi-transparent lid along with a rubberized ring gasket to completely isolate the culture well during use (Figure 3.2, 3.3E). But, its impact on OCT measurements needed to be assessed, as this adds another layer of scattering, possibly limiting the ability to accurately identify structures within biological samples or assess fluid flows *in vitro*.

The baseline case of OCT measurement for comparison was taken while the OCT device is inverted with respect to the Scanning Unit, as shown in Figure 4.1A. As before, this path is chosen because it is the shortest, most direct path to the microfluidic channel of the inCHIPit™ device. Therefore, it should

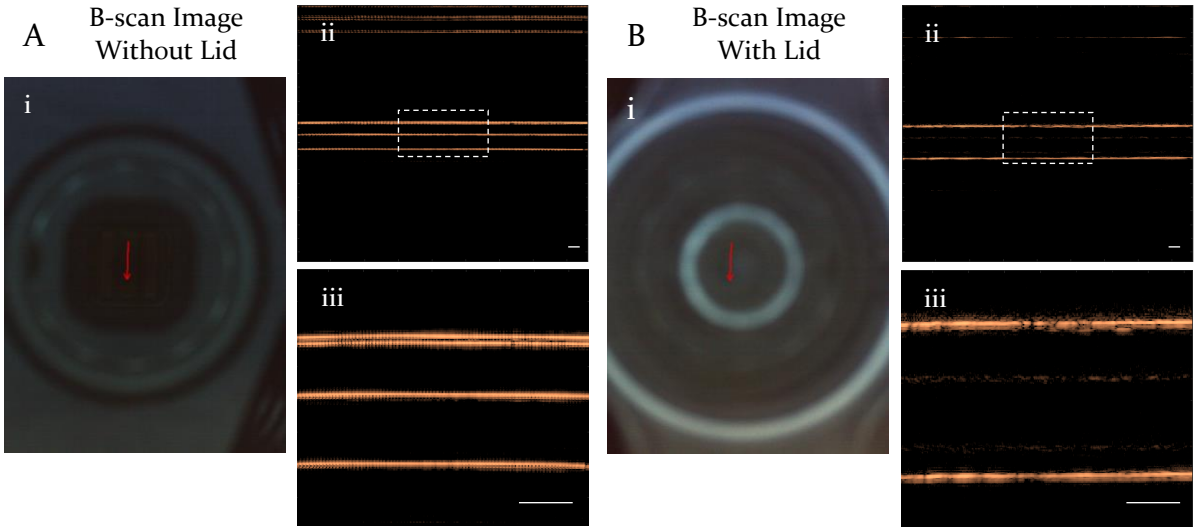

Figure 4.5 B-scans comparing impact of the culture lid on imaging quality. **A**. Images without a lid covering the culture well. **B**. Images with a lid covering the culture well. **i**. Live images of B-scan selections. **ii**. B-scan images of longitudinal cross-section of inCHIPit™. **iii**. Zoom sections of B-scans. Scale bars are 100 μm optical path length. inCHIPit-3C™ device was right-side up in relation to the impingent sampling wave.

also have the fewest superfluous scattering opportunities and should give the strongest signal when returning to the OCT Base Unit for detection. The subsequent two cases are measured with the BI/OND device oriented right-side up, with the porous membrane being closest to the sampling light wave. The first of these two cases are without the culture lid; the second is with the culture lid in place.

In Figure 4.5, it is first evident that the presence of the lid has a negative effect in terms of choosing the location to image. By comparing Figure 4.5A.i and 4.5B.i, it is apparent that the lid filters out most of the backscattered light waves, suggesting that the material used it not maximally optically transparent. However, this is an observation made effectively with the naked eye, which may not be fully paralleled to imaging under more sensitive methods. Through the B-scan reconstructions of the porous membrane and microfluidic channel, the effect of the lid is further elucidated. Comparing the images between Figures 4.5A.ii,iii and 4.5B.ii,iii, the negative impact of the presence of the lid on OCT measurements is further enforced. The resolution of the multiple layers of the inCHIPit™ is clearer without the lid where all layers are distinguishable. In comparison with the base case of a B-scan with an inverted BI/OND device, there is no significant different quality of image.

While the imaging quality is similar between a right-side up no lid case and the inverted instance, when put in the context of macro tissue culture, the inverted scenario may prove to be problematic if the tissue does not strongly adhere to the porous membrane surface. It would make imaging with the current OCT setup sub-optimal as the tissue would be mobile and would move when the culture would be inverted. This may be ameliorated by repositioning the OCT Scanning Unit underneath the OOC to image in an upwards manner, permitting the tissue to fully settle down on the top surface of the porous membrane. In this case, though, there is a drawback that imaging within the culture well will be significantly limited as light will not penetrate past the tissue, effectively limiting FOV to the bottom surface of the macroscopic tissue and microfluidic channel.

4.2 Doppler OCT of inCHIPit™ Device

Doppler OCT was performed to characterize fluid flows in the BI/OND OOC device. These data are extracted through calculating the Doppler phase shift as explained in Chapter 2. Spectral averaging was set to 5, lateral averaging was set to 5, and axial averaging was set to 4. Four or ten snapshot images were captured during D-OCT imaging, which were used to calculate the Doppler phase shift; imaging time was approximately 0.15 or 1.5 seconds. In order to generate backscattering within the microfluidic channel and the cell culture well, Intralipid® was introduced through the microfluidic inlet. This oil-in-water emulsion provided quasi-point particles for the imaging beam to backscatter and gather information about the flow characteristics. When measurements were focused within the culture well,

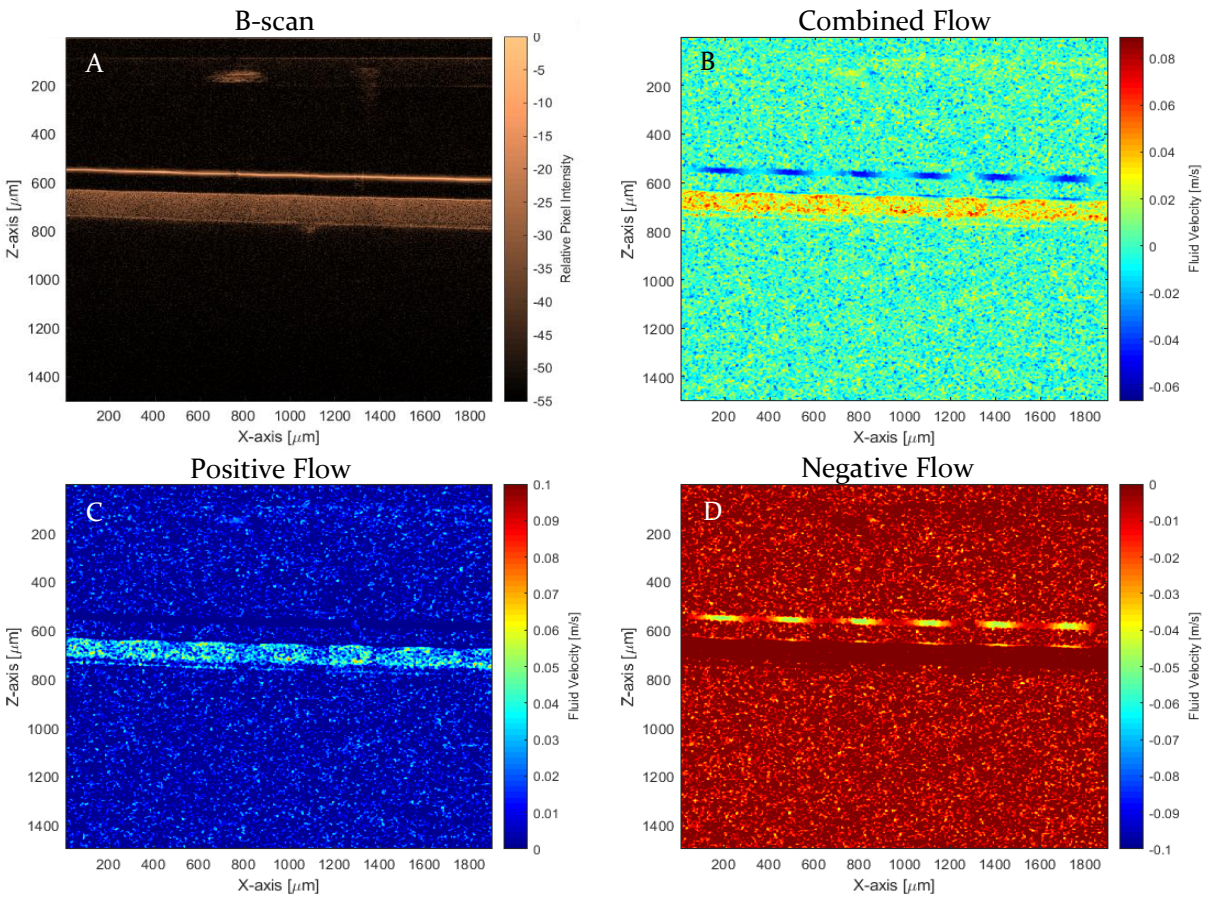

Figure 4.6 Example of Doppler flow deconstruction. **A**. Longitudinal B-scan as a positional reference. **B**. Full reconstruction of Doppler flows. **C**. Positive Doppler flows. **D**. Negative Doppler flows. inCHIPit-3C™ device was inverted in relation to the impingent sampling wave. FRP flow rate: 218 μL/min.

the volume was flushed with DI H_2O to avoid excess scattering from remnant emulsions. All aspects of the process were identical to that of acquiring an A-scan or B-scan in terms of location selection and machine calibration. According to the Thorlabs OCT manual, the machine has a maximum detectable fluid velocity, which follows the relation $v_{\max} = f \cdot \lambda/4$, where f is the scanning rate of the OCT machine (36 kHz) and λ is the vacuum center wavelength of the light source (900 nm) [89]. In all appropriate instances, flows were kept within this v_{max} limit; however, during attempts to measure diffusion and transport across the porous membrane, this limit was exceeded.

B-scan images and Doppler can be acquired simultaneously (Figure 4.6A-D). Images depicting Doppler adjusted flow profiles are scaled and colorized, as shown in Figure 4.6B. By selecting the positive (Figure 4.6C) or negative (Figure 4.6D) components of the Doppler shifts, it is possible to determine the relative direction of flow. This is able to be performed because the general direction flow is known *a priori*, determined by the pressure driven flows and the plane of the microfluidic channel. If, for instance, these measurements were made in the context of a highly vascularized tissue sample, blood flow direction would not be as easily elucidated and only magnitudes could be reliably measured [90]. By converting the appropriate velocity range based on the color of the Doppler images, and converting to flow rates, the D-OCT measurement may be compared to the readings on the Fluigent FRP. Here, two measurements are performed: a longitudinal B-scan and a transverse B-scan. For the longitudinal case, the input flow rate is recorded as 218 μL/min, which is approximately 72.7 μL/min per channel, whereas the observed velocity range is 54 to 90 μL/min (0.03 m/s to 0.05 m/s). The expected flow rate agrees with the observed values using D-OCT. This is despite the observed fluid velocity being above the $v_{\max}$ value; as the B-scans are selected by hand, it is possible that the vertical slice is not precisely in the middle of the channel, which would lead to a measured profile closer to the wall and, therefore, a B-scan in a region where the flow is slowed due to viscous effects near the channel wall. The

range of flow rates can be narrowed by adapting more intensive data processing, specifically to convert the colorized data to a list of numerical values. This will significantly reduce the range of flow rate values.

The second transverse B-scan can reveal a velocity across the center of the microfluidic channel rather than along the longer axis. In Figure 4.7, the input flow rate measured by the FRP is 90 μL/min. The D-OCT measured range of velocities converts to approximately 144 μL/min to 192 μL/min (0.06 m/s to 0.08 m/s), which is a large overestimation. This is in part to v_{max} = 8.100 μm/s, or a corresponding 14.58 μL/min. While it is still evident that the direction of the flow is correct, determining the speed accurately is not possible as it is evident that the phase shift exceeds $\pi/2$ radians [53]. Furthermore, if a transverse B-scan is performed, additional information may be sampled, relative speeds may be compared. Fully developed, laminar flow through straight microchannels exhibits a parabolic velocity profile, with the peak velocities existing at the center of the channel were there are minimal wall effects [91]. By plotting the intensity values from measure across the area of the channel (with a moving average filtering), it may be confirmed that the velocity profile fits such a description for rectangular cross-sections (Figure 4.7). Fitting a second order polynomial to the horizontal and vertical profiles gives r-squared values of 0.3051 and 0.9759, respectively. It is reasonable that the horizonal fit is lower as it is in the larger dimension of the channel, and will have a larger radius of curvature, thus deviating more from the parabolic shape [91]. Therefore, longitudinal B-scan data provides more accurate measures of channel flow rate and transverse B-scans give a relative sense of the flow velocities at points across the interior microfluidic channel.

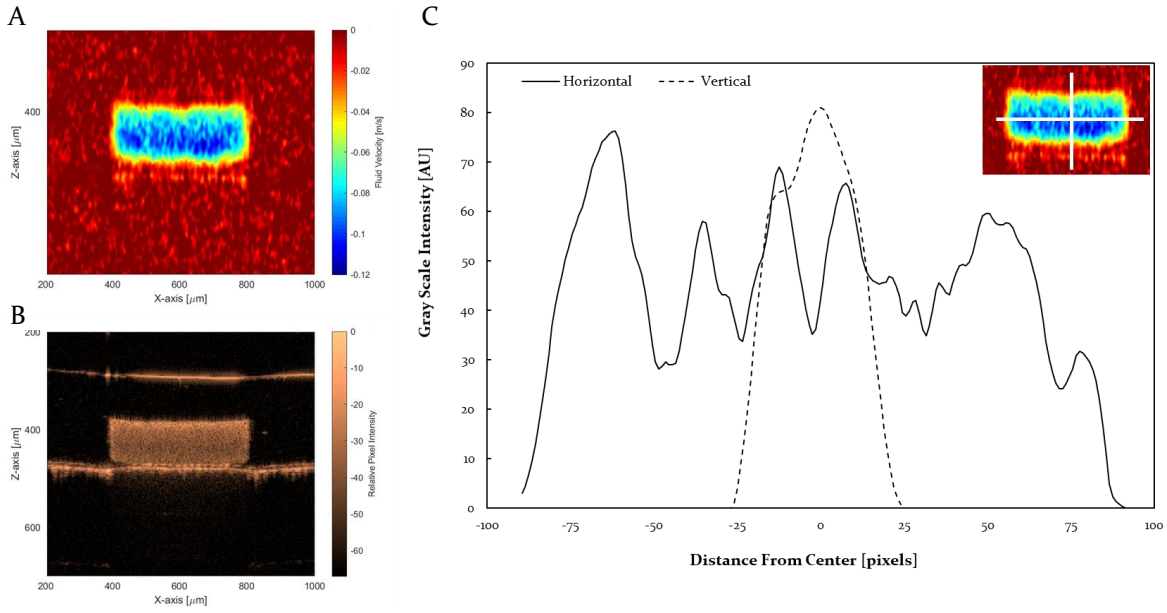

Figure 4.7 Quantitation of fluid flow velocities in inCHIPit-1C™. **A**. Heat map of fluid velocities in inCHIPit-1C™ microfluidic channel. **B**. B-scan of inCHIPit-1C™ microfluidic channel. inCHIPit-1C™ device was inverted in relation to the impingent sampling wave. **C**. Axially resolved gray scale intensity profiles (AU = arbitrary units) taken in the horizontal (solid line) and vertical (dotted line) directions of the inset image.

The microfluidic channel in the inCHIPit™ device is not entirely a closed system as the top layer is a porous PDMS membrane rather than a solid boundary. The purpose is to drive diffusive mass transport and fluid refreshment in the culture well. *Organ-on-Silicon* made allusions to this, though the simulation model was never experimentally confirmed. In work preceding this study of the inCHIPit™ platform, some simulation studies with COMSOL® were carried about by Gaio and co., demonstrating flow enters the culture well closest to the inlet through the porous membrane during flow (30 μL/min), travels along the top side of the membrane, and then re-enters the microfluidic channel at the other side of the well at the outlet (Figure 4.8A,B) [43]. This flow path is divided into three sections: ascending, horizontal, and descending (Figure 4.8C). Here, attempts are made to support that claim. Doppler scans were performed at the entries and exits of the three channels of the inCHIPit™ device with a third slicing diagonally across all three, intersecting one channel at the entry, one at the middle portion, and the last at the exit. Images were taken with the chip inverted. If there are elements of the incoming fluid flow entering the culture channel, it is reasonable to expect a change in fluid velocity within the microfluidic channel, dictated by conservation of mass. The scans are shown in Figure 4.9.

As it can be seen, there are three distinct flow patterns corresponding to the entering flow, cross flow, and exiting flow. The entering flow demonstrates a negative flow, the mid flow has elements of both positive and negative flow, and the exiting flow has a positive flow. These stark differences may possibly be explained by the model proposed in Figure 4.10. D-OCT is able to derive particle velocities based on backscattered light anti-parallel to the impinging light (Figure 4.10B). Through this component vector, the magnitude of the velocity may be derived. However, in the cases of Figure 4.10A,C, there is an extra angle α the either leads to an upward flow into the channel, $\boldsymbol{V}_{asc}$, or back into the microfluidic channel, $\boldsymbol{V}_{des}$. Unfortunately, the exact value of this angle is not known for this work. However, by performing a similar analysis and identifying the component vectors contributing to $\boldsymbol{k}_s$, a sense of the impact on the measured phase shift, and corresponding Doppler velocity, may be gained. The modelling suggests either an underestimation or overestimation of the flows, as $\boldsymbol{k}_{s_{asc}} < \boldsymbol{k}_s < \boldsymbol{k}_{s_{des}}$ giving $\boldsymbol{V}_{asc} < \boldsymbol{V} < \boldsymbol{V}_{des}$. This is made clear by rearranging the expressions for $\boldsymbol{k}_s$ as functions of $\boldsymbol{V}\cos\theta$. These relations were not fully explored during the course of this work due to unforeseen circumstances.

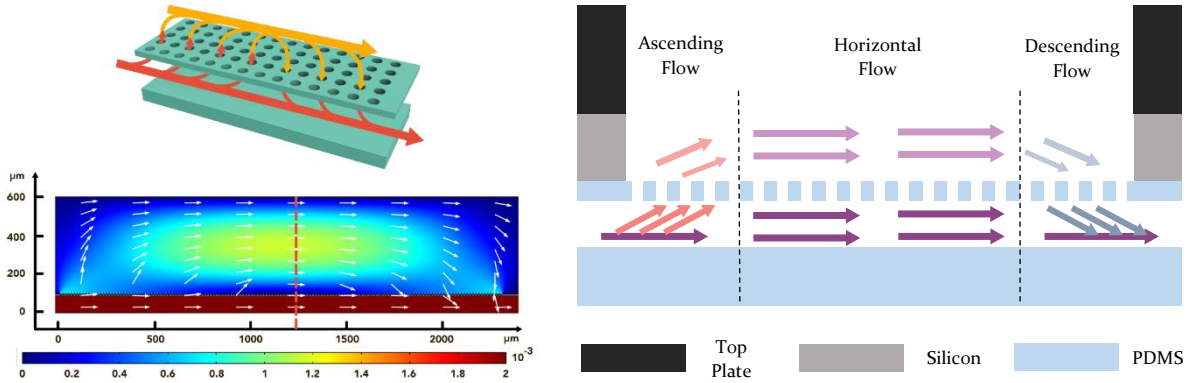

Figure 4.8 Fluid velocity vectors across the porous membrane of the inCHIPit™ platform. **Top Left**: 3D rendering of simulation modeling from Ref. [43]. **Bottom Left**: Simulated flow values from COMSOL® simulation. Heat map and colorbar measuring fluid velocity in m·s^{-1}. **Right**: Cross-sectional diagram depicting three flow regimes in the inCHIPit™ OOC. Red indicates flow ascending into the culture well, purple indicates flow horizontal relative to the microfluidic channel, and blue indicates flow descending from the culture well. Light shading is flow inside the culture well while dark shading is in the microfluidic channel.

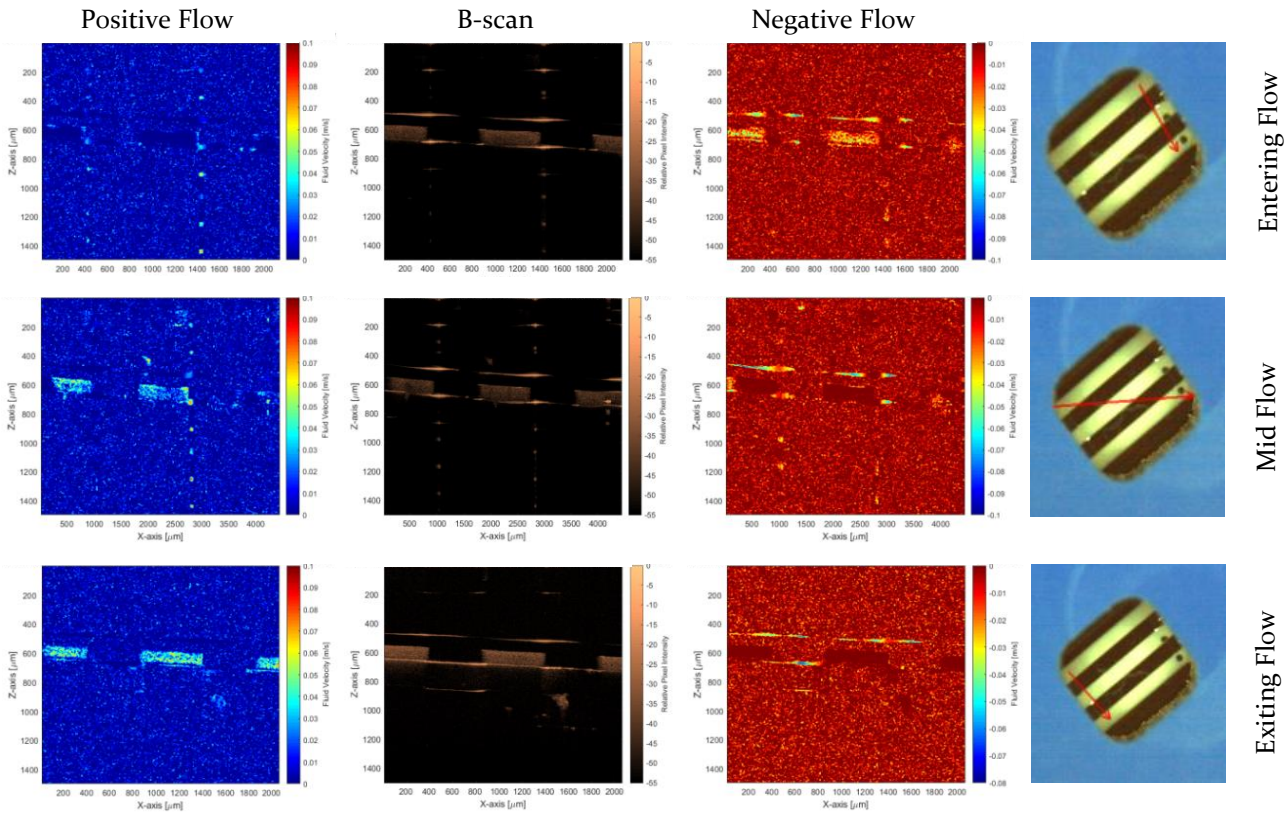

Figure 4.9 Doppler flow measurements across microfluidic channels of inCHIPit-3C™. B-scans were taken at the entrance, mid-section, and exit of the microchannels. All 3 microchannels were simultaneously measured. Live images on the right show where B-scans were taken. Microchannel widths are 300 μm. The calculated angle of inclination is 3.9°.

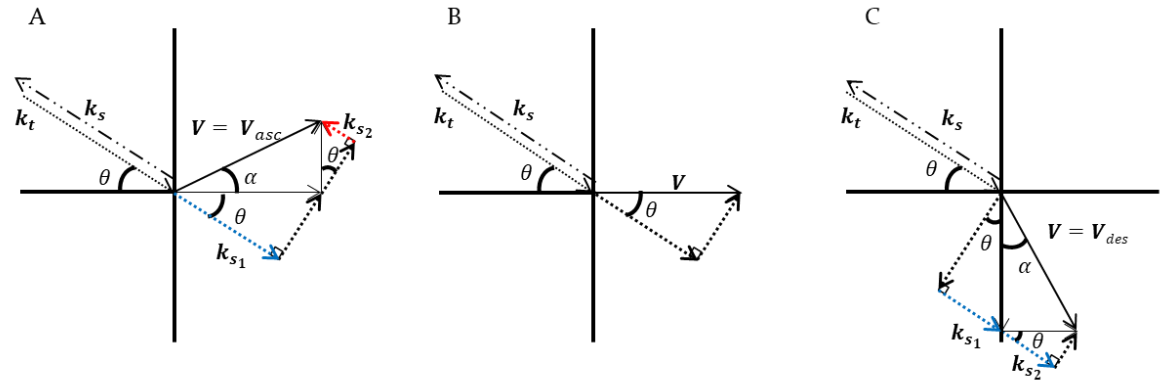

Figure 4.10 Vector diagrams of theory behind Doppler OCT. The horizontal axis represents the longitudinal axis of the microfluidic channel and the vertical axis is the normal. **A**. Case during ascending flow $\boldsymbol{V_{asc}}$ relative to the microfluidic channel. **B**. Case for horizontal fluid flow $\boldsymbol{V}$ coincident with microfluidic channel. **C**. Case during descending flow $\boldsymbol{V_{des}}$ relative to the microfluidic channel. $\boldsymbol{k_t}$ is the incoming light, $\boldsymbol{k_s}$ is the scattered light, $\boldsymbol{k_{s_1}}$ and $\boldsymbol{k_{s_2}}$ are components of $\boldsymbol{k_s}$ during ascending and descending flow, θ is the angle of inclination respective to the horizontal, α is the additional angle dependent on the steepness of ascent or descent of flow. Blue vectors indicate phase shift contributing values while red vectors are detracting.

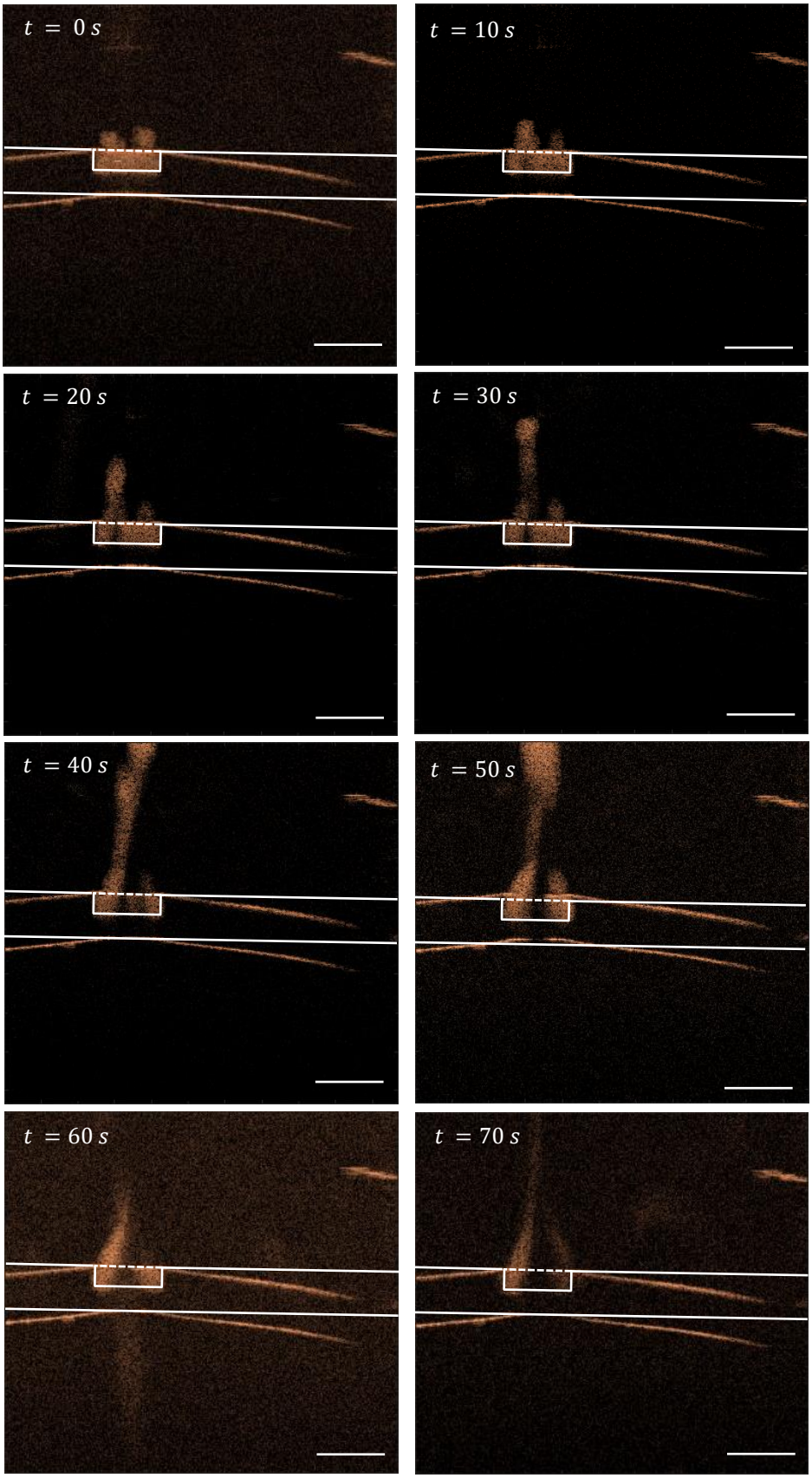

Figure 4.11 Sequential transverse B-scans acquired during diffusion studies. Time interval images were captured every ten seconds. The flow rate was set to approximately 49 μL min^{-1}. Measurements were performed in an upright inCHIPit-1C^{TM}. The scale bar is 300 μm.

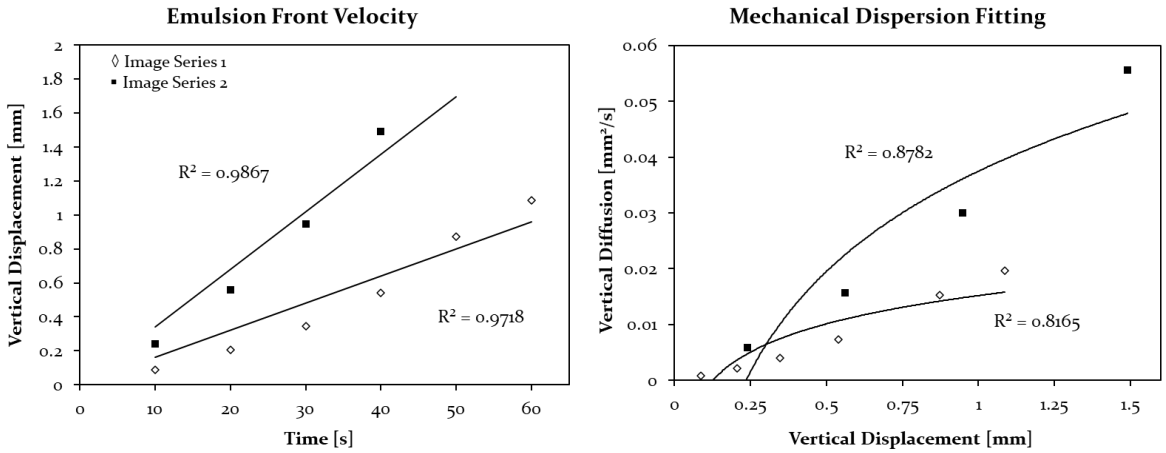

Figure 4.12 Curve fitting of Intralipid® emulsion entering the culture well volume. **Left**. Displacement against time with linear curve fitting. The R-squared values are displayed next to their respective curves. **Right**. Diffusion units against displacement with logarithmic curve fitting. R-squared values are placed next to their respective curves. Image series 1 (unfilled diamonds) corresponds to Figure 4.10. Image series 2 is in Appendix D-2 (dark squares).

4.3 Porous Membrane Transport Characterization

As the goal of the BI/OND inCHIPit™ device is to (co-)culture cells and tissues in the culture well, media refreshment is a requirement of the platform. B-scans were performed of diffusing Intralipid® emulsions as an initial study of such phenomenon. Images were taken in a time series, every 10 seconds and then the distance from the membrane surface was measured at each time point. By relating these measurements to velocity units and diffusion units, curve fitting could be performed to form an understanding of how the culture well volume is connected to the microfluidic channel. It should be noted, that these data are proof-of-concept, as the lid was removed, causing the liquid level to change as measurements were taken, and the diffusive qualities of Intralipid® are not known. There is also some difficulty in measuring the distances traveling by the ascending emulsion front. Once the edge of the front leaves the FOV, it "returns" as a downward flow. This is due to the process of FFT performed on the OCT data.

Figure 4.11 shows a series of B-scans capturing Intralipid® emulsion entering the culture well. By measuring the pixel distance from the membrane surface, converting to optical path distance and then an actual distance, the velocity was estimated to be 16 μm/s by plotting displacements over time [92]. Plotting the diffusive measures (length²/time) against displacement, implications of diffusive behavior may be elucidated [93]. Since the diffusion coefficient of Intralipid® in water is not known, the distinction between dispersion and diffusion cannot be determined; however, the curve fitting confirms the action of one or the other. Free diffusion exhibits radial expansion from a point of origin, while dispersion phenomenon demonstrate elongated patterns due to the extra flow from velocity terms [91], [93]. Due to the shape of the emulsion front, mechanical dispersion through the pores appears to be a more likely candidate. The fitted curves are shown in Figure 4.12.

4.4 Doppler OCT During Organoid Culture

As real organoids were not obtained during the course of this thesis work, organoid-like bodies (OLBs) were formed using commercial model compounds Play-Doh®. While materials more suitable for such a substitution should have been used, such as hydrogels [94], they were not accessible to the author. Modelling clay was first rolled out into a long, thin fiber, and then cut into smaller sections These sections were rolled by hand and then placed in an oven at 100°C for approximately 45 minutes, or until the OLBs were no longer soft to the touch. The average major diameter was ca. 2.27 mm and the average minor diameter was ca. 1.86 mm. Organoid-like bodies were measured using a Mahr 16ER

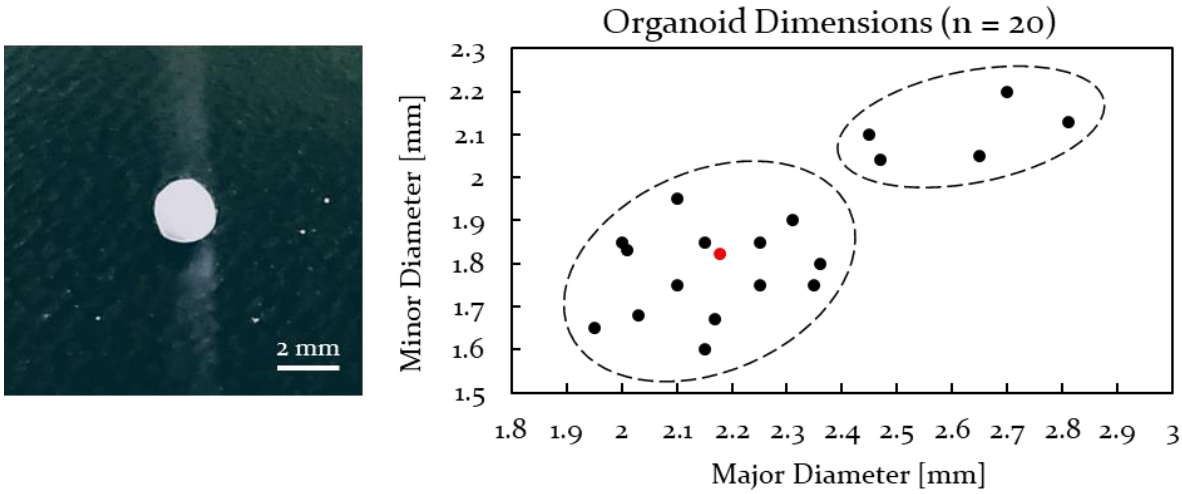

Figure 4.13 Organoid-like bodies (OLBs). **Left**: image of organoid used during D-OCT testing. **Right**: Scatter plot of OLBs (n = 20) plotting major and minor axes. Two clusters are shown; the red data point corresponds to the image on the left. Scale bar is 2 mm.

MarCal Digital Calliper. Size distributions and an exemplary image are shown in Figure 4.13. The organoids were at the same length scale as those used in Gaio *et al.* [43].

As the modelling compound is less dense than water or Intralipid®, the OLBs tended to float within the culture well volume. Further, imaging was performed with inCHIPit™ positioned in an upright manner to attempt to model how normal organoids would behave during culture. This combination made imaging condition more variable. Based on the filling of the well and the size of the OLB, flow was disrupted differently. Two examples are shown in Figure 4.14. It should be noted, that measurement of flow within in the channels is cut off because the impinging light is stopped by emulsion clouds above the FOV.

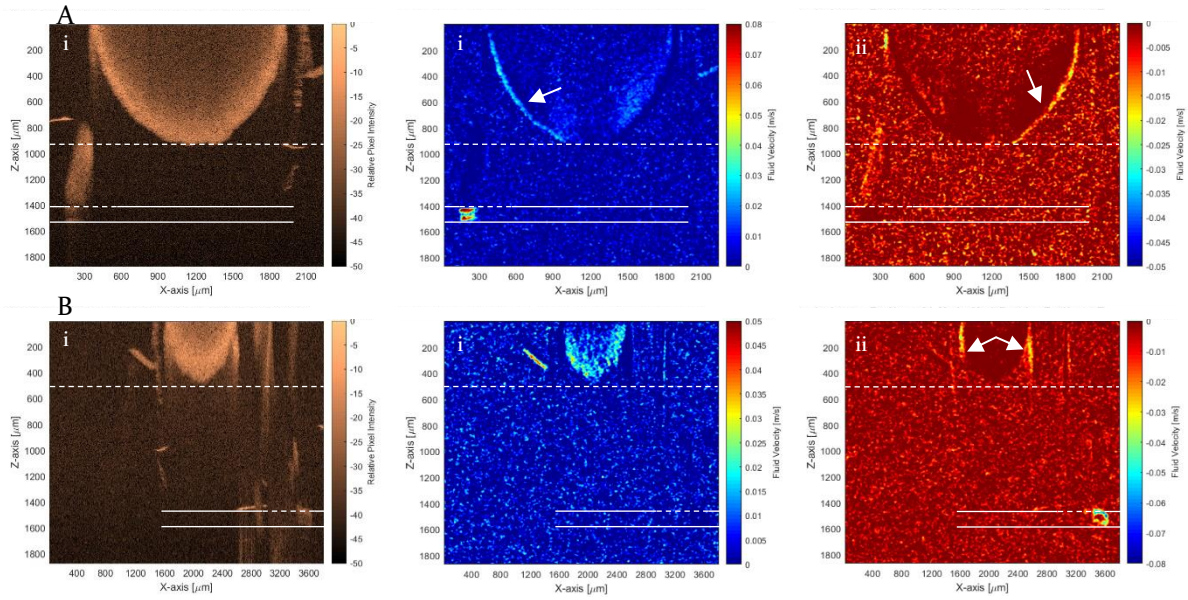

Figure 4.14 B-scan and Doppler images of OLBs suspended in the culture well. **A**. OLB is imaged closer to the well. **B**. OLB is imaged further from the well. **i**. B-scans. **ii**. Positive flows. **iii**. Negative flows. Long, dashed white bars indicate the bottom-most portion of the OLB. The solid white and short dashed white line indicate the PDMS walls and porous membrane locations, respectively. White arrows are point out velocity signals along the OLBs. inCHIPit-1C™ was imaged right-side up with respect to the imaging beam

Chapter 5

Conclusions & Future Directions

Organ on Chip as a field has exploded with many new organ models are being developed, with the hope that a human on chip, a full integration of all organ-specific OOCs into a larger ensemble that recapitulates body-wide responses, will eventually be created. However, many of the current techniques for characterizing and quantifying physical features on these microfluidic chips are lagging in some respects. Often, sample preparation is an involved and tedious process, while other methods can be based on simulations with simplifying assumptions. The goal of this thesis was to demonstrate the versatility and applicability of OCT within in the context of the OOC field. To the author's knowledge, this has yet to be done, or at least, has been performed in very limited fashions. In this thesis report, methods and primary results were presented, demonstrating the usefulness and feasibility of using OCT in future studies involving OOC platforms, such as that of BI/OND. Concluding this thesis work, the objectives from Section 1.3 are reviewed and future prospects are also addressed.

While OCT may not be fully compatible with all OOC systems – for example, microfluidics entirely fabricated of laboratory glass would cause high amounts of extra reflections, it proved informative for revealing useful parameters to be considered when performing OCT with OOC. The effects of OOC construction materials was shown to have noticeable impacts on B-scan quality. When using the inCHIPit™ platform, the two different build materials of the top plate could be seen to affect the amounts of light backscattering, with the opaque one giving better results. The presence of the lid severely limited imaging capabilities when imaging from the topside of the culture well. If this issue is not specifically addressed, imaging while culturing may prove difficult in the BI/OND chip. And as demonstrated, some solutions, such as angling the devices with respect to the scanning beam or selecting specific materials, can be easily implemented.

It was also shown in this thesis work that D-OCT can be successfully used in OOC platforms to characterize flows in both sections of a two-layer device. Velocities were confirmed to be reasonably accurate (longitudinal measures showed flow rates in a range of 54 to 90 μL/min for an expected flow rate of 72.7 μL/min), but OCT appeared to also tend to overestimate flows, with measured flows in the range of 144 μL/min to 192 μL/min when a flow rate of 90 μL/min was expected. These two observations

were performed on longitudinal and transverse cross section, respectively. It would be advised to explore this more. However, flows were shown to follow fluid mechanic models and exhibited fully developed, parabolic velocity profiles. Furthermore, proof of culture well refreshing was reported, with initial attempts to characterize diffusive traits. Emulsion transport across the porous membrane exhibited dispersion like behaviour, although with more intimate knowledge of the effusing solution material properties, this observation could be explored more in detail.

Lastly, it was briefly shown that OLBs disrupt culture well flows in distinct ways, though there is a need for a more thorough investigation. The disruption of flow is loosely correlated to the size of the OLB and the OLB's distance microfluidic channel. OCT, despite unforeseen circumstances and limited access to both biological labs and imaging labs, proved to be applicable in such circumstances and more experiments should be performed as follow up.

5.1 Recommendations and Future Work

The results in this thesis are strongly positive in regards to the potential of OCT becoming a staple measurement tool of the organ on chip field. Its abilities to scan systems without significant sample prep and real-time imaging are alluring while its versatility would make it adaptable to the diverse range and types of OOCs. For example, optical coherence elastography, OCT applied in another manner based on speckling patterns, would be useful for studying mechanical stimulation in OOCs without the need to introduce other materials or labelling compounds. Many OOC systems attempted to introduce physiologically relevant stress and shear input, but must rely on simulations, secondary indicators of those parameters, or implement fairly complicated protocols. OCT can perform such measurements without much adaptation to its basic protocol; many extensions of the technology are accessed through data processing and not the experimental setup. Thus, it is not hard to imagine that OOC dimensions, fluid flow velocities, mechanical properties, and monitoring of biological events all can be captured through this single measurement system.

The characterization of the BI/OND device remained incomplete, in part due to uncontrollable factors by the author. First, a full profile of the media refreshing in the culture well is required. A useful tool that could be used is a flow valve, which would make induction and monitoring of flow more accurate. Next, studying lower flow rates would also give the ability to measure diffusion properties specifically without the added velocity component of mechanical dispersion. It would as well be confirming of OCT's accuracy when measuring fluid flows in that regime in OOC. Alongside these studies, improved analytical and computations can bring about more accurate flow measurements. Additionally, measurement of velocity profiles around macroscopic tissues is needed; one aspect, especially, would be to use actual tissues as the utilized modelling compound was not fully realistic. Concomitantly, scanning the tissues from different angles would be required, as the tissues are highly scattering and imaging both sides of a macrotissue would not be possible. Orienting the Scanning Unit from both the top and bottom could solve this issue partially.

The future of drug development and biomedical testing is promising with the advent and versatility of OOC technologies. Drug responses can be better gauged due to the increased biological similarity of OOC models and scientists can better study the human body. To help drive toward this goal of effective 3D culturing, an equally versatile imaging tool is needed to capture many aspects of OOCs. OCT can track dimensional features, microfluidic fluid flows, and mechanical strains using the same imaging process; thus, OCT best fulfils the needs of the OOC field and merits a much deeper investigation in conjunction with OOC development.

Appendix A

Applications of OCT

A-1 Extended Applications for OCT

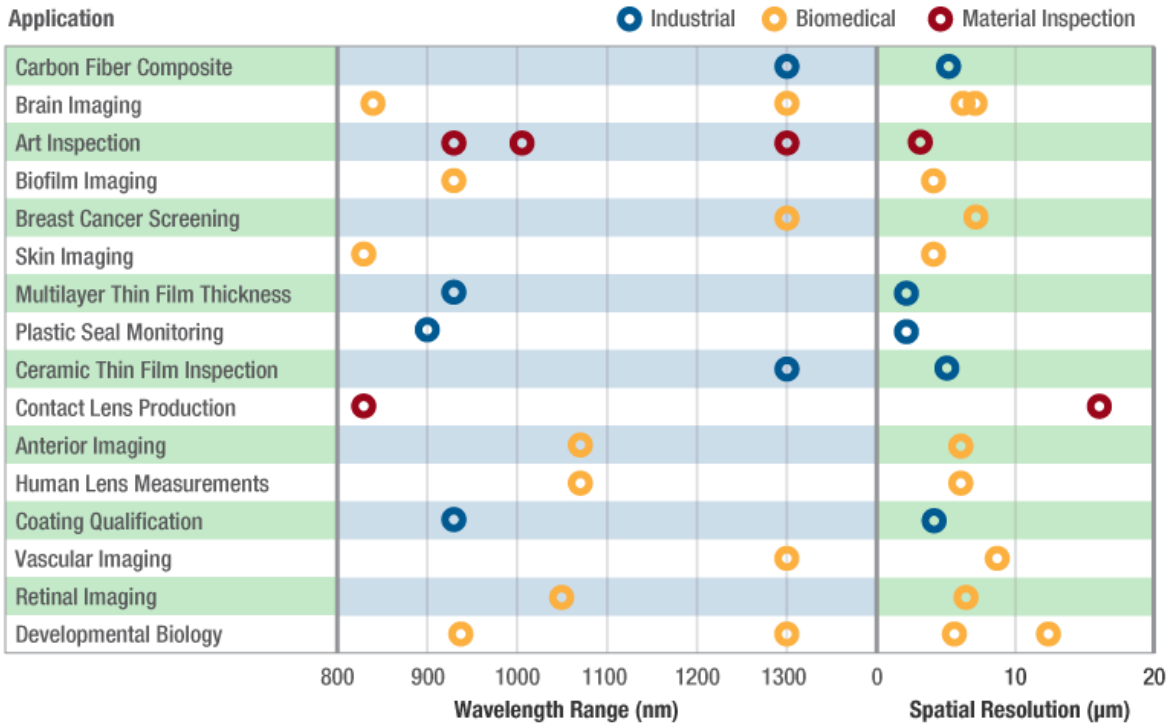

Figure A-1 Compilation of applications for OCT. Organized by application type: blue, industrial; yellow biomedical; and, red, material inspection. Further, the applications are divided again based on compatible wavelength (ranges) (nm) and corresponding spatial resolutions (μm). Adapted from Ref. [95].

Appendix B

Detector Signal Derivations

B-1 Methodology of Generating A-scans

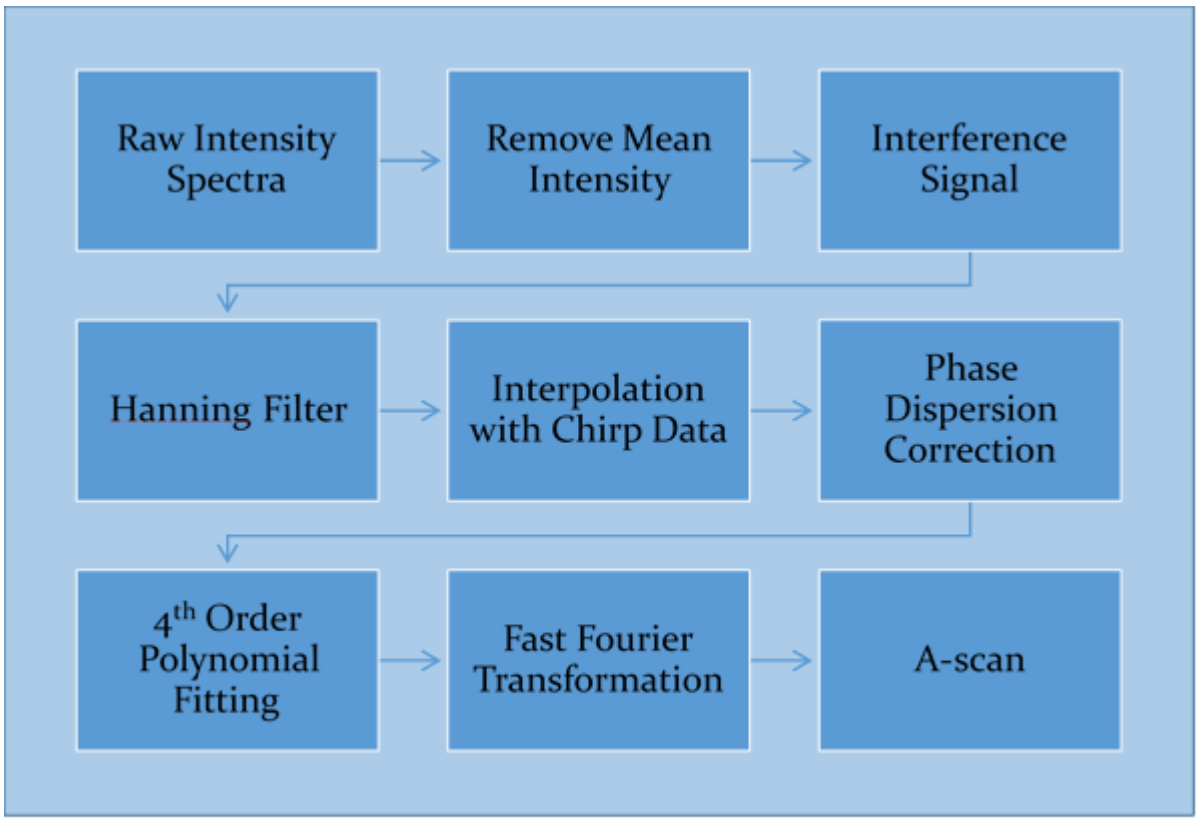

Figure B-1 Flow diagram of data processing pipeline for generation of a single A-scan. The process was carried out in MATLAB® 2018.

B-2 Michelson Interferometer Detector Photocurrent

The observed current at the photodetector measured as the summation of the squares of the electrical fields originating from the reference and sample arms, written as

$$I_0(k,\omega) = current\ at\ detector \sim [E_s(t) + E_r(t)]^2$$

where

$$E(x,y,z,t) = a\cos(\omega t - kz)$$

and

$$\omega = 2\pi\nu \quad k = 2\pi/\lambda$$

Thus, it may be said

$$I_0(k,\omega) \sim |E_r|^2 + |E_s|^2 + 2\cdot E_r \cdot E_s \cos(2\cdot k\cdot \Delta L)$$

in which

$$\Delta L = pathlength$$

By rewriting the photocurrent relationship in terms of complex signals

$$E_i = s(k,\omega)e^{i(kz-\omega t)}$$

with

$$k = \frac{2\pi}{\lambda}$$

$$\omega = 2\pi\nu = angular\ frequency \qquad s = electric\ field\ amplitude$$

and the relationships between frequency, speed, and refractive index

$$\frac{w}{k} = \frac{\lambda\omega}{2\pi} = \frac{c}{n(\lambda)} = \lambda\nu$$

where $n(\lambda)$ represents the material refractive with a wavelength dependence, it can be shown that

$$|E_i|^2 = |E_r|^2 + |E_s|^2 = 0.5\,|E_i|^2 + 0.5\,|E_i|^2$$

given that

$$E_r = \frac{E_i}{\sqrt{2}}[r_r e^{i2kz_r}] \qquad E_s = \frac{E_i}{\sqrt{2}}[r_s(z_s)\ \times e^{i2kz_s}]$$

Where

$$R_i = |r_i|^2$$

is the power reflectivity and the electrical reflectivity, respectively.

Reflectivity must be introduced as different materials reflect and transmit varying fractions of electromagnetic waves. The optical path dependence can be shown of discrete reflectors by the relation

$$\sqrt{R_s(z_s)} = |r_s| = \left|\sum_{n=1}^{N} r_{s_N}\delta(z_s - z_{s_N})\right|$$

where $\delta(z_s - z_{s_N})$ is the depth or optical distance of reflections. Photodetectors measure a time average electrical intensity:

$$I_0(k,\omega) = \frac{\rho}{2}\langle|E_r + E_s|^2\rangle = \frac{\rho}{2}\langle(E_r + E_s)(E_r + E_s)^*\rangle$$

where ρ is photodetector responsivity. The $\frac{1}{2}$ factor is due to the fact that the beams cross the interferometer twice

Expand and simplifying the above equation

$$= \frac{\rho}{2}\langle \left| \frac{s(k,\omega)}{\sqrt{2}} r_r e^{i(2kz_r-\omega t)} + \frac{s(k,\omega)}{\sqrt{2}} r_s e^{i(2kz_s-\omega t)} \right|^2 \rangle$$

$$= \frac{\rho}{2}\left[\begin{array}{l} \left(\frac{s(k,\omega)}{\sqrt{2}} r_r e^{i(2kz_r-\omega t)}\right)\left(\frac{s(k,\omega)}{\sqrt{2}} r_r e^{-i(2kz_r-\omega t)}\right) + \left(\frac{s(k,\omega)}{\sqrt{2}} r_r e^{i(2kz_r-\omega t)}\right)\left(\frac{s(k,\omega)}{\sqrt{2}} r_s e^{-i(2kz_s-\omega t)}\right) + \dots \\ \left(\frac{s(k,\omega)}{\sqrt{2}} r_r e^{-i(2kz_r-\omega t)}\right)\left(\frac{s(k,\omega)}{\sqrt{2}} r_s e^{i(2kz_s-\omega t)}\right) + \left(\frac{s(k,\omega)}{\sqrt{2}} r_s e^{i(2kz_s-\omega t)}\right)\left(\frac{s(k,\omega)}{\sqrt{2}} r_s e^{-i(2kz_s-\omega t)}\right) \end{array} \right]$$

the following expression can be arrived at

$$= \frac{\rho}{2}\left[\left(\frac{s(k,\omega)^2}{2}(r_r)^2\right) + \left(\frac{s(k,\omega)^2}{2}(r_r r_s)e^{i(2k(z_r-z_s))} + \frac{s(k,\omega)^2}{2}(r_r r_s)e^{i(2k(z_s-z_r))}\right) + \left(\frac{s(k,\omega)^2}{2}(r_s^2)\right)\right]$$

Separating term and substituting for power spectral density $S(k) = \langle |s(k,\omega)|^2 \rangle$ and power reflectivity , the referred relations are achieved

$$I_0(k) = \frac{\rho}{4}\left[S(k)\cdot[R_r + R_{s1} + R_{s2} + \dots]\right] \quad "DC\ Terms"$$

$$+ \frac{\rho}{4}\left[S(k)\sum_{n=1}^{N}\sqrt{R_r R_{s_n}}\left[e^{i2k\left(z_r - z_{s_n}\right)} + e^{-i2k\left(z_r - z_{s_n}\right)}\right]\right] \quad "Cross-correlation\ Terms"$$

$$+ \frac{\rho}{4}\left[S(k)\sum_{n\neq m=1}^{N}\sqrt{R_{s_n} R_{s_m}}\left[e^{i2k\left(z_{s_n} - z_{s_m}\right)} + e^{-i2k\left(z_{s_n} - z_{s_m}\right)}\right]\right] "Auto-correlation\ Terms"$$

B-3 Doppler Velocity

The frequency at the detector f_d may be equated

$$f_d = \frac{1}{2\pi}(\mathbf{k}_s - \mathbf{k}_t)\cdot \boldsymbol{V}$$

where

$$|\mathbf{k}| = \frac{2\pi}{\boldsymbol{\lambda}}$$

and

$$\boldsymbol{k} = A\cos(2\pi(kx - \omega t) + \varphi)$$

Expanding the right side of th equation

$$f_d = \frac{1}{2\pi}\left(\overrightarrow{k_s}\cdot\vec{V} - \overrightarrow{k_t}\cdot\vec{V}\right)$$

and substituting

$$f_d = \frac{1}{2\pi}\left(\left|\overrightarrow{k_s}\right|\left|\vec{V}\right|\cos\theta_s - \left|\overrightarrow{k_t}\right|\left|\vec{V}\right|\cos\theta_t\right), \quad \theta_t = (180 - \theta_s)$$

the following equation can be arrived at

$$f_d = \frac{1}{2\pi}\left(\frac{2\pi}{\boldsymbol{\lambda}}V\cos\theta_s - \frac{2\pi}{\boldsymbol{\lambda}}V\cos(180 - \theta_s)\right)$$

$$f_d = \left(\frac{V}{\boldsymbol{\lambda}}\cos\theta_s + \frac{V}{\boldsymbol{\lambda}}\cos\theta_s\right)$$

$$f_d = \frac{2V\cos(\theta_s)}{\boldsymbol{\lambda}_0}$$

where

$$\boldsymbol{\lambda} = wavelength \quad A = amplitude \quad k = spatial\ angular\ frequency$$
$$\boldsymbol{\lambda}_0 = vacuum\ centered\ wavelength$$
$$\theta = Doppler\ angle\ between\ the\ incoming\ light\ and\ the\ particle\ velocity$$
$$x = position \quad \omega = temporal\ angular\ frequency \quad t = time \quad \varphi = phase\ offset$$

Based on scanning rate, f_d can also be equated to

$$f_d = \frac{\Delta\phi}{2\pi T} = \frac{1}{2\pi T}\sum_{m=(n-1)M}^{nM}\sum_{j=1}^{N}\left[\tan^{-1}\left(\frac{Im\left[\widetilde{\Gamma}_{j+1}(t_m)\right]}{Re\left[\widetilde{\Gamma}_{j+1}(t_m)\right]}\right) - \tan^{-1}\left(\frac{Im\left[\widetilde{\Gamma}_{j}(t_m)\right]}{Re\left[\widetilde{\Gamma}_{j}(t_m)\right]}\right)\right]$$
$$= \frac{\Delta\phi}{2\pi T} = \frac{1}{2\pi T}\tan^{-1}\left(\frac{Im\left[\sum_{m=(n-1)M}^{nM}\sum_{j=1}^{N}\widetilde{\Gamma}_{j}(t_m)\cdot\widetilde{\Gamma}^{*}_{j+1}(t_m)\right]}{Re\left[\sum_{m=(n-1)M}^{nM}\sum_{j=1}^{N}\widetilde{\Gamma}_{j}(t_m)\cdot\widetilde{\Gamma}^{*}_{j+1}(t_m)\right]}\right)$$

where

$$\widetilde{\Gamma}_j = complex\ signals\ at\ axial\ times\ t_m\ at\ the\ j'th\ A-scan$$
n = n'th pixel *M = {even number} window size in axial size for each direction A-scan*
N = number of sequential scans for cross-correlation *T = time duration between A-scans*

By equating the two expressions for f_d

$$\frac{2V\cos(\theta_s)}{\boldsymbol{\lambda}_0} = \frac{1}{2\pi}\frac{\Delta\phi}{\Delta t}$$
$$V\cos(\theta_s) = \frac{\boldsymbol{\lambda}_0}{4\pi}\frac{\Delta\phi}{\Delta t}$$

with

$\Delta\phi = phase\ change\ between\ sequential\ A-scans \quad \Delta t = time\ between\ sequential\ A-scans$

Thus, a relation for velocity is derived

Appendix C

Additional Hardware Information & Experimental Protocols

C-1 BI/OND comPLATE™ System

Figure C-1 Rendering of the comPLATE™ system.

C-2 Thorlabs Ganymede OCT Specifications

900 nm OCT Base Units

Base Unit Item #[a]	CAL110	GAN210	GAN610	GAN220	GAN620
Series Name (Click for Link)	Callisto	Ganymede			
Key Performance Feature(s)	Laptop PC for Maximum Portability	High Resolution		Very High Resolution	
		General Purpose	High Speed	General Purpose	High Speed
Center Wavelength	930 nm	930 nm		900 nm	
Imaging Depth[b] (Air/Water)	1.7 mm / 1.3 mm	2.9 mm / 2.2 mm	2.7 mm / 2.0 mm	1.9 mm / 1.4 mm	
Axial Resolution[b] (Air/Water)	7.0 µm / 5.3 µm	6.0 µm / 4.5 µm		3.0 µm / 2.2 µm	
A-Scan Line Rate	1.2 kHz	5.5 kHz to 36 kHz	5 kHz to 248 kHz	5.5 kHz to 36 kHz	5 kHz to 248 kHz
Sensitivity (Max)[c]	107 dB	101 dB	102 dB	101 dB	102 dB
OCT Type	Spectral Domain				

a. These Item #s are OCT base units that can be customized using a wide selection of OCT scanners, lens kits, and optional accessories.
b. Axial resolution and actual imaging depth are dependent on the optical properties of the sample being imaged.
c. Values for the Callisto and Ganymede systems are typical and were measured using a scanner with a common reference/sample path and 50% path split.

C-3 BI/OND OCT Protocol

Goal

Set up Thorlabs Ganymede Series Spectral Domain OCT Imaging System for imaging of the BI/OND® platform.

Background

Optical Coherence Tomography (OCT) is a non-invasive imaging technique that uses low coherence near-infrared lights to obtain structural data of a given sample.

Materials

- 900 nm superluminescent laser diode (SLD)
- Thorlabs OCT Software

- BI/OND inCHIPit™
- Thorlabs (large) Mirror Holder

Procedure

1. Turn on OCT Base Unit equipment and allow SLD to warm up
2. Open ThorLabs application on desktop
   a. Additional software: LabView, MATLAB, "Quick Manual pdf"
3. Set Dataset and Export folders to appropriate personal folder
   a. File > Setting > Dataset Folder --> C:\OCTData\BIOND
   b. File > Setting > Export Folder --> C:\OCTData\BIOND
4. At the top right of the Thorlabs software, you must also name the experiment. Each saved scan will receive an experiment number underneath the experiment name umbrella
5. In 2D mode, with no object in the field of view (FOV), set the intensity to approximately 70%. Range is [60%, 80%] by adjusting the aperture
   a. Numerical Aperture NA (i.e. F-stop number) is a determining factor in image resolution. Larger NA (i.e. low F-stop numbers) values give shallower FOVs while lower NA values (i.e. high F-stop numbers) give larger deeper FOVs
6. Switching to 1D mode, still with no object in the FOV, adjust raw spectral data to approximately 80% maximum signal by adjusting the reference bean
7. Making use of live view of chip holder, align microfluidic channels to sample holder adjustment directions (i.e. x-axis knob and y-axis knob)
   a. Using a pen or other external object to orient visual field and device such that channel is parallel along the y-axis and perpendicular along the x-axis
8. Switching back to 2D mode, make a B-scan along each of the major axes. All types of scans (A, B, and M) may be adjust in the bottom left of the Thorlabs software by selecting a point or area I the live view. Adjust each axis individually until the chip is level as possible by eye
9. By performing a 2D scan with an A-scan slice visualized (select a vertical place along a point of high signal intensity), set the focal point by setting z-depth to points of largest signal strength (in dB). Typically, this is around ~ 1mm depth in 2D mode

C-4 BI/OND MFCS™-EX Protocol

Goal

Set up Fluigent Microfluidic Flow Control System EX (MFCS™-EX) to BI/OND® platform for pneumatic control and fluid flows.

Background

The controller connects to Fluigent All-in-One (A-i-O) - "Easy Mode" - and Fluigent Microfluidic Automation Tool software that allow for the induction and definition of pumping protocols to dictate membrane pressure profiles and fluid flow profiles. The Fluigent A-i-O software samples at 20ms while Fluigent Microfluidic Automation Tool samples at 50ms.

Materials

- Fluigent MFCS™-EX
- Power cable
- USB connector cable
- BI/OND® Microfluidic Platform (Version 1.0)
- Fluigent Software (Fluigent A-i-O 2018 or Fluigent Microfluidic Automation Tool 2018)

Procedure

A-i-O 2018 "Easy Mode"

1. Connect power cable and USB connector
2. Turn on the Fluigent MFCS™-EX and open the software of choice
3. Wait for software and hardware to initialize

   a. Allow P_{gauge} vs time plots a full decade of observation at 0 millibar before proceeding with measurements
4. Connect elastic tubing to each pressure valve in use (i.e. typically fluid channel and pneumatic channel)
   a. Safer to connect tubing to Fluigent MFCS™-EX while all valves are at 0 millibar and/or the Fluigent MFCS™-EX is paused
5. Input the desired pressure drops to each corresponding pressure valve in the AIO software, numbered 1 to 8
6. Press "Play" button on the Fluigent MFCS™-EX **without** connecting to the BI/OND® platform to confirm hardware and software are functioning properly
7. Pause Fluigent MFCS™-EX and connect tubing to BI/OND® platform

Appendix D

Experimental Addendum

D-1 Demonstration of Single Axis Adjustments

Table D.1 Demonstration of setting both x-axis and y-axis perpendicular to impinging light beam. Measured on an inverted inCHIPit-3C™.

Exp. #	Orientation	Video Image	B-scan Reconstruction	Zoomed View	Angle of Inclination
001	Parallel to Channel	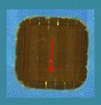		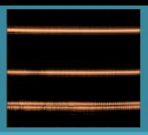	≈ 0°
002	Perpendicular to Channel	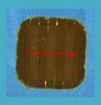		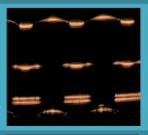	≈ 0°
003	Positive Diagonal	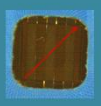		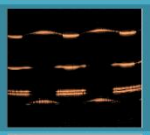	≈ 0°
004	Negative Diagonal		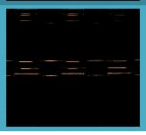	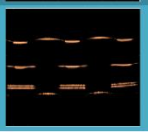	≈ 0°

Table D.2 Demonstration of setting only the y-axis at angle to impinging light beam. Measured on an inverted inCHIPit-3C™.

Exp. #	Orientation	Video Image	OCT Reconstruction	OCT Reconstruction Zoom	Angle of Inclination	Signal Level
010	Parallel to Channel Membrane	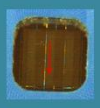		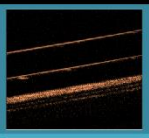	≈ 5.0° [5.101°, 4.969°]	≈ 30 dB
011	Perpendicular to Channel	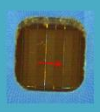			≈ 5.0° [5.101°, 4.969°]	≈ 30 dB
012	Perpendicular to Channel	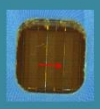			< 5.0°	≈ 40 dB
013	Perpendicular to Channel		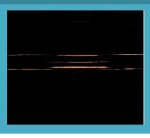	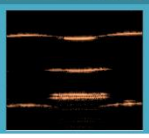	≈ 0°	≈ 50 dB* *Autocorrelation noise returns

Table D.3 Demonstration of setting only the x-axis at angle to impinging light beam. Measured on an inverted inCHIPit-3C™.

Exp. #	Orientation	Video Image	OCT Reconstruction	OCT Reconstruction Zoom	Angle of Inclination
016	Parallel to Channel Membrane	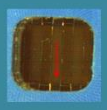	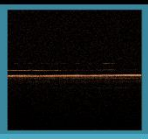	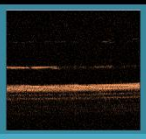	≈ 0°
015	Parallel to Channel PDMS Wall	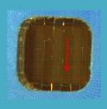		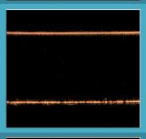	≈ 0°
017	Perpendicular to Channel	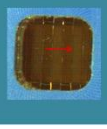			≈ 4.95° [4.891°, 4.987°]

D-2 Emulsion Front Velocity Images

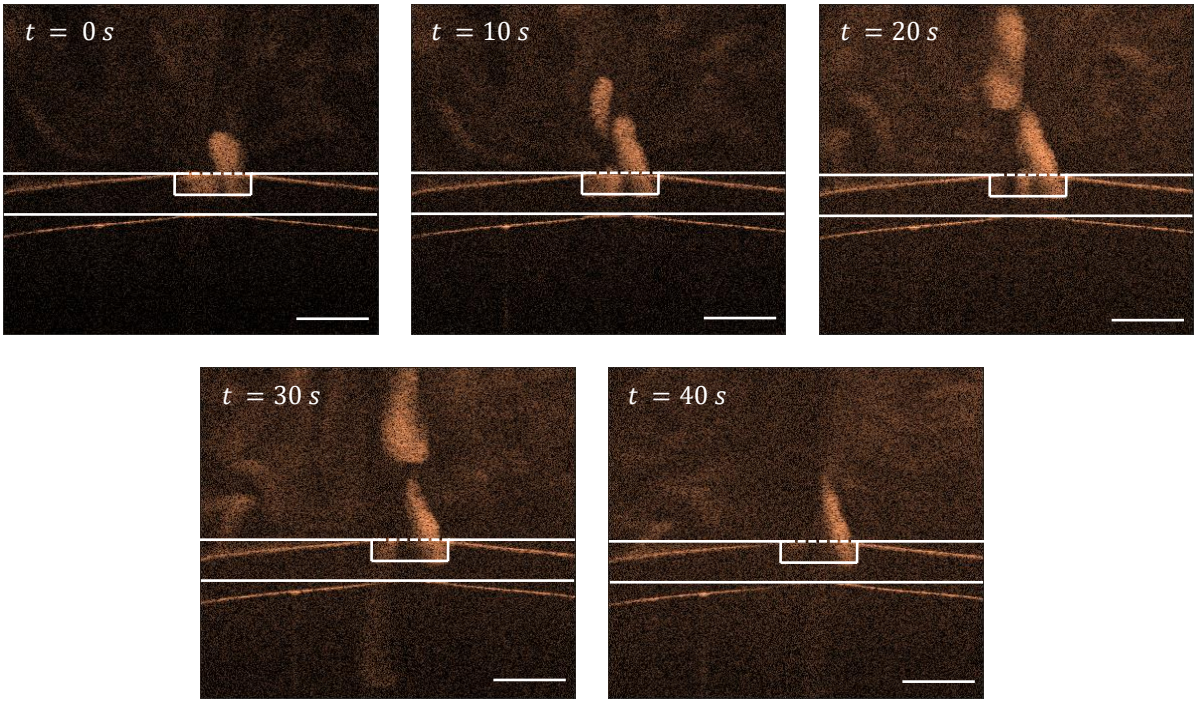

Figure D-1 Sequential transverse B-scans acquired during diffusion studies. Time interval images were captured every ten seconds. The flow rate was set to approximately 33 μL min^{-1}. Measurements were performed in an upright inCHIPit-1C^{TM}. The solid and dotted white lines demarcated the solid PDMS and porous membrane, respectively. The scale bar is 300 μm.

D-3 Data Curve Fitting

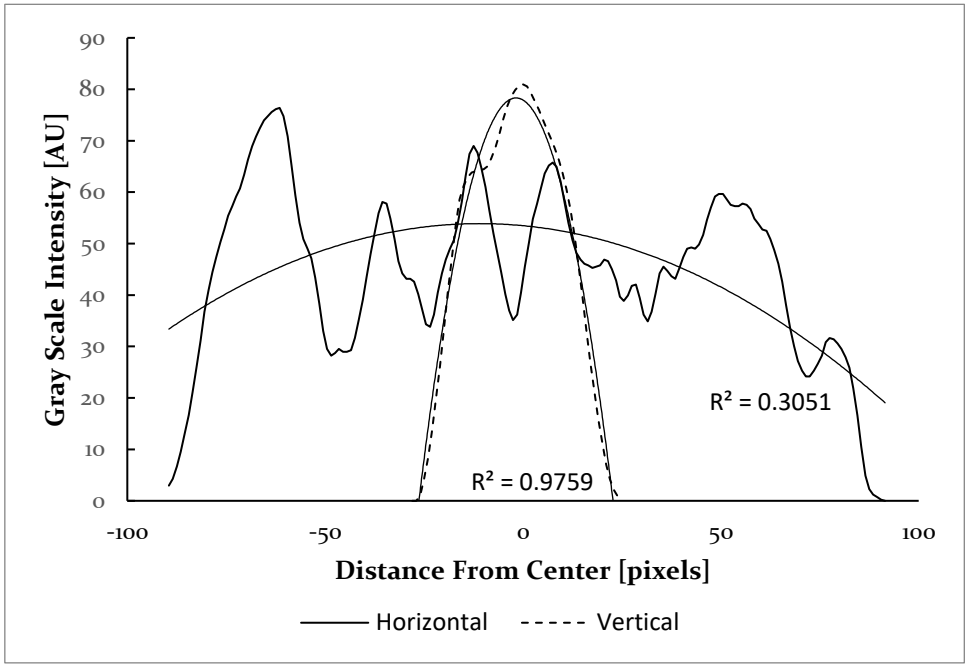

Figure D-2 Axially resolved gray scale intensity profiles (AU = arbitrary units) taken in the horizontal (solid line) and vertical (dotted line) directions of the inset image with second order polynomial fitting.

Glossary

List of Acronyms

1D	One-dimensional
2D	Two-dimensional
3D	Three-dimensional
Al	Aluminum
ANG-1	Angiopoietin 1
BHF	Buffered Hydrofluoric Acid
bioMEMS	Biomedical MEMS
CCD	Charge Coupled Detector
DC	Direct Current
D-OCT	Doppler Optical Coherence Tomography
DI H_2O	Deionized Water
DRIE	Deep Reactive Ion Etching
ECM	Extracellular Matrix
EEMCS	Electrical Engineering, Mathematics, & Computer Science
FD	Fourier Domain
FFT	Fast Fourier Transform
FOV	Field of View
FRP	Flow Rate Platform
GF	Growth Factor
Hh	Hedgehog Protein
inCHIPit-1C™	inCHIPit™ 1-lane
inCHIPit-3C™	inCHIPit™ 3-lane
LOC	Lab on Chip
MEMS	Microelectromechanical Systems
MFCS™	Microfluidic Flow Control System
µPIV	Micro-particle Image Velocimetry
µTAS	Micro Total Chemical Analysis Systems
NDE	Non-destructive Evaluation
NDT	Non-destructive Testing
OCT	Optical Coherence Tomography
OLB	Organoid-like Body
OOC	Organ on chip
PDMS	Poly(dimethyl)siloxane
PECVD	Plasma Enhanced Chemical Vapor Deposition
POS	PDMS on Silicon
R&D	Research and Development
SD	Spectral Domain
Si	Silicon
SiO_2	Silicon Oxide
SLD	Superluminsecent Diode
TD	Time Domain
TU Delft	Technical University of Delft
UV	Ultraviolet
VEGF	Vascular Endothelial Growth Factor

Bibliography

[1] A. Manz, N. Graber, and H. M. Widmer, "Miniaturized total chemical analysis systems: A novel concept for chemical sensing," *Sensors Actuators B. Chem.*, 1990, doi: 10.1016/0925-4005(90)80209-I.

[2] N. Khalid, I. Kobayashi, and M. Nakajima, "Recent lab-on-chip developments for novel drug discovery," *Wiley Interdiscip. Rev. Syst. Biol. Med.*, vol. 9, no. 4, p. e1381, Jul. 2017, doi: 10.1002/wsbm.1381.

[3] H. Z. An, E. R. Safai, H. Burak Eral, and P. S. Doyle, "Synthesis of biomimetic oxygen-carrying compartmentalized microparticles using flow lithography," *Lab Chip*, vol. 13, no. 24, p. 4765, 2013, doi: 10.1039/c3lc50610j.

[4] F. Fachin *et al.*, "Monolithic Chip for High-throughput Blood Cell Depletion to Sort Rare Circulating Tumor Cells," *Sci. Rep.*, vol. 7, no. 1, Dec. 2017, doi: 10.1038/s41598-017-11119-x.

[5] K. A. Wetterstrand, "DNA Sequencing Costs: Data," *National Human Genome Research Institute*, 2019. https://www.genome.gov/about-genomics/fact-sheets/DNA-Sequencing-Costs-Data (accessed Dec. 10, 2019).

[6] E. R. Mardis, "A decade's perspective on DNA sequencing technology," *Nature*, vol. 470, no. 7333, pp. 198–203, 2011, doi: 10.1038/nature09796.

[7] M. L. Metzker, "Sequencing technologies the next generation," *Nat. Rev. Genet.*, vol. 11, no. 1, pp. 31–46, 2010, doi: 10.1038/nrg2626.

[8] S. Lightfoot, "Quantitation comparison of total RNA using the Agilent 2100 bioanalyzer , ribo-green analysis and UV spectrometry Application," pp. 1–8, 2002, doi: 5988-7650EN.

[9] F. Gorjikhah *et al.*, "Improving 'lab-on-a-chip' techniques using biomedical nanotechnology: a review," *Artif. Cells, Nanomedicine, Biotechnol.*, vol. 44, no. 7, pp. 1609–1614, Oct. 2016, doi: 10.3109/21691401.2015.1129619.

[10] B. Roussel, S. Clerc, and M. Villien, "Organs-on-chips 2017 Report: From Technologies to Market Sample," 2017.

[11] P. Kim *et al.*, "Soft Litography for Microfluidics: a Review," *Biochip*, p. 11, 2008, doi: 10.1107/S0108270110005755.

[12] J. C. McDonald *et al.*, "Fabrication of microfluidic systems in poly(dimethylsiloxane)," *Electrophoresis*, vol. 21, no. 1, pp. 27–40, Jan. 2000, doi: 10.1002/(SICI)1522-2683(20000101)21:1<27::AID-ELPS27>3.0.CO;2-C.

[13] C. Kyu Byun, K. Abi-Samra, Y.-K. Cho, and S. Takayama, "Pumps for microfluidic cell culture," *Electrophoresis*, vol. 35, pp. 245–257, 2014, doi: 10.1002/elps.201300205.

[14] W. F. Quirós-Solano *et al.*, "Microfabricated tuneable and transferable porous PDMS membranes for Organs-on-Chips," *Sci. Rep.*, vol. 8, no. 1, Dec. 2018, doi: 10.1038/s41598-018-31912-6.

[15] R. Greek and M. J. Rice, "Animal models and conserved processes," *Theor. Biol. Med. Model.*, vol. 9, no. 1, p. 40, Dec. 2012, doi: 10.1186/1742-4682-9-40.

[16] L. L. Bischel, K. E. Sung, J. A. Jiménez-Torres, B. Mader, P. J. Keely, and D. J. Beebe, "The importance of being a lumen," *FASEB J.*, vol. 28, no. 11, pp. 4583–4590, 2014, doi: 10.1096/fj.13-243733.

[17] I. Meyvantsson and D. J. Beebe, "Cell Culture Models in Microfluidic Systems," *Annu. Rev. Anal. Chem.*, vol. 1, no. 1, pp. 423–449, 2008, doi: 10.1146/annurev.anchem.1.031207.113042.

[18] D. Huh, Y. S. Torisawa, G. A. Hamilton, H. J. Kim, and D. E. Ingber, "Microengineered physiological biomimicry: Organs-on-Chips," *Lab Chip*, vol. 12, no. 12, pp. 2156–2164, 2012, doi: 10.1039/c2lc40089h.

[19] D. E. Ingber, "Developmentally inspired human 'organs on chips,'" *Dev.*, vol. 145, no. 16 Special Issue, pp. 10–13, 2018, doi: 10.1242/dev.156125.

[20] V. van Duinen, S. J. Trietsch, J. Joore, P. Vulto, and T. Hankemeier, "Microfluidic 3D cell culture: from tools to tissue models," *Curr. Opin. Biotechnol.*, vol. 35, pp. 118–126, Dec. 2015, doi: 10.1016/J.COPBIO.2015.05.002.

[21] D. E. Ingber, "From mechanobiology to developmentally inspired engineering," *Philosophical Transactions of the Royal Society B: Biological Sciences*, vol. 373, no. 1759. Royal Society

Publishing, 2018, doi: 10.1098/rstb.2017.0323.
[22] D. Huh, B. D. Matthews, A. Mammoto, M. Montoya-Zavala, H. Yuan Hsin, and D. E. Ingber, "Reconstituting organ-level lung functions on a chip," *Science (80-.).*, vol. 328, no. 5986, pp. 1662–1668, 2010, doi: 10.1126/science.1188302.
[23] H. J. Kim and D. E. Ingber, "Gut-on-a-Chip microenvironment induces human intestinal cells to undergo villus differentiation," *Integr. Biol. (United Kingdom)*, vol. 5, no. 9, pp. 1130–1140, 2013, doi: 10.1039/c3ib40126j.
[24] S. N. Bhatia and D. E. Ingber, "Microfluidic organs-on-chips," *Nature Biotechnology*, vol. 32, no. 8. pp. 760–772, 2014, doi: 10.1038/nbt.2989.
[25] Y. Shin *et al.*, "In vitro 3D collective sprouting angiogenesis under orchestrated ANG-1 and VEGF gradients," *Lab Chip*, vol. 11, no. 13, pp. 2175–2181, 2011, doi: 10.1039/c1lc20039a.
[26] V. van Duinen, D. Zhu, C. Ramakers, A. J. van Zonneveld, P. Vulto, and T. Hankemeier, "Perfused 3D angiogenic sprouting in a high-throughput in vitro platform," *Angiogenesis*, pp. 1–9, Aug. 2018, doi: 10.1007/s10456-018-9647-0.
[27] I. Wagner *et al.*, "A dynamic multi-organ-chip for long-term cultivation and substance testing proven by 3D human liver and skin tissue co-culture," *Lab Chip*, vol. 13, no. 18, pp. 3538–3547, 2013, doi: 10.1039/c3lc50234a.
[28] Z. Xu *et al.*, "Application of a microfluidic chip-based 3D co-culture to test drug sensitivity for individualized treatment of lung cancer," *Biomaterials*, vol. 34, no. 16, pp. 4109–4117, 2013, doi: 10.1016/j.biomaterials.2013.02.045.
[29] P. Gravesen, J. Branebjerg, and O. S. Jensen, "Microfluidics - A review," *Journal of Micromechanics and Microengineering*, vol. 3, no. 4. pp. 168–182, 1993, doi: 10.1088/0960-1317/3/4/002.
[30] V. Vogel, "Unraveling the Mechanobiology of Extracellular Matrix," *Annual Review of Physiology*, vol. 80, no. 1. pp. 353–387, 2018, doi: 10.1146/annurev-physiol-021317-121312.
[31] S. Kim, M. Chung, J. Ahn, S. Lee, and N. L. Jeon, "Interstitial flow regulates the angiogenic response and phenotype of endothelial cells in a 3D culture model," *Lab Chip*, vol. 16, no. 21, pp. 4189–4199, 2016, doi: 10.1039/c6lc00910g.
[32] N. Gaio *et al.*, "Cytostretch, an Organ-on-Chip Platform," *Micromachines*, vol. 7, no. 7, p. 120, Jul. 2016, doi: 10.3390/mi7070120.
[33] N. J. Douville *et al.*, "Combination of fluid and solid mechanical stresses contribute to cell death and detachment in a microfluidic alveolar model," *Lab Chip*, vol. 11, no. 4, pp. 609–619, 2011, doi: 10.1039/colc00251h.
[34] Y. Liu, E. Gill, and Y. Y. Shery Huang, "Microfluidic on-chip biomimicry for 3D cell culture: a fit-for-purpose investigation from the end user standpoint," *Futur. Sci. OA*, vol. 3, no. 2, p. FSO173, 2017, doi: 10.4155/fs0a-2016-0084.
[35] S. Murphy, S. Murphy, M. Devarasetty, D. Yildiz, A. Atala, and D. Konar, "Lung-On-A-Chip Technologies for Disease Modeling and Drug Development," *Biomed. Eng. Comput. Biol.*, vol. 2016, no. S1, p. 17, 2016, doi: 10.4137/BECB.S34252.
[36] A. Skardal, T. Shupe, and A. Atala, "Organoid-on-a-chip and body-on-a-chip systems for drug screening and disease modeling," *Drug Discov. Today*, vol. 21, no. 9, pp. 1399–1411, 2016, doi: 10.1016/j.drudis.2016.07.003.
[37] K. H. Benam *et al.*, "Engineered In Vitro Disease Models," *Annu. Rev. Pathol. Mech. Dis.*, vol. 10, no. 1, pp. 195–262, 2015, doi: 10.1146/annurev-pathol-012414-040418.
[38] M. L. Shuler, "Advances in organ-, body-, and disease-on-a-chip systems," *Lab on a Chip*, vol. 19, no. 1. Royal Society of Chemistry, pp. 9–10, 2019, doi: 10.1039/c8lc90089b.
[39] B. Zhang and M. Radisic, "Organ-on-A-chip devices advance to market," *Lab Chip*, vol. 17, no. 14, pp. 2395–2420, 2017, doi: 10.1039/c6lc01554a.
[40] IEEE Thailand Section. and Institute of Electrical and Electronics Engineers., … "Biomedical Engineering International Conference.," pp. 2–8, 2019.
[41] M. Mastrangeli, S. Millet, T. Orchid Partners, and J. Van den Eijnden-van Raaij, "Organ-on-chip in development: Towards a roadmap for organs-on-chip," *ALTEX*, vol. 36, no. 4, pp. 650–668, 2019, doi: 10.14573/altex.1908271.
[42] N. Franzen, W. H. van Harten, V. P. Retèl, P. Loskill, J. van den Eijnden-van Raaij, and M. IJzerman, "Impact of organ-on-a-chip technology on pharmaceutical R&D costs," *Drug Discov. Today*, vol. 24, no. 9, pp. 1720–1724, 2019, doi: 10.1016/j.drudis.2019.06.003.
[43] N. Gaio, "Organ-on-Silicon," 2019.

[44] N. Gaio, C. Silvestri, B. Van Meer, S. Vollebregt, C. Mummery, and R. Dekker, "Fabrication and characterization of an Upside-down Carbon Nanotube (CNT) Microelectrode array (MEA)," *IEEE Sens. J.*, vol. 16, p. 1, 2016, doi: 10.1109/JSEN.2016.2573854.

[45] W. F. Quiros-Solano, N. Gaio, C. Silvestri, G. Pandraud, and P. M. Sarro, "Polymeric strain gauges as pressure sensors for microfabricated organ-on-chips," *TRANSDUCERS 2017 - 19th Int. Conf. Solid-State Sensors, Actuators Microsystems*, pp. 1296–1299, 2017, doi: 10.1109/TRANSDUCERS.2017.7994293.

[46] J. Friend and L. Yeo, "Fabrication of microfluidic devices using polydimethylsiloxane," *Biomicrofluidics*, vol. 4, no. 2, 2010, doi: 10.1063/1.3259624.

[47] R. Edmondson, J. J. Broglie, A. F. Adcock, and L. Yang, "Three-dimensional cell culture systems and their applications in drug discovery and cell-based biosensors," *Assay Drug Dev. Technol.*, vol. 12, no. 4, pp. 207–218, 2014, doi: 10.1089/adt.2014.573.

[48] U. Jandt, O. Platas Barradas, R. Pörtner, and A. P. Zeng, "Mammalian cell culture synchronization under physiological conditions and population dynamic simulation," *Appl. Microbiol. Biotechnol.*, vol. 98, no. 10, pp. 4311–4319, 2014, doi: 10.1007/s00253-014-5553-6.

[49] E. A. V. Jones, M. H. Baron, S. E. Fraser, and M. E. Dickinson, "Measuring hemodynamic changes during mammalian development," *Am. J. Physiol. Circ. Physiol.*, vol. 287, no. 4, pp. H1561–H1569, Oct. 2004, doi: 10.1152/ajpheart.00081.2004.

[50] S. Ghaffari, R. L. Leask, and E. A. V. Jones, "Flow dynamics control the location of sprouting and direct elongation during developmental angiogenesis," *Development*, vol. 142, no. 23, pp. 4151–4157, 2015, doi: 10.1242/dev.128058.

[51] J. B. Pawley, Ed., *Handbook Of Biological Confocal Microscopy*. Boston, MA: Springer US, 2006.

[52] M. Ali, "Signal Processing Overview of Optical Coherence Tomography Systems for Medical Imaging," 2010. [Online]. Available: www.ti.com.

[53] B. J. Vakoc, S. H. Yun, J. F. De Boer, G. J. Tearney, and B. E. Bouma, "Phase-resolved optical frequency domain imaging."

[54] G. Liu and Z. Chen, "Advances in Doppler OCT," *Chinese Opt. Lett.*, vol. 11, no. 1, Jan. 2013, doi: 10.3788/COL201311.011702.

[55] I. Newton and G. . Hemming, *Opticks: or, A treatise of the reflections, refractions, inflexions and colours of light : also two treatises of the species and magnitude of curvilinear figures*. London: Printed for Sam. Smith, and Benj. Walford, 1704.

[56] P. Hariharan, *Basics of Interferometry*, 2nd ed. Academic Press, 2007.

[57] P. Hariharan, *Optical Interferometry*, 2nd ed. Academic Press, 2003.

[58] H. F. Stewart, M. E. Stratmeyer, and Center for Devices and Radiological Health (U.S.), *An Overview of ultrasound : theory, measurement, medical applications, and biological effects*. 1982.

[59] B. Bunch and A. Hellemans, *The History of Science and Technology A Browser's Guide to the Great Discoveries, Inventions, and the People Who MadeThem from the Dawn of Time to Today*, Illustrate. Houghton Mifflin Harcourt - HMH, 2004.

[60] D. M. Greenberger, M. A. Horne, and A. Zeilinger, "Multiparticle Interferometry and the Superposition Principle," *Phys. Today*, vol. 46, no. 8, pp. 22–29, 1993, doi: 10.1063/1.881360.

[61] J. R. Friedman, V. Patel, W. Chen, S. K. Tolpygo, and J. E. Lukens, "Quantum superposition of distinct macroscopic states," *Nature*, vol. 406, no. 6791, pp. 43–46, 2000, doi: 10.1038/35017505.

[62] X. Gu, A. F. Kockum, A. Miranowicz, Y. xi Liu, and F. Nori, "Microwave photonics with superconducting quantum circuits," *Phys. Rep.*, vol. 718–719, pp. 1–102, 2017, doi: 10.1016/j.physrep.2017.10.002.

[63] Wikimedia Commons contributors, "Rayleigh interferometer.PNG." Wikipedia Commons, the free media respository, 2015, [Online]. Available: https://commons.wikimedia.org/w/index.php?title=File:Rayleigh_interferometer.PNG&oldid=154984650.

[64] J. M. Schmitt, "Optical coherence tomography (OCT): a review," *IEEE J. Sel. Top. Quantum Electron.*, vol. 5, no. 4, pp. 1205–1215, 1999, doi: 10.1109/2944.796348.

[65] J. G. Fujimoto and W. Drexler, "Introduction to OCT," *Opt. Coherence Tomogr. Technol. Appl. Second Ed.*, pp. 3–64, 2015, doi: 10.1007/978-3-319-06419-2_1.

[66] E. A. Swanson *et al.*, "In vivo retinal imaging by optical coherence tomography," *Opt. Lett.*, vol. 18, no. 21, p. 1864, 1993, doi: 10.1364/ol.18.001864.

[67] S. A. Boppart, M. E. Brezinski, B. E. Bouma, G. J. Tearney, and J. G. Fujimoto, "Investigation of developing embryonic morphology using optical coherence tomography," *Dev. Biol.*, vol. 177, no.

1, pp. 54–63, 1996, doi: 10.1006/dbio.1996.0144.
[68] D. Stifter, "Beyond biomedicine: A review of alternative applications and developments for optical coherence tomography," *Appl. Phys. B Lasers Opt.*, vol. 88, no. 3, pp. 337–357, Aug. 2007, doi: 10.1007/s00340-007-2743-2.
[69] S. E. Fujimoto JG, Brezinski ME, Tearney GJ, Boppart SA, Bouma B, Hee MR, Southern JF, "Optical biopsy and imaging using optical coherence tomography," doi: 10.1038/nm0995-970.
[70] Thorlabs, "Optical coherence tomography," 2020. https://www.thorlabs.com/newgrouppage9.cfm?objectgroup_id=5702.
[71] M. E. Brezinski, "NOISE AND SYSTEM PERFORMANCE WITH TD-OCT AND SD-OCT," in *Optical Coherence Tomography*, Elsevier, 2006, pp. 175–195.
[72] NobelPrize.org, "Albert A. Michelson – Biographical," *Nobel Media AB 2020*. https://www.nobelprize.org/prizes/physics/1907/michelson/biographical/ (accessed May 08, 2020).
[73] J. A. Izatt, M. A. Choma, and A.-H. Dhalla, "Theory of Optical Coherence Tomography," in *Optical Coherence Tomography*, Cham: Springer International Publishing, 2015, pp. 65–94.
[74] W. Drexler and J. G. Fujimoto, Eds., *Optical Coherence Tomography*. Cham: Springer International Publishing, 2015.
[75] J. Rosen and L. Q. Gothard, *Encyclopedia of Physical Science*. Facts On File, 2010.
[76] Z. Chen and J. Zhang, "Doppler Optical Coherence Tomography," in *Optical Coherence Tomography*, Cham: Springer International Publishing, 2015, pp. 1289–1320.
[77] R. Lyons and B. Associates, "Frequency domain tutorial, part 2: complex signals and spectral diagrams," *EE Times DESIGNLINES MILITARY & AEROSPACE DESIGNLINE*, 2008. https://www.eetimes.com/frequency-domain-tutorial-part-2-complex-signals-and-spectral-diagrams/ (accessed May 31, 2020).
[78] F. Mayinger, Ed., *Optical Measurements*. Berlin, Heidelberg: Springer Berlin Heidelberg, 1994.
[79] J. P. Dunkers *et al.*, "Optical coherence tomography of glass reinforced polymer composites," *Compos. Part A Appl. Sci. Manuf.*, vol. 30, no. 2, pp. 139–145, Feb. 1999, doi: 10.1016/S1359-835X(98)00084-0.
[80] P. E. Ciddor, "Refractive index of air: new equations for the visible and near infrared," *Appl. Opt.*, vol. 35, no. 9, p. 1566, Mar. 1996, doi: 10.1364/AO.35.001566.
[81] G. M. Hale and M. R. Querry, "Optical Constants of Water in the 200-nm to 200-μm Wavelength Region," *Appl. Opt.*, vol. 12, no. 3, p. 555, Mar. 1973, doi: 10.1364/AO.12.000555.
[82] F. Schneider, J. Draheim, R. Kamberger, and U. Wallrabe, "Process and material properties of polydimethylsiloxane (PDMS) for Optical MEMS," *Sensors Actuators, A Phys.*, vol. 151, no. 2, pp. 95–99, 2009, doi: 10.1016/j.sna.2009.01.026.
[83] S. Deguchi, J. Hotta, S. Yokoyama, and T. S. Matsui, "Viscoelastic and optical properties of four different PDMS polymers," *J. Micromechanics Microengineering*, vol. 25, no. 9, 2015, doi: 10.1088/0960-1317/25/9/097002.
[84] J. A. Izatt, M. A. Choma, and A.-H. Dhalla, "Theory of Optical Coherence Tomography," in *Optical Coherence Tomography*, 2nd ed., W. Drexler and J. G. Fujimoto, Eds. Springer International Publishing Switzerland, 2015, pp. 65–94.
[85] K. Haase and R. D. Kamm, "Advances in on-chip vascularization," *Regen. Med.*, vol. 12, no. 3, pp. 285–302, 2017, doi: 10.2217/rme-2016-0152.
[86] S. J. Trietsch, G. D. Israëls, J. Joore, T. Hankemeier, and P. Vulto, "Microfluidic titer plate for stratified 3D cell culture," *Lab Chip*, vol. 13, no. 18, pp. 3548–3554, 2013, doi: 10.1039/c3lc50210d.
[87] S. Torino, B. Corrado, M. Iodice, and G. Coppola, "PDMS-Based Microfluidic Devices for Cell Culture," *Inventions*, vol. 3, no. 3, p. 65, Sep. 2018, doi: 10.3390/inventions3030065.
[88] S. Moon, S.-W. Lee, and Z. Chen, "Reference spectrum extraction and fixed-pattern noise removal in optical coherence tomography," *Opt. Express*, vol. 18, no. 24, p. 24395, Nov. 2010, doi: 10.1364/OE.18.024395.
[89] Thorlabs, "ThorImage OCT Operating Manual." Thorlabs, Dachau/Munich, 2014.
[90] O. Tan, Y. Jia, E. Wei, and D. Huang, "Clinical Applications of Doppler OCT and OCT Angiography," in *Optical Coherence Tomography*, Cham: Springer International Publishing, 2015, pp. 1413–1428.
[91] M. M. Denn, *Process Fluid Mechanics*. Prentice-Hall, 1980.
[92] O. Bottema and B. Roth, *Theoretical Kinematics*, Revised Ed. Dover Publications, 2012.
[93] Z. Zhao, L. Jing, and I. Neretnieks, "Evaluation of hydrodynamic dispersion parameters in

fractured rocks," *J. Rock Mech. Geotech. Eng.*, vol. 2, pp. 243–254, 2010, doi: 10.3724/SP.J.1235.2010.00243.
[94] S. Mantha *et al.*, "Smart Hydrogels in Tissue Engineering and Regenerative Medicine," *Materials (Basel).*, vol. 12, no. 20, p. 3323, Oct. 2019, doi: 10.3390/ma12203323.
[95] "Microscopy and Laser Imaging." [Online]. Available: www.thorlabs.com.